5

Monte-Carlo Simulations of Globular Cluster Dynamics

by

Kriten J. Joshi

Submitted to the Department of Physics
in partial fulfillment of the requirements for the degree of

Doctor of Philosophy

at the

MASSACHUSETTS INSTITUTE OF TECHNOLOGY

February 2000

Author .....
Department of Physics
January 28, 2000

Certified by .....
Frederic A. Rasio
Assistant Professor
Thesis Supervisor

Accepted by .....
Thomas J. Greytak
Professor, Associate Department Head for Education

Monte-Carlo Simulations of Globular Cluster Dynamics

by

Kriten J. Joshi

Submitted to the Department of Physics
on January 28, 2000, in partial fulfillment of the
requirements for the degree of
Doctor of Philosophy

Abstract

We present the results of theoretical calculations for the dynamical evolution of dense globular star clusters. Our new study was motivated in part by the wealth of new data made available from the latest optical, radio, and X-ray observations of globular clusters by various satellites and ground-based observatories, and in part by recent advances in computer hardware. New parallel supercomputers, combined with improved computational methods, now allow us to perform dynamical simulations of globular cluster evolution using a realistic number of stars ($N \sim 10^5 - 10^6$) and taking into account the full range of relevant stellar dynamical and stellar evolutionary processes. These processes include two-body gravitational scattering, strong interactions and physical collisions involving both single and binary stars, stellar evolution of single stars, and stellar evolution and interactions in close binary stars.

We have developed a new numerical code for computing the dynamical evolution of a dense star cluster. Our code is based on a Monte Carlo technique for integrating numerically the Fokker-Planck equation. We have used this new code to study a number of important problems. In particular, we have studied the evolution of globular clusters in our Galaxy, including the effects of a mass spectrum, mass loss due to the tidal field of the Galaxy, and stellar evolution. Our results show that the direct mass loss from stellar evolution can significantly accelerate the total mass loss from a globular cluster, causing most clusters with low initial central concentrations to disrupt completely. Only clusters born with high central concentrations, or with relatively few massive stars, are likely to survive until the present and remain observable. Our study of mass segregation in clusters shows that it is possible to retain significant numbers of very-low-mass ($m \ll 0.1\mathrm{M}_\odot$) objects, such as brown dwarfs or planets, in the outer halos of globular clusters, even though they are quickly lost from the central, denser regions. This is contrary to the common belief that globular clusters are devoid of such low-mass objects. We have also performed, for the first time, dynamical simulations of clusters containing a realistic number of stars and a significant fraction of binaries. We find that the energy generated through binary-binary and binary-single-star interactions in the cluster core can support the system against gravothermal collapse on timescales exceeding the age of the Universe, ex-

plaining naturally the properties of the majority of observed globular clusters with resolved cores.

Thesis Supervisor: Frederic A. Rasio
Title: Assistant Professor

Acknowledgments

I would like to thank my family for their unflinching support, and for encouraging me to study the science that I have always loved. I would like to thank my advisor Prof. Rasio for being a great mentor and teacher, and for introducing me to the joys of research. I would also like to thank my thesis committee members Prof. Kaspi and Prof. Bertschinger for many helpful comments and discussions, and also for their patience and understanding.

Contents

List of Figures

List of Tables

Chapter 1

Introduction

1.1 Overview

Globular clusters are roughly spherical collections of $\sim 10^5 - 10^6$ stars. Our own Galaxy contains about $150 - 200$ globular clusters. They are almost isotropically distributed around the center of the Galaxy, with more than half of the observed clusters being within 10 kpc from the Galactic center. However, the distribution extends to much larger distances, with a few clusters being beyond 50 kpc.

To a good approximation, globular clusters can be regarded as spherical self-gravitating systems containing a large number of point-mass particles, interacting in a Newtonian gravitational field. Despite the appealing simplicity of such systems, a systematic understanding of their evolution, and the various physical processes that are involved, is still incomplete.

1.1.1 Basic Properties of Globular Clusters

Globular clusters are thought to contain some of the oldest stars in the Galaxy. The ages of globular clusters are determined mainly from their Hertzsprung-Russell (HR, or "Color-Magnitude") diagrams, which show a clear "turn-off" point, at which stars leave the main sequence and evolve for the first time up the giant branch. As the cluster gets older, the position of the turn-off, which indicates the point when

the Hydrogen in the stellar core has been converted to Helium, moves to stars of lower mass and later spectral type. Hence the position of the turn-off point on the observed HR diagram can be used in principle to determine the time since the stars, and presumably the entire cluster, were formed. Using this technique, the ages of Galactic globular clusters have been found to be in the range $10 - 20 \times 10^9$ yr.

The structure of a typical globular cluster is characterized by a dense central region, or core, and a more extended and lower-density outer envelope, or halo. The density (and hence the surface brightness) often varies by several orders of magnitude from the core to the halo. Hence globular clusters are usually described by their core radius, r_c, generally defined as the radius at which the surface brightness is half its central value, and a tidal radius, r_t, at which the density falls to zero. For most clusters, r_c lies in the range $0.2 - 10$ pc, and r_t/r_c lies between 10 and 100. The masses of globular clusters are distributed in the range $\sim 10^4 - 10^6 M_\odot$, with a peak around $10^5 M_\odot$.

1.1.2 Equilibrium Models

In idealized models of globular clusters, the effect of stellar encounters is ignored (as a first approximation), and a steady state model is constructed, in which the overall structure of the cluster does not change with time. Stellar encounters, and other effects are then introduced as perturbations which cause the cluster to evolve along a sequence of steady state models.

We first consider the simplifying assumptions made in a steady state, or "zero-order" model. (A) Although the gravitational potential of the cluster is due to combined gravity of the discrete stars contained in it, we ignore the granularity of the system in determining the potential. This makes the gravitational potential ϕ a slowly varying function of position alone. (B) The gravitational potential ϕ, the velocity distribution function f, and all other cluster properties are independent of time. (C) The cluster is spherically symmetric. This makes f a function of r, v_r and v_t, where v_r is the radial velocity of a star at a distance r from the center, and v_t is its transverse velocity. The potential ϕ is also a function of r only.

These assumptions imply that the energy per unit mass E, and angular momentum per unit mass J of a star is constant. The energy and angular momentum per unit mass is given by,

$$E = \frac{1}{2}v^2 + \phi(r), \tag{1.1}$$

$$J = rv_t = rv\sin\theta, \tag{1.2}$$

where θ is the angle between $\mathbf{r}$ and $\mathbf{v}$.

The velocity distribution function $f(\mathbf{r}, \mathbf{v}, t)$ is defined so that $f(\mathbf{r}, \mathbf{v}, t)\mathbf{drdv}$ is the number of stars at time t in the volume element $\mathbf{dr} = dx\,dy\,dz$ centered at $\mathbf{r}$, and in the velocity space element $\mathbf{dv} = dv_x\,dv_y\,dv_z$ centered at $\mathbf{v}$. The basic constraint on the form of f (only for the zero-order approximation in which stellar encounters are ignored) is the collisionless Boltzmann equation,

$$\frac{\partial f}{\partial t} + \sum_i a_i \frac{\partial f}{\partial v_i} + \sum_i v_i \frac{\partial f}{\partial x_i} = 0, \tag{1.3}$$

where x_i is one of the three coordinates x, y, or z, and a_i is the acceleration of the particle, given by $a_i = -\partial\phi/\partial x_i$. The number density is then given by

$$n(\mathbf{r}, t) = \int f(\mathbf{r}, \mathbf{v}, t)\mathbf{d}v. \tag{1.4}$$

The collisionless Boltzmann equation determines the dynamical evolution of a system satisfying condition (A), subject to Poisson's Law,

$$\nabla^2\phi(\mathbf{r}, t) = 4\pi G\rho. \tag{1.5}$$

Several analytic models for Globular clusters are available, which satisfy the conditions (A), (B) and (C) given above. These models are most often used as initial conditions for numerical simulations of globular clusters, and to fit observed clusters. One popular spherical model is the polytropic sphere, which is specified by assuming an isotropic velocity distribution everywhere, and with a phase-space distribution

function

$$f = \kappa_1(-E)^p \quad \text{for } E < 0, \text{and } 0 \text{ for } E > 0, \tag{1.6}$$

where κ_1 is a constant, and the potential ϕ is taken to be zero at the cluster surface. Using equation (1.4) and equation (1.1), we get for $p > -1$,

$$\rho(r) = \kappa_2[-\phi(r)]^{p+3/2}, \tag{1.7}$$

where κ_2 is a constant. This is the basic equation for a polytrope, with the index $n = p + 3/2$. The polytrope with $n = 5$ is known as a Plummer model, and is used widely as an initial model for numerical simulations of clusters. Despite having an infinite extent (the density falls to zero only at infinity), this model resembles clusters with a compact core and an extended halo. Its physical properties are given by simple analytic expressions,

$$\rho(r) = \frac{3M}{4\pi R^3} \times \frac{1}{[1 + r^2/R^2]^{5/2}}, \tag{1.8}$$

$$\phi(r) = \frac{-GM}{R} \times \frac{1}{[1 + r^2/R^2]^{1/2}} = -2[v_m(r)]^2, \tag{1.9}$$

where v_m is the three-dimensional velocity dispersion. The scale factor R is related to $\rho(0)$ and $v_m(0)^2$ through equations (1.8) and (1.9).

Another class of models which are widely used to fit observed cluster profiles, are the "lowered Maxwellian", or "King" models, with

$$f = K(e^{-BE} - e^{-BE_e}) \quad \text{if } E < E_e, \text{ and } 0 \text{ otherwise.} \tag{1.10}$$

Physically, this distribution function takes into account the presence of a tidal radius r_t around the cluster due to the presence of the Galactic tidal field. Any star that goes beyond the tidal radius effectively becomes unbound from the cluster. The presence of a tidal radius gives the King model a finite extent, with $E_e = \phi(r_t)$. In dimensionless form, King models are parametrized by r_t/r_c only, where r_c is the core radius.

1.1.3 Dynamical Evolution

Steady state models can provide a zero-order approximation for the structure of a cluster at any given time. However, as stated earlier, due to the effect of perturbations due to stellar interactions and other effects, a cluster evolves slowly from one steady-state model to the next. The main source of these perturbations are as follows: (a) The granularity of the gravitational field, due to interactions between stars, which causes small local perturbations as stars pass by one another; (b) External gravitational fields, particularly due to the presence of the Galaxy; and (c) Changes in the properties of individual stars, as a result of stellar evolution, or close interactions.

When encounters between stars are important, the evolution of the distribution function $f(\mathbf{r}, \mathbf{v}, t)$ is given by the Boltzmann equation, which generalizes equation (1.3) as

$$\frac{Df}{Dt} = \frac{\partial f}{\partial t} + \sum_i a_i \frac{\partial f}{\partial v_i} + \sum_i v_i \frac{\partial f}{\partial x_i} = \left(\frac{\partial f}{\partial t}\right)_{enc}, \tag{1.11}$$

where the effect of encounters between particles is included in the $(\partial f/\partial t)_{enc}$ term. For small perturbations produced by distant interactions between stars, a process known as two-body relaxation, the encounter term is given by (see Spitzer 1987 for a full derivation),

$$\left(\frac{\partial f}{\partial t}\right)_{enc} = -\sum_{i=1}^{3} \frac{\partial}{\partial v_i}(f\langle \Delta v_i \rangle) + \frac{1}{2}\sum_{i,j=1}^{3} \frac{\partial^2}{\partial v_i \partial v_j}(f\langle \Delta v_i \Delta v_j \rangle). \tag{1.12}$$

The quantities $\langle \Delta v_i \rangle$ and $\langle \Delta v_i \Delta v_j \rangle$ are the "diffusion coefficients", representing the mean and mean-square changes in the velocity of stars due to interactions. The Boltzmann equation (eq. [1.11]), with the encounter term substituted from equation (1.12), is called the Fokker-Planck equation. To understand the dynamical evolution of globular clusters, one must solve the Fokker-Planck equation in some form, in order to take into account the effect of two-body relaxation. In most numerical studies, the Fokker-Planck solution is solved assuming various initial models and boundary conditions, and then the perturbations due to external fields and due to changes in the properties of stars (items (b) and (c) mentioned above) are taken into account sep-

arately, by modifying the properties of stars (for stellar evolution), or changing the boundary conditions at the tidal radius (for the Galactic tidal field) as a function of time.

The inevitable final consequence of two-body relaxation in a cluster, is the development of the "gravothermal instability" in a cluster, which causes the core of the cluster to become extremely small, but with a very high density of stars. Since the core is on average denser than the halo, the mean kinetic energies of stars (i.e., the dynamical temperature) in the core is higher, which leads to a constant loss of energy from the core to the halo through conduction. Through two-body relaxation, slower moving stars acquire energy through interactions in the core, and then carry the energy out to the halo in the form of translational energy. The constant loss of energy from the core causes the core to shrink, which in turn causes the temperature to go up further. In this way, two-body relaxation leads to the development of the gravothermal instability. This evolution takes place on a fundamental timescale, known as the "relaxation time" t_r, which is related to the dynamical time as $\sim t_{relax} = N/\ln \gamma N \cdot t_{dyn}$, where $\gamma \simeq 0.1$ is a constant. The dynamical time, also referred to as the "crossing time" is approximately the time required for a star with the mean velocity to cross the cluster, and is typically $\sim 10^5 - 10^7$ yr. On the other hand, the relaxation time is usually several orders of magnitude larger, and ranges from $10^8 - 10^{12}$ yr. The relaxation time represents the timescale on which the global structure of the clusters evolves due to two-body relaxation.

We now mention some of the other significant physical processes that affect the overall evolution of globular clusters. We discuss each one of these issues in detail in later sections and chapters, where they are relevant.

(A) **Two-Body Relaxation:** Clusters are spherically symmetric, self-gravitating systems. Energy exchange between stars takes place through two-body scattering events, and is modeled by the Fokker-Planck equation. Timescale $\sim \tau_{relax} \sim 10^8 - 10^{12}$ yr $\propto N/\ln N \cdot t_{dyn}$.

(B) **Stellar Evolution:** Mass loss due to stellar evolution reduces the binding energy of the cluster. Internal evolution of binaries is also important. Timescale $\tau_{stellar} \sim 10^6 - 10^{12}$ yr.

(C) **Tidal Field of the Galaxy:** Effectively imposes a Roche lobe on the cluster in the potential of the Galaxy. Leads to the escape of stars if they go beyond the tidal boundary. Timescale $\tau_{tidal} \sim 10^7 - 10^{12}$ yr.

(D) **Mass Segregation:** Massive stars (and binaries), in an effort to achieve equipartition, sink into the core, accelerating core collapse. Timescale $\tau_{seg} \sim \tau_{relax}(\bar{m}/m)$, where m is the mass of the component in question, and $\bar{m}$ is the mean mass in the cluster.

(E) **Binary Interactions:** Binaries provide a much larger interaction cross section than single stars, and hence can lead to strong (close) interactions more frequently than single stars. Interactions with binaries release energy at the expense of the internal binding energy of the binary. They can serve as energy sources, which can support the core against collapse.

(F) **Tidal shocking by the Galactic Disk:** "Shock heating" of the cluster due to a passage through the disk, or close to the bulge, can accelerate the relaxation process and increase the mass loss rate. Note however, that although the term "shock heating" is often used to describe the energy infused into the cluster due to brief yet strong tidal interactions with the Galactic disk or bulge, this is not a shock in the conventional sense (there is no shock wave, no collisional fluid, nor are there any jump conditions). Timescale $\tau_{shock} \sim 10^7 - 10^9$ yr.

(G) **Stellar Collisions:** Increased interaction cross sections due to the presence of binaries, and Giant stars can lead to greatly enhanced collision rates in dense cluster cores. The Massive stars formed as a result evolve more quickly, leading to further mass loss, effectively heating the cluster.

1.2 Astrophysical Motivation

We now discuss our main motivations for studying globular cluster evolution taking into account new observations of globular clusters, and present some of the outstanding questions relating to the topic. The dynamical evolution of dense star clusters is a problem of fundamental importance in theoretical astrophysics. But many aspects of the problem have remained unresolved in spite of years of numerical work and improved observational data.

On the theoretical side, some key unresolved issues include the role played by primordial binaries and their dynamical interactions in the overall cluster dynamics and in the production of exotic sources (Hut et al. 1992), the effect of the Galactic tidal field, the interplay between stellar evolution and the rate of escape of stars from the cluster, (Takahashi & Portegies Zwart 2000), and the importance of tidal shocking for the long-term evolution and survival of globular clusters in the Galaxy (Gnedin, Lee & Ostriker 1999).

On the observational side, we now have many large data sets providing a wealth of information on blue stragglers, X-ray sources and millisecond pulsars, all found in large numbers in dense clusters (e.g., Bailyn 1995; Camilo et al. 2000; Piotto et al. 1999). Although it is clear that these objects are produced at high rates through dynamical interactions in the dense cluster cores, the details of the formation mechanisms, and in particular the interplay between binary stellar evolution and dynamical interactions, are far from understood.

With the Hubble Space Telescope (HST), stars well below the main-sequence turnoff can also now be studied in detail in globular clusters, even in dense cluster cores. For the nearest clusters, color–magnitude diagrams extending to $V \approx 27$ reach main-sequence stars and white dwarfs as faint as $M_V \approx 13$, corresponding to main-sequence masses close to $0.1\,M_\odot$. From deep color–magnitude diagrams, detailed luminosity and mass functions can be obtained, providing direct constraints on theoretical models, and, in particular, on mass segregation effects (Ferraro et al. 1997a; Marconi et al. 1998; Sosin & King 1997). Observations such as these have pro-

vided a wealth of new information about globular clusters, and in the process have also presented new challenges for theoretical models. For example, the deficiency of low-mass stars in NGC 6397 compared to three other clusters with similar low metallicities suggests that tidal shocks may have affected its evolution significantly (Piotto et al. 1997). The Globular clusters 47 Tuc and M15 have both been the targets of several highly successful searches for pulsars (Anderson 1992; Robinson et al. 1995; Camilo et al. 2000). The observed properties of pulsars in these clusters are found to be very different. The pulsars in 47 Tuc are all millisecond pulsars, and most are in short-period binaries, while those in M15 are mostly single recycled pulsars with longer pulse periods. This suggests that these two clusters may provide very different dynamical environments for the formation of recycled pulsars. In order to understand these issues fully, to relate our theoretical understanding to observations, and to make predictions about the fate of globular clusters, requires that we take into account *all* of the relevant physical processes accurately, since it is the interplay between them that gives these systems their rich phenomenology. In this effort, we must rely increasingly on sophisticated simulations, which can realistically incorporate the various physical processes, and provide new insights.

With this perspective in mind, we now list the main questions that will be addressed in our study: (A) What is the relative importance of the Galactic tidal field in determining the final fate of globular clusters? How long do globular clusters survive in the tidal field of the Galaxy?

(B) What is the effect of stellar evolution on the dynamics of a globular cluster? Does mass loss due to stellar evolution affect the core-collapse time, or the rates of physical processes such as a tidal stripping of stars?

(C) What role does the mass stratification instability (described by Spitzer) play in systems with a very steep mass spectrum? Does the presence of a heavier component in the core cause the core to decouple from the rest of the cluster and collapse as an independent subsystem consisting of the heavier stars? How do very low-mass objects evolve in a cluster? Do clusters contain low-mass objects such as brown-dwarfs and

planets?

(D) Can the distributions and properties of well-known tracers of dynamical interactions, such as blue stragglers, cataclysmic variables, X-ray sources and millisecond pulsars, be explained based on our understanding stellar interactions in the cores of globular clusters?

(E) What is the role played by primordial binaries in the overall dynamical evolution of globular clusters, and, in particular, in supporting clusters against core collapse? Is it possible for the core of a globular cluster to re-expand due to the energy injected during interactions of stars with primordial binaries, leading to "gravothermal oscillations" of the core?

1.3 Overview of Numerical Methods

1.3.1 Monte-Carlo Methods

Following the pioneering work of Hénon (1971a,b), many numerical simulations of globular cluster evolution were undertaken in the early 1970's, by two groups, at Princeton and Cornell, using different Monte-Carlo methods, now known as the "Princeton method" and the "Cornell method". In the Princeton method, the orbit of each star is integrated numerically, while the diffusion coefficients for the change in velocity $\Delta\mathbf{v}$ and $(\Delta v)^2$ (which are calculated analytically) are selected to represent the average perturbation over an entire orbit. Energy conservation is enforced by requiring that the total energy be conserved in each radial region of the cluster. The Princeton method assumes an isotropic, Maxwellian velocity distribution of stars to compute the diffusion coefficients, and hence does not take in to account the anisotropy in the orbits of the field stars. One advantage of this method is that, since it follows the evolution of the cluster on a dynamical timescale, it is possible to follow the initial "violent relaxation" phase more easily. Unfortunately, for the same reason, it also requires considerably more computing time compared to other versions of the Monte-Carlo method. In the Cornell method, also known as the "Orbit-averaged

Monte-Carlo method", the changes in energy E and angular momentum J per unit time (averaged over an orbit) are computed analytically for each star. Hence, the time consuming dynamical integration of the orbits is not required. In addition, since the diffusion coefficients are computed for both ΔE *and* ΔJ, the Cornell method does take in to account the anisotropy in the orbits of the stars. The "Hénon method" is a variation of the Cornell method, in which the velocity perturbations are computed by considering an encounter between pairs of neighboring stars. This also allows the local 2-D phase space distribution $f(E, J)$ to be sampled correctly. Our code is based on a modified version of Hénon's method. We have modified Hénon's algorithm for determining the timestep and computing the representative encounter between neighboring stars. We present a detailed description the basic method and our modifications in Chapter 2.

In the simplest case of a spherical system containing N point masses, Hénon's algorithm can be summarized as follows. We begin by assigning to each star a mass, radius and velocity by sampling from a spherical and isotropic distribution function (for example, the Plummer model). Once the positions and masses of all stars are known, the gravitational potential of the cluster is computed assuming spherical symmetry. The energy and angular momentum of each star are then calculated. Energy and angular momentum are perturbed at each timestep to simulate the effects of two-body encounters. The perturbations depend on each star's position and velocity, and on the density of stars in its neighborhood. The timestep should be a fraction of the relaxation time for the cluster (which is larger than the dynamical time by a factor $\propto N/\ln \gamma N$). The perturbation of the energy and angular momentum of a star at each timestep therefore represents the cumulative effect of many small (and distant) encounters with other stars. Under the assumption of spherical symmetry, the cross-sections for these perturbations can be computed analytically. The local number density is computed using a sampling procedure. Once a new energy and angular momentum is assigned to each star, a new realization of the system is generated by assigning to each star a new position and velocity in an orbit that is consistent with its new energy and angular momentum. In selecting a new position for each star along

its orbit, each position is weighted by the amount of time the star spends around that position. Using the new positions, the gravitational potential is then recomputed for the entire cluster. This procedure is then repeated over many timesteps. After every timestep, all stars with positive total energy (cf. §2.7) are removed from the computation since they are no longer bound to the cluster and are hence considered lost from the cluster instantly on the relaxation timescale. The method allows stars to have arbitrary masses and makes it very easy to allow for a stellar mass spectrum in the calculations.

1.3.2 Direct Integration of the Fokker-Planck Equation

In addition to Monte-Carlo and N-body simulations, a new method was developed, mainly by Cohn and collaborators, based on the direct numerical integration of the orbit-averaged Fokker-Planck equation (Cohn 1979, 1980; Statler, Ostriker & Cohn 1987; Murphy & Cohn 1988). Unlike the Monte-Carlo methods, the direct Fokker-Planck method constructs the (smooth) distribution function of the system on a grid in phase space, effectively providing the $N \rightarrow \infty$ limit of the dynamical behavior. The original formulation of the method used a 2-D phase space distribution function $f(E, J)$ (Cohn 1979). However, the method was later reduced to a 1-D form using an isotropized distribution function $f(E)$ (Cohn 1980). The reduction of the method to one dimension speeded up the calculations significantly. In addition, the use of the Chang & Cooper (1970) differencing scheme provided much better energy conservation compared to the original 2-D method. The 1-D method provided very good results for isolated clusters, in which the effects of velocity anisotropy are small. The theoretically predicted emergence of a power-law density profile in the late stages of evolution for isolated single-component systems has been clearly verified using this method (Cohn 1980). Calculations that include the effects of binary interactions, including primordial binaries, have also allowed the evolution to be followed beyond core collapse (Gao et al. 1991). However, results obtained using the 1-D method showed substantial disagreement with N-body results for tidally truncated clusters, in which the evaporation rate is dramatically affected by the velocity anisotropy. Ignoring the

velocity anisotropy led to a significant overestimate of the evaporation rate from the cluster, resulting in shorter core-collapse times for tidally truncated clusters (Portegies Zwart et al. 1998). A recent implementation of the Fokker-Planck method by Drukier et al. (1999) has extended the algorithm to allow a 2-D distribution function, while also improving the energy conservation. A similar 2-D method has also been developed by Takahashi (1995, 1996, 1997). The new implementations produce much better agreement with N-body results (Takahashi & Portegies Zwart 1998), and can also model the effects of mass loss due to stellar evolution (Takahashi & Portegies Zwart 1999), as well as binary interactions (Drukier et al. 1999).

For many years direct N-body simulations were limited to systems with $N \lesssim 10^3$ stars. New, special-purpose computing hardware such as the GRAPE (Makino et al. 1997) now make it possible to perform direct N-body simulations with up to $N \sim 10^5$ single stars (Hut & Makino 1999), but the inclusion of a significant fraction of primordial binaries in these simulations remains prohibitively expensive. The large dynamic range of the orbital timescales of the stars in the cluster presents a serious difficulty for N-body simulations. The orbital timescales can be as small as the periods of the tightest binaries. The direct integration of stellar orbits is especially plagued by this effect. These difficulties are overcome using techniques such as individual integration timesteps, and various schemes for regularizing binaries (see, e.g., Aarseth 1998 for a review). These short-cuts introduce specific selection effects, and complicate code development considerably. Instead, in the Monte-Carlo methods, individual stellar orbits are represented by their constants of the motion (energy E and angular momentum J for a spherical system) and perturbations to these orbits are computed periodically on a timestep that is a fraction of the relaxation time. Thus the numerical integration proceeds on the natural timescale for the overall dynamical evolution of the cluster. Note also that, because of exponentially growing errors in the direct integration of orbits, N-body simulations, just like Monte-Carlo simulations, can only provide a statistically correct representation of cluster dynamics (Goodman et al. 1993; Hernquist, Hut, & Makino 1993).

A great advantage of the Monte-Carlo method is that it makes it particularly easy

to add more complexity and realism to the simulations one layer at a time. The most important processes that we will focus on initially will be stellar evolution and mass loss through a tidal boundary. Interactions of single stars with primordial binaries, binary-binary interactions, stellar evolution in binaries, and a detailed treatment of the influence of the Galaxy, including tidal shocking of the cluster when it passes through the galactic disk, will be incorporated subsequently.

Recent improvements in algorithms and available computational resources have allowed meaningful comparisons between the results obtained using different numerical methods (see for example the "Collaborative Experiment" by Heggie et al. 1999). However, there still remain substantial unresolved differences between the results obtained using various methods. For example, the lifetimes of clusters computed recently using different methods have been found to vary significantly. Lifetimes of some clusters computed using direct Fokker-Planck simulations by Chernoff & Weinberg (1990) are up to an order of magnitude shorter than those computed using N-body simulations and a more recent version of the Fokker-Planck method (Takahashi & Portegies Zwart 1998). It has been found that, in many cases, the differences between the two methods can be attributed to the lack of an appropriate discrete representation of the cluster in the Fokker-Planck simulations. This can lead to an over-estimate of the mass-loss rate from the cluster, causing it to disrupt sooner. Recently, new calibrations of the mass loss in the Fokker-Planck method (Takahashi & Portegies Zwart 1999) that account for the slower mass loss in discrete systems, has led to better agreement between the methods. The limitation of N-body simulations to small N (especially for clusters containing a large fraction of primordial binaries) makes it particularly difficult to compare the results with Fokker-Planck calculations, which are effectively done for very large N (Portegies Zwart et al. 1998, Heggie et al. 1999). This gap can be filled very naturally with Monte-Carlo simulations, which can be used to cover the entire range of N's not accessible by other methods.

Chapter 2

The Monte-Carlo Method

2.1 Overview

The Monte-Carlo methods were first used to study the development of the gravothermal instability (Spitzer & Hart 1971a,b; Hénon 1971a,b) and to explore the effects of a massive black hole at the center of a globular cluster (Lightman & Shapiro 1977). In those early studies, the available computational resources limited the number of particles used in the Monte-Carlo simulations to $\lesssim 10^3$. Since this is much smaller than the real number of stars in a globular cluster ($N \sim 10^5 - 10^6$), each particle in the simulation represents effectively a whole spherical shell containing many stars, and the method provides no information about individual objects and their dynamical interactions. More recent implementations have used up to $\sim 10^4 - 10^5$ particles and have established the method as a promising alternative to direct N-body integrations (Stodólkiewicz 1986; Giersz 1998). Monte-Carlo simulations have also been used to study specific interaction processes in globular clusters, such as tidal capture (Di Stefano & Rappaport 1994), interactions involving primordial binaries (Hut, McMillan, & Romani 1992) and stellar evolution (Portegies Zwart et al. 1997). However, in all these studies the background cluster was assumed to have a *fixed structure*, which is clearly not realistic. Instead, the main goal of our study is to perform Monte-Carlo simulations of cluster dynamics treating both the cluster itself and all relevant interactions self-consistently, including all dynamical interactions involving primordial

binaries. This idea is particularly timely because the latest generation of parallel supercomputers now makes it possible to do such simulations for a number of objects equal to the actual number of stars in a globular cluster. Using the correct number of stars in a cluster simulation ensures that the relative rates of different dynamical processes (which all scale differently with the number of stars) are correct. This is crucial if many different dynamical processes are to be incorporated, as we plan to do in this study.

Our basic algorithm for doing stellar dynamics is based on the "orbit-averaged Monte-Carlo method" developed by Hénon (1971a,b). The method was later used and improved by Stodólkiewicz (1982, 1985, 1986). It has also recently been used by Spurzem & Giersz (1996) to follow the evolution of hard three-body binaries in a cluster with equal point-mass stars. New results using Stodólkiewicz's version of the method were also presented recently by Giersz (1998). In earlier implementations of the Monte-Carlo method with $N \sim 10^3$, each particle in the simulation was a "superstar," representing many individual stars with similar orbital properties. In our implementation, with $N \sim 10^5 - 10^6$, we treat each particle in the simulation as a single star. We have also modified Hénon's original algorithm to allow the timestep to be made much smaller in order to resolve the dynamics in the core more accurately.

We now describe our implementation of the Monte-Carlo method in detail. For completeness, we also include some of the basic equations of the method. For derivations of these equations, and a more detailed discussion of the basic method, see Hénon (1971b), Stodólkiewicz (1982), and Spitzer (1987).

2.2 Initial Conditions

The initial model is assumed to be in dynamical equilibrium, so that the potential does not change on the crossing timescale. This is important since the Monte-Carlo method uses a timestep which is of the order of the relaxation time, and hence cannot handle the initial phase of "violent relaxation" during which the potential changes on the dynamical timescale. Under the assumption of spherical symmetry, the distribution

function for such an equilibrium system can be written in the form $f = \Psi(E, J)$, where E and J are the energy per unit mass, and angular momentum per unit mass,

$$E = \Phi(r) + \frac{1}{2}(v_r^2 + v_t^2), \tag{2.1}$$

$$J = rv_t. \tag{2.2}$$

Here r is the distance from the cluster center, v_r is the radial velocity, v_t is the transverse velocity, and $\Phi(r)$ is the gravitational potential. In principle, the initial distribution function $\Psi(E, J)$ can be arbitrary. However, in practice, computing a self-consistent potential for an arbitrary distribution function can be quite difficult. Since the method requires the initial potential $\Phi(r)$ to be known, a simple initial model is usually selected so as to allow the potential to be computed quasi-analytically. Common examples are the sequence of King models and the Plummer model.

Once the number of stars N is selected, the initial condition is constructed by assigning to each star values for r, v_r, v_t, and m, consistent with the selected model. Once the positions and masses of all the stars are known, the gravitational potential Φ is computed as a function of distance from the center. The energy per unit mass E, and angular momentum per unit mass J of each star are then computed using equations (1) and (2).

2.3 The Gravitational Potential

We compute the mean potential of the cluster by summing the potential due to each star, under the assumption of spherical symmetry. We use only the radial position r of each star (since we assume spherical symmetry, we can neglect the angular positions of the stars, to a very good approximation). We begin by sorting all the stars by increasing radius. Then the potential at a point r, which lies between two stars at positions r_k and r_{k+1}, is given by

$$\Phi(r) = G\left(-\frac{1}{r}\sum_{i=1}^{k} m_i - \sum_{i=k+1}^{N}\frac{m_i}{r_i}\right). \tag{2.3}$$

For any two neighboring stars at distances r_k and r_{k+1}, the mass contained within the radius r remains constant for $r_k < r < r_{k+1}$. Hence, we can compute the potential at r, if the potentials $\Phi_k = \Phi(r_k)$ and $\Phi_{k+1} = \Phi(r_{k+1})$ are known, as

$$\Phi(r) = \Phi_k + \left(\frac{1/r_k - 1/r}{1/r_k - 1/r_{k+1}}\right)(\Phi_{k+1} - \Phi_k). \tag{2.4}$$

At each timestep, we store pre-computed values of $\Phi_k = \Phi(r_k)$, for each star k in the cluster. The potential at an arbitrary point r can then be quickly computed simply by finding the index k such that $r_k \leq r \leq r_{k+1}$ and then using equation (2.4).

We now describe the process of evolving the system through one complete timestep.

2.4 Two-Body Relaxation and Timestep Selection

We simulate the effect of interactions during each timestep Δt by perturbing the energy and angular momentum of each star in the cluster. The perturbations ΔE and ΔJ for a star are determined by computing a single *effective* encounter between the star and its nearest neighbor (in terms of distance from the center, since we assume spherical symmetry). During such an encounter, the two stars exchange kinetic energy, but the total energy is conserved. In the center of mass frame of the two interacting stars, the magnitude of the velocity does not change; instead the velocity is deflected through an angle β.

In the original method described by Hénon (1971b), the timestep used was a small fraction of the relaxation time for *the entire cluster*. Although the timestep computed in this way is suitable for the outer regions of the cluster, it is too large to provide an accurate representation of the relaxation in the core, especially in the later stages of cluster evolution where the relaxation time in the core can be many orders of magnitude smaller than in the outer regions. This caused the inner regions of the

cluster to be under-relaxed. The limited computational resources available at that time did not permit the timestep to be made much smaller, without slowing down the computation to a crawl. The greatly increased computational power available today allows us to use a timestep that is small enough to resolve the relaxation process in the core, even for systems with $N \gtrsim 10^5$.

To provide an accurate description of the overall relaxation of the cluster, each effective encounter should give the correct mean value of the change in energy at each position. We achieve this by selecting the effective deflection angle β_e for the encounter (in the center of mass frame of the two interacting stars) as follows. If the masses of the two stars are m_1 and m_2, and their velocities v_1 and v_2, respectively, then the kinetic energy changes can be written as

$$\Delta KE_1 = m_1 v_1 \Delta v_1 + \frac{1}{2} m_1 (\Delta v_1)^2, \tag{2.5}$$

$$\Delta KE_2 = m_2 v_2 \Delta v_2 + \frac{1}{2} m_2 (\Delta v_2)^2, \tag{2.6}$$

where Δv_1 and Δv_2 are the changes in the velocities during the encounter. Since the total kinetic energy in each encounter is conserved, the mean value of the first terms on the RHS of equations (5) and (6) must equal the mean value of the second terms (with the opposite sign). This indicates that in order to get a good representation of the energy exchange between stars in the relaxation process, we must consider the mean value of $m_1(\Delta v_1)^2$ during each timestep.

The change in velocity Δv_1 during an encounter with a deflection angle β, can be calculated from elementary mechanics as (see, e.g., Spitzer 1987, eq. [2-6]),

$$(\Delta v_1)^2 = 4 \frac{m_2^2}{(m_1 + m_2)^2} w^2 \sin^2(\beta/2), \tag{2.7}$$

where w is the relative speed of the two stars before the encounter. The mean overall *rate* of change in the velocity $< (\Delta v_1)^2 >$ due to many distant (weak) encounters of the star with other cluster stars can then be calculated by averaging over the impact parameter (cf. Spitzer 1987, eq. [2-8]). Using this, the mean change in the velocity

in the time Δt is given by

$$< (\Delta v_1)^2 >= 8\pi G^2 \nu \Delta t < m_2^2 w^{-1} > \ln \Lambda, \tag{2.8}$$

where $\ln \Lambda \equiv \ln(\gamma N)$ is the Coulomb logarithm (γ is a constant ~ 0.1; see §3.1), and ν is the local number density of stars. We obtain the correct mean value of $m_1(\Delta v_1)^2$ by equating the RHS of equations (7) and (8), giving

$$< 4\frac{m_1 m_2^2}{(m_1+m_2)^2} w^2 \sin^2(\beta/2) >= 8\pi G^2 \nu \Delta t < m_1 m_2^2 w^{-1} > \ln(\gamma N). \tag{2.9}$$

Equation (9) relates the timestep Δt to the deflection angle β for the encounter. Thus, in order to get the correct mean value of $m_1(\Delta v_1)^2$ for the star during the time Δt, we can define the *effective* deflection angle β_e for the representative encounter, as

$$\sin^2(\beta_e/2) = 2\pi G^2 \frac{(m_1+m_2)^2}{w^3} \nu \Delta t \ln(\gamma N). \tag{2.10}$$

In addition to using the correct mean value of $m_1(\Delta v_1)^2$, we can also require that its variance be correct. To compute the variance, we must calculate the mean value of $(\Delta v_1)^4$. Using equation (2.7), we have

$$(\Delta v_1)^4 = 16\frac{m_2^4}{(m_1+m_2)^4} w^4 \sin^4(\beta/2). \tag{2.11}$$

We then use Spitzer's equation (2-5), and again integrate over the impact parameter to get the mean value of $(\Delta v_1)^4$ in the time Δt,

$$< (\Delta v_1)^4 >= 16\pi G^2 \frac{m_2^4}{(m_1+m_2)^2} w \nu \Delta t. \tag{2.12}$$

Comparing equations (11) and (12), we see that, in order to have the correct variance of $m_1(\Delta v_1)^2$, we should have

$$\sin^4(\beta_e/2) = \pi G^2 \frac{(m_1+m_2)^2}{w^3} \nu \Delta t. \tag{2.13}$$

Consistency between equations (10) and (13) gives the relation between the number of stars in the system, and the effective deflection angle that must be used,

$$\sin^2(\beta_e/2) = \frac{1}{2\ln(\gamma N)}. \tag{2.14}$$

This relation indicates that for large N, the effective deflection angle must be small, while as N decreases, close encounters become more important. If the timestep is too large, then $< \sin^2(\beta/2) >$ is also too large, and the system is under-relaxed. Hence the timestep used should be sufficiently small so as to get a good representation of the relaxation process in the cluster. In addition, the local relaxation time varies greatly with distance from the cluster center. In practice we use the shortest relaxation time in the core to compute the timestep. We first evaluate the local density ρ_c in the core and the approximate core radius $r_c = (3v_c^2/4\pi G\rho_c)^{1/2}$. We then compute the timestep Δt using equation (2.10) and requiring that the average value of $\sin^2(\beta_e/2)$ for the stars within the core radius r_c be sufficiently small. The value of $\sin^2(\beta_e/2)$ given by equation (2.14) varies only slightly between 0.046 and 0.072 for N between 10^4 and 5×10^5 (assuming $\gamma \simeq 0.1$). Hence for all our simulations, we require that $\sin^2(\beta_e/2) \lesssim 0.05$.

Equation (10) is then used to compute the effective deflection angle for all stars in the cluster. The local number density ν is computed by averaging over the nearest p stars. We find that using a value of p between 20 and 50 gives the best results for $N \sim 10^5$. We find that the difference in the core-collapse times obtained for various test models using values of p between 20 and 50 is less than 1%. Of course, the value of p should not be too large so as to maintain a truly local estimate of the number density. We use a value of $p = 40$ in all our calculations, which gives consistently good agreement with published results.

2.5 Computing the Perturbations ΔE and ΔJ during an Encounter

To compute the velocity perturbation during each timestep, a single representative encounter is computed for each star, with its nearest neighbor in radius. Selecting the nearest neighbor ensures that the correct local velocity distribution is sampled, and also accounts for any anisotropy in the orbits. Due to spherical symmetry, selecting the nearest neighbor in radius is equivalent to selecting the nearest neighbor in 3-D, since only the velocity (and not the position) of the nearest neighbor is used in the encounter. Following Hénon's notation, we let (r, v_r, v_t) and (r', v_r', v_t') represent the phase space coordinates of the two interacting stars, with masses m and m', respectively. In addition to these parameters, the angle ψ of the plane of relative motion defined by ($\mathbf{r}' - \mathbf{r}$, $\mathbf{v}' - \mathbf{v}$) with some reference plane is selected randomly between 0 and 2π, since the distribution of field stars is assumed to be spherically symmetric.

We take our frame of reference such that the z axis is parallel to $\mathbf{r}$, and the (x, z) plane contains $\mathbf{v}$. Then the velocities of the two stars are given by

$$\mathbf{v} = (v_t, 0, v_r),\ \mathbf{v}' = (v_t' \cos\phi, v_t' \sin\phi, v_r'), \tag{2.15}$$

where ϕ is also randomly selected between 0 and 2π, since the transverse velocities are isotropic because of spherical symmetry. The relative velocity $\mathbf{w} = (w_x, w_y, w_z)$ is then

$$\mathbf{w} = (v_t' \cos\phi - v_t, v_t' \sin\phi, v_r' - v_r). \tag{2.16}$$

We now define two vectors $\mathbf{w}_1$ and $\mathbf{w}_2$ with the same magnitude as $\mathbf{w}$, such that $\mathbf{w}_1$, $\mathbf{w}_2$, and $\mathbf{w}$ are mutually orthogonal. The vectors $\mathbf{w}_1$ and $\mathbf{w}_2$ are given by

$$\mathbf{w}_1 = (w_y w/w_p, -w_x w/w_p, 0), \tag{2.17}$$

$$\mathbf{w}_2 = (-w_x w_z/w_p, -w_y w_z/w_p, w_p), \tag{2.18}$$

where $w_p = (w_x^2 + w_y^2)^{1/2}$. The angle ψ is measured from the plane containing the vectors $\mathbf{w}$ and $\mathbf{w_1}$. The relative velocity of the two stars after the encounter is given by

$$\mathbf{w}^\star = \mathbf{w}\cos\beta + \mathbf{w}_1 \sin\beta\cos\psi + \mathbf{w}_2 \sin\beta\sin\psi, \tag{2.19}$$

where β is the deflection angle computed in §2.4. The new velocities of the two stars after the interaction are then given by

$$\mathbf{v}^\star = \mathbf{v} - \frac{m'}{m+m'}(\mathbf{w}^\star - \mathbf{w}), \tag{2.20}$$

$$\mathbf{v}'^\star = \mathbf{v}' + \frac{m}{m+m'}(\mathbf{w}^\star - \mathbf{w}). \tag{2.21}$$

The new radial and transverse velocities for the first star are given by $v_r^\star = v_z^\star$, and $v_t^\star = (v_x^{\star 2} + v_y^{\star 2})^{1/2}$, from which we compute the new orbital energy E and angular momentum J as $E^\star = \Phi(r) + \frac{1}{2}(v_r^{\star 2} + v_t^{\star 2})$, and $J^\star = r v_t^\star$. Similar quantities $E'^\star$ and $J'^\star$ are also computed for the second star.

2.6 Computing New Positions and Velocities

Once the orbits of all the stars are perturbed, i.e., new values of E and J are computed for each star, a new realization of the system is generated, by selecting a new position for each star in its new orbit, in such a way that each position in the orbit is weighted by the amount of time that the star spends at that position. To do this, we begin by computing the pericenter and apocenter distances, r_{min} and r_{max}, for each star. The orbit of a star in the cluster potential is a rosette, with r oscillating between r_{min} and r_{max}, which are roots of the equation

$$Q(r) = 2E - 2\Phi(r) - J^2/r^2 = 0. \tag{2.22}$$

See Binney & Tremaine (1987; §3.1) for a general discussion, and see Hénon (1971b; Eqs. [41]-[45]) for a convenient method of solution. The new position r should now

be selected between r_{min} and r_{max}, in such a way that the probability of finding r in an interval dr is equal to the fraction of time spent by the star in the interval during one orbit, i.e.,

$$\frac{dt}{P} = \frac{dr/|v_r|}{\int_{r_{min}}^{r_{max}} dr/|v_r|}, \tag{2.23}$$

where P is the orbital period, and $|v_r|$ is given by

$$|v_r| = [2E - 2\Phi(r) - J^2/r^2]^{1/2} = [Q(r)]^{1/2}. \tag{2.24}$$

Thus the value of r should be selected from a probability distribution that is proportional to $f(r) = 1/|v_r|$. Unfortunately, at the pericenter and apocenter points (r_{min} and r_{max}), the radial velocity v_r is zero, and the probability distribution becomes infinite. To overcome this problem, we make a change of coordinates by defining a suitable function $r = r(s)$ and selecting a value of s from the distribution

$$g(s) \equiv \frac{1}{|v_r|}\frac{dr}{ds}. \tag{2.25}$$

We must select the function $r(s)$ such that $g(s)$ remains finite in the entire interval. A convenient function $r(s)$ that satisfies these requirements is given by

$$r = \frac{1}{2}(r_{min} + r_{max}) + \frac{1}{4}(r_{max} - r_{min})(3s - s^3), \tag{2.26}$$

where s lies in the interval -1 to 1. We then generate a value for s, which is consistent with the distribution $g(s)$, using the von Neumann rejection technique. Equation (26) then gives a corresponding value for r which is consistent with the distribution function $f(r)$.

The magnitude of the new radial velocity v_r is computed using equation (2.24), and its sign is selected randomly. The transverse velocity is given by $v_t = J/r$.

Once a new position is selected for each star using the above procedure, the gravitational potential $\Phi(r)$ is recomputed as described in §2.3. This completes the

timestep, and allows the next timestep to be started.

Note that the gravitational potential used to compute new positions and velocities of the stars is from the previous timestep. The new potential can only be computed *after* the new positions are assigned, and it is then used to recompute the positions in the next timestep. Thus the computed potential always lags slightly behind the actual potential of the system. The exact potential is known only at the initial condition. This only introduces a small systematic error in the computation, since the potential changes significantly only on the relaxation timescale.

A more important source of error, especially in computing the new energies of the stars after the potential is recomputed, is the random fluctuation of the potential in the core, which contains relatively few stars, but has a high number density. Since the derivative of the potential is also steepest in the core, a small error in computing a star's position in the core can lead to a large error in computing its energy. As the simulation progresses, this causes a slow but consistent leak in the total system energy. The magnitude of this error (i.e., the amount of energy lost per timestep) depends partly on the number of stars N in the system. For large N, the grid on which the potential is pre-computed (see §2.3) is finer, and the number of stars in the core is larger, which reduces the noise in the potential. The overall error in energy during the course of an entire simulation is typically of order a few percent for $N = 10^5$ stars. In any realistic simulation, the actual energy gain or loss due to real physical processes such as stellar evolution, escape of stars through a tidal boundary, and interactions involving binaries, is at least an order of magnitude greater than this error. Hence we choose not to renormalize the energy of the system, or employ any other method to artificially conserve the energy of the system, which could affect other aspects of the evolution.

Another possible source of error in Monte-Carlo simulations, which was noted by Hénon (1971b) is the "spurious relaxation" effect. This is the tendency for the system to relax because of the potential fluctuations from one timestep to the next, even in the absence of orbital perturbations due to two-body relaxation. However, this effect is significant only for simulations done with very low $N \sim 10^2 - 10^3$. In

test calculations performed with $N \sim 10^4 - 10^5$ and two-body relaxation explicitly turned off (by setting the scattering angle $\beta_e = 0$ in eq. [2.10]), we find no evidence of spurious relaxation. Indeed Hénon (1971b) himself showed that spurious relaxation was not significant in his models for $N \gtrsim 10^3$.

2.7 Escape of Stars and the Effect of a Tidal Boundary

For an isolated system, the gradual evaporation of stars from the cluster is computed in the following way. During each timestep, after the perturbations ΔE and ΔJ are computed, all stars with a positive total energy (given by eq. [2.1]) are assumed to leave the cluster on the crossing timescale. They are therefore considered lost immediately on the relaxation timescale, and removed from the simulation. The mass of the cluster (and its total energy) decreases gradually as a result of this evaporation process.

As a simple first step to take in to account the tidal field of the Galaxy, we include an effective tidal boundary around the cluster, at a distance $r_t \simeq R_g(M_{cluster}/3M_g)^{1/3}$, where R_g is the distance of the cluster from the Galactic center and M_g is the mass of the Galaxy (approximated as a point mass). The tidal radius is roughly the size of the Roche lobe of the cluster in the field of the Galaxy. Once the initial tidal radius r_{t0} is specified, the tidal radius at a subsequent time t during the simulation can be computed by $r_t(t) = r_{t0}(M_{cluster}(t)/M_{cluster}(0))^{1/3}$. After each timestep, we remove all stars with an apocenter distance r_{max} greater than the tidal radius, since they are lost from the cluster on the crossing timescale. As the cluster loses stars due to evaporation and the presence of the tidal boundary, its mass decreases, which causes the tidal boundary to shrink, in turn causing even more stars to be lost. The total mass loss due to a tidal boundary can be very significant, causing up to 90% of the mass to be lost (depending on the initial model) over the course of the simulation (see §3.2).

2.8 Units

Following the convention of most previous studies, we define dynamical units so that $[G] = [M_0] = [-4E_0] = 1$, where M_0 and E_0 are the initial total mass and total energy of the system (Hénon 1971). Then the units of length L, and time T are given by

$$L = GM_0^2(-4E_0)^{-1}, \qquad \text{and} \qquad T = GM_0^{5/2}(-4E_0)^{-3/2}. \tag{2.27}$$

We see that L is basically the virial radius of the cluster, and T is of the order of the initial dynamical (crossing) time. To compute the evolution of the cluster on a relaxation timescale, we rescale the unit of time to $TN_0/\ln(\gamma N_0)$, which is of the order of the initial relaxation time. Using this unit of time allows us to eliminate the $\ln(\gamma N)$ dependence of the evolution equations. The only equation that explicitly contains the evolution time is equation (2.10), which relates the timestep and the effective deflection angle. In our units, equation (2.10) can be written as,

$$\left[\sin^2(\beta_e/2)\right] = 2\pi\frac{([m_1] + [m_2])^2}{[w]^3}[\nu][\Delta t]N, \tag{2.28}$$

where [q] indicates a quantity q expressed in our simulation units. Using a unit of time that is proportional to the initial relaxation time has the advantage that the evolution timescale is roughly independent of the number of stars N once an initial model has been selected. This is only true approximately, for isolated systems of equal-mass stars, with no other processes that depend explicitly on the number of stars (such as stellar evolution or mass segregation). For example, the half-mass relaxation time for the Plummer model,

$$t_{rh} = \frac{0.138N}{\ln(\gamma N)}\left(\frac{r_h^3}{GM}\right)^{1/2}, \tag{2.29}$$

is always 0.093 in our units, independent of N.

The dynamical units defined above are identical to the standard N-body units (Heggie & Mathieu 1986). Hence to convert the evolution time from N-body time

units to our Monte-Carlo units, we must simply multiply by a factor $\ln(\gamma N_0)/N_0$.

2.9 Numerical Implementation

We have implemented our Monte-Carlo code on the SGI/CRAY Origin2000 parallel supercomputer at the National Center for Supercomputing Applications (NCSA), and at Boston University. Our parallelized code can be used to get significant speedup of the simulations, using up to 8 processors, especially for large N simulations. This ability to perform large N simulations will be particularly useful for doing realistic simulations of very large globular clusters such as 47 Tuc (with $N \gtrsim 10^6$ stars). A simulation with $N = 10^5$ stars can be completed in approximately 15–20 CPU hours on the Origin2000, which uses MIPS R10000 processors. For comparison, a simulation of this size would take $\sim$ 6 months to complete using the GRAPE-4, which is the fastest available hardware for N-body methods.

The most computationally intensive step in the simulation is the calculation of the new positions of stars. The operation involves solving for the roots of an equation (eq. [2.22]) using the indexed values of the positions of the N stars. We find that the most efficient method to solve for the roots in this case is the simple bisection method (e.g., Press et al. 1992), which requires $\sim N \log_2 N$ steps to converge to the root. Hence the computation of the positions and velocities also scales as $\sim N \log_2 N$ in our method. The next most expensive operation is the evaluation of the potential at a given point r. As described in §2.3, this requires finding k such that $r_k \leq r \leq r_{k+1}$ and then using equation (2.4). This search can again be done easily using the bisection algorithm. However, since the evaluation of the potential is required several times for each star, in each timestep, it is useful to tabulate the values of k on fine grid in r at the beginning of the timestep. This allows the required values of k to be found very quickly, at the minor cost of using more memory to store the table. The rest of the steps in the simulation scale almost linearly with N. This makes the overall computation time scale (theoretically) as $N \log_2 N$.

In Figure 2-1, we show the scaling of the wall-clock time with the number of pro-

cessors, and also the scaling of the overall computation time with the number of stars N in the simulation. The overall computation time is consistent with the theoretical estimate for $N \lesssim 10^5$. For larger N, the computation time is significantly higher, because of the less efficient use of cache memory and other hardware inefficiencies that are introduced while handling large arrays. For N in the range $1 - 5 \times 10^5$, we find that the actual computation time scales as $\sim N^{1.4}$.

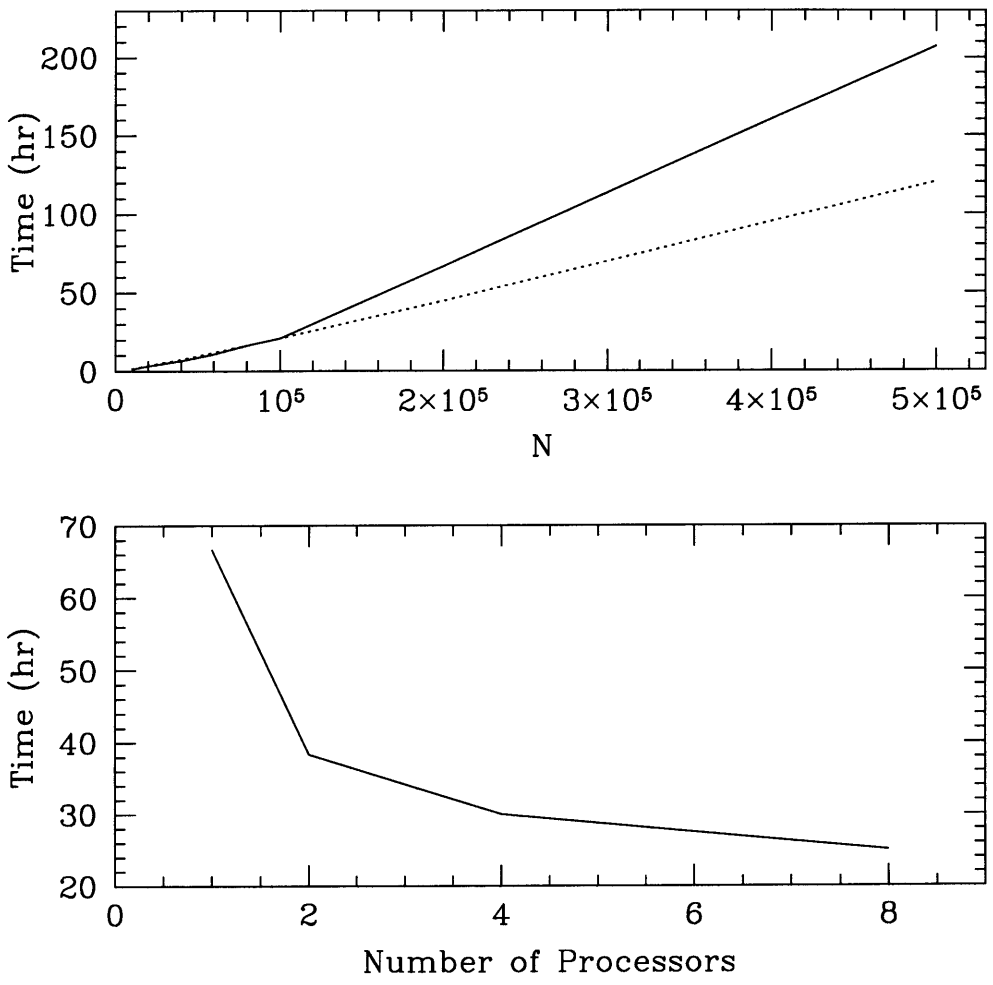

Figure 2-1: The top frame shows the total computation time required (for an initial Plummer model evolved up to core collapse) using one processor for simulations with up to $N = 5 \times 10^5$. The dotted line indicates the theoretically estimated scaling of the computation time as $\sim N \log_2 N$. In practice, we find that the computation time scales as $\sim N^{1.4}$ for $N = 1 - 5 \times 10^5$. The bottom frame shows the scaling of the computation time ("wall-clock time") with the number of processors for $N = 2 \times 10^5$.

We find that we can easily reduce the overall computation time by a factor of ≈ 3 by using up to 8 processors. The scaling is most efficient for $2-4$ processors for simulations with $N \sim 1-5\times 10^5$. The scaling gets progressively worse for more than 8 processors. This is in part caused by the distributed shared-memory architecture of the Origin2000 supercomputer, which allows very fast communication between the nearest 2-4 processors, but slower communication between the nearest 8 processors. Beyond 8 processors, the communication is even slower, since the processors are located on different nodes. The most suitable architecture for implementing the parallel Monte-Carlo code would be a truly shared memory supercomputer, with roughly uniform memory access times between processors. Our code is implemented using the Message Passing Interface (MPI) parallelization library, which is actively being developed and improved. The MPI standard is highly portable, and available on practically all parallel computing platforms in use today. The MPI library is optimized for each platform and automatically takes advantage of the memory architecture to the maximum extent possible. Hence we expect that future improvements in the communication speed and memory architectures will make our code scale even better. We are also in the process of improving the scaling of the code to a larger number of processors by designing a new algorithm for reducing the amount of communication required between processors.

Chapter 3

Evolution of Clusters with Equal-Mass Stars

[1]

In this chapter, we describe our first results using the new Monte-Carlo code to compute the evolution of the Plummer and King models. We explore the evolution of the Plummer model in detail, and compare our results with those obtained using Fokker-Planck and N-body methods. We also compare core-collapse times and mass-loss rates for the series of King models (with dimensionless central potential $W_0 = 1-12$), including a tidal radius, with similar results obtained by Quinlan (1996) using a 1-D Fokker-Planck method.

3.1 Evolution of an Isolated Plummer Model

We first consider the evolution of a cluster with the Plummer model (which is a polytropic model, with index $n = 5$; see, e.g., Binney & Tremaine 1987) as the initial condition. Perhaps the best known result for single component systems, is the expected homologous evolution of the halo, leading to the eventual development of a power-law density profile between the core and the outer halo, during the late phases

[1] Based on the results in Joshi, Rasio & Portegies Zwart 2000

of evolution. At late times the cluster evolves through a sequence of nearly self-similar configurations, with the core contracting and a power-law halo with density $\rho \propto r^{-\beta}$ expanding out. The development of this power law has been predicted theoretically (Lynden-Bell & Eggleton 1980; Heggie & Stevenson 1988), and verified using direct Fokker-Planck integrations (Cohn 1980). The exponent β is theoretically and numerically estimated to be about 2.2 (Spitzer 1987). However, since the theoretical derivations are based on an analysis of the Fokker-Planck equation, it is not surprising that the numerical Fokker-Planck integrations (which solve the same Fokker-Planck equation numerically) reproduce the theoretical exponent exactly. Due to limitations in computing accurate density profiles using a small number of stars, this result has not been confirmed independently using an N-body simulation.

Here, we explore numerically for the first time the development of this power law using an independent method. Some early results were obtained using previous versions of the Monte-Carlo method, but with a small number of stars $N \sim 10^3$ (Duncan & Shapiro 1982). Although the Monte-Carlo method can be thought of as just another way of solving the Fokker-Planck equation, there are significant differences between solving the equation in the continuous limit ($N \to \infty$), as in direct Fokker-Planck integrations, and by using a discrete system with a finite N as in our method. There are also many subtle differences in the assumptions and approximations made in the two methods, and even in different implementations of the same method.

In Figures 3-1a–c we show the density profile of the cluster at three different times during its evolution, up to core collapse. We start with an $N = 10^5$ isolated Plummer model, and follow the evolution up to core-collapse, which occurs at $t = t_{cc} \simeq 15.2\, t_{rh}$. This simulation, performed with $N = 10^5$ stars, took about 18 CPU hours on the SGI/Cray Origin2000. In our calculations, the core-collapse time is taken as the time when the the innermost Lagrange radius (radius containing 0.3% of the total mass of the cluster) becomes smaller than 0.001 (in our units described in §2.8), at which point the simulation is terminated. Given the very rapid evolution of the core near core collapse, we find that we can determine the core-collapse time to within $\lesssim 1\%$. The accuracy is limited mainly by noise in the core. The value we obtain for t_{cc}/t_{rh}

is in very good agreement with other core-collapse times between $15 - 16\,t_{rh}$ for the Plummer model, reported using other methods. For example Quinlan (1996) obtains a core collapse time of $15.4\,t_{rh}$ for the Plummer model using a 1-D Fokker-Planck method, and Takahashi (1993) finds a value of $15.6\,t_{rh}$, using a variational method to solve the 1-D Fokker-Planck equation.

Figure 3-1a shows the density profile at an intermediate time $t = 11.4\,t_{rh}$ during the evolution. The dotted line indicates the initial Plummer profile. At this point in the evolution, we still see a well defined core, with the core density increased by a factor of ~ 30 compared to the initial core density. We see the power-law density profile developing, with the best-fit index $\beta = 2.8$. In Figure 3-1b, we show the density profile just before core collapse, at $t = 15\,t_{rh}$. We see that the core density has now increased by a factor of $\sim 10^4$ over the initial core density. The power law is now clearly visible, with the best-fit index $\beta = 2.3$. Finally, in Figure 3-1c, we show the density profile at core-collapse, $t = 15.2\,t_{rh}$. The dashed line now indicates the *theoretical* power law with $\beta = 2.2$. We see that the actual density profile seems to approach the theoretical profile asymptotically as the system approaches core collapse. At this point in the evolution, the core density as measured in our simulation is about 10^6 times greater than the initial density. In a globular cluster with $N = 2 \times 10^5$, an average stellar mass $< m >= 0.5\,\mathrm{M}_\odot$, and a mean velocity dispersion $< v^2 >^{1/2}= 5\,\mathrm{km\,s^{-1}}$, this would correspond to a number density of $\sim 2 \times 10^9\,\mathrm{pc}^{-3}$. Note that a real globular cluster is not expected to reach such high core densities, since the formation of binaries and the subsequent heating of the core due to binary interactions become significant at much lower densities. Numerical noise due to the extremely small size of the core makes it difficult to determine the core radius and density accurately at this stage. This also causes the numerical accuracy of the Monte-Carlo method to deteriorate, forcing us to stop the computation. Thus, we find that the power-law structure of the density profile as the cluster approaches core collapse is consistent with theoretical predictions, and the power-law index approaches its theoretical value asymptotically during the late stages of core collapse.

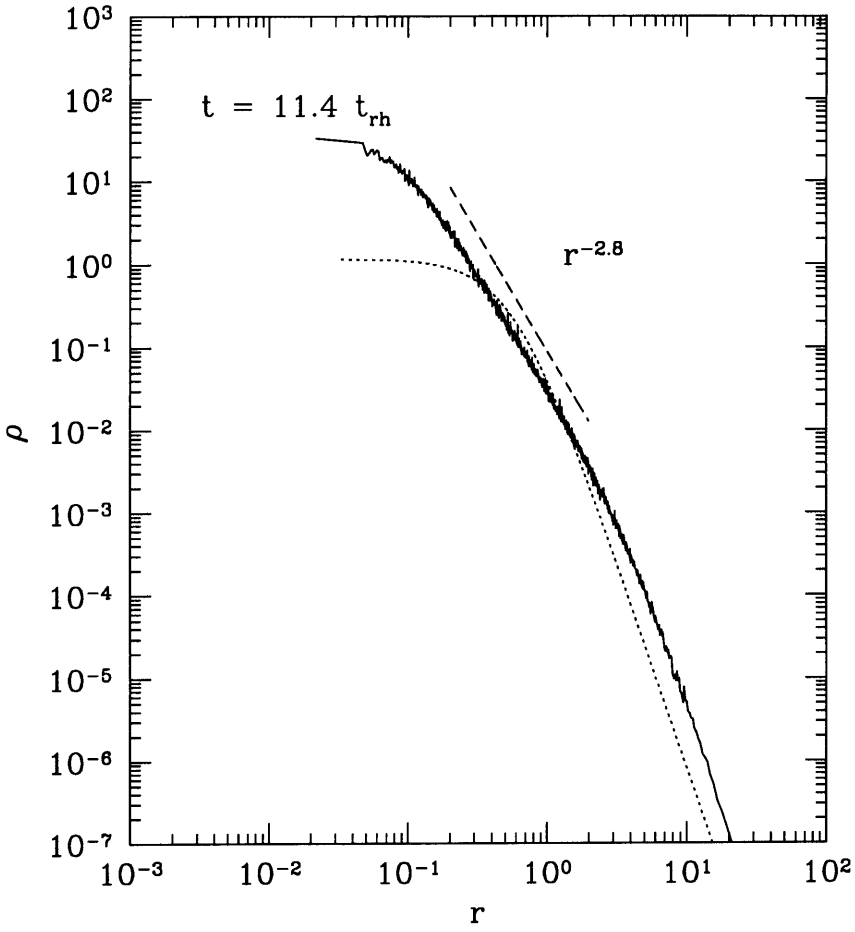

Figure 3-1: (a) Density profile at an intermediate time, $t = 11.4\, t_{rh}$ during the evolution of an isolated Plummer model with $N = 10^5$ stars. The expected power-law in the density profile is clearly seen, with the best-fit exponent $\beta = 2.8$. The power law exponent approaches its theoretical value of 2.2 as the cluster approaches core-collapse (cf. Fig. 3-1b & c). The dotted line indicates the initial Plummer profile. Units are defined in §2.8.

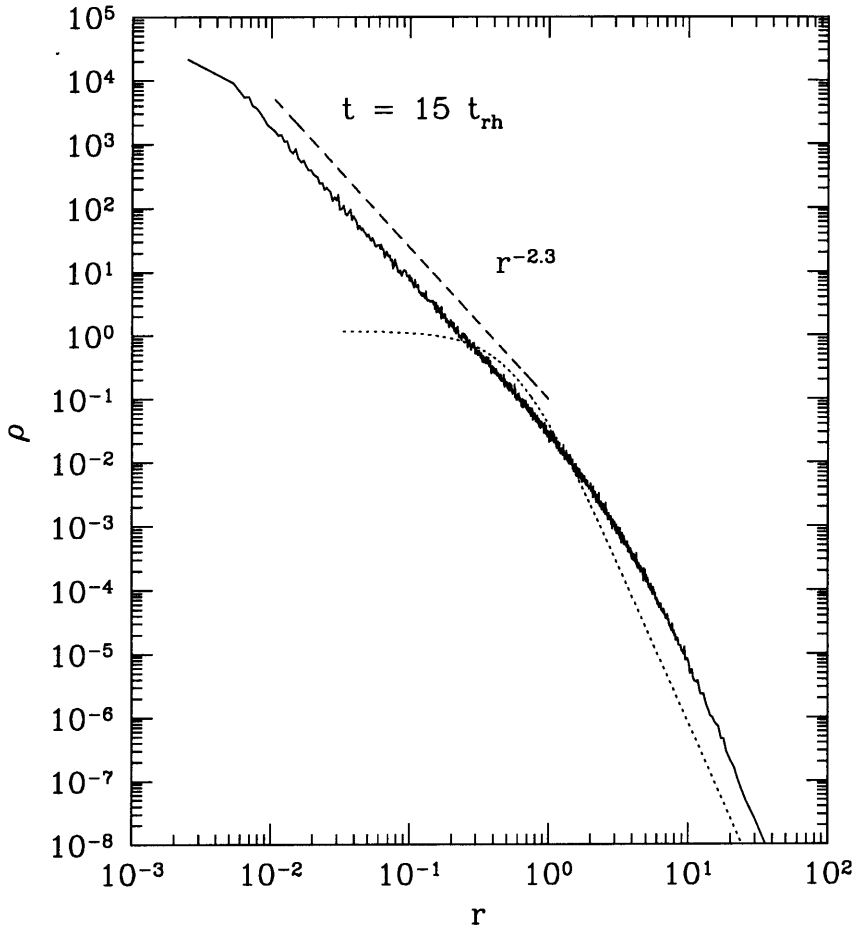

Figure 3-1: (b) Density profile at $t = 15\, t_{rh}$ (just before core-collapse) for the same model as in Fig. 3-1 a. The expected power-law in the density profile is now clearly seen, with the best-fit exponent $\beta = 2.3$, which is now closer to its theoretical value of 2.2. The core density is about 10^4 times greater than the initial density.

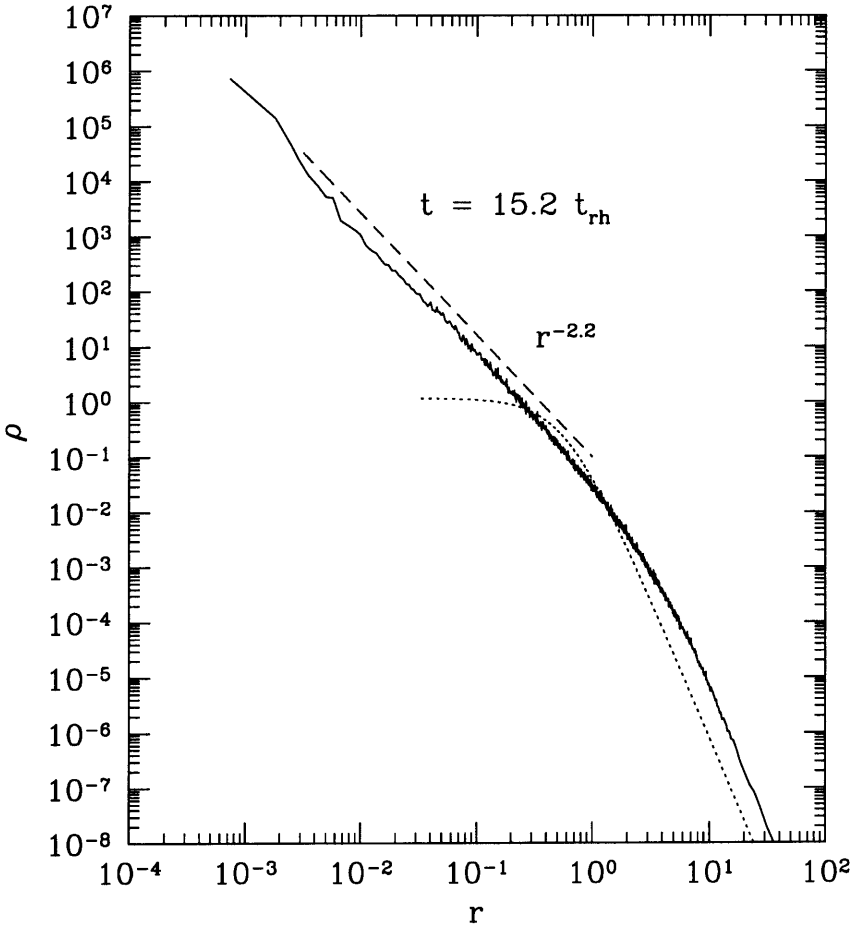

Figure 3-1: (c) Density profile at $t_{cc} = 15.2\, t_{rh}$ (at core-collapse) for the same model as in Fig. 3-1 a. The dashed line now indicates the *theoretical* power law, with exponent $\beta = 2.2$. The core density is almost 10^6 times greater than the initial density.

Next, we look at the evolution of the Lagrange radii (radii containing constant fractions of the total mass), and we compare our results with those of an equivalent N-body simulation. In Figure 3-2, we show the evolution of the Lagrange radii for an $N = 16384$ direct N-body integration by Makino (1996) and for our Monte-Carlo integration with $N = 10^5$ stars. Time in the direct N-body integration is scaled to the initial relaxation time (the standard time unit in our Monte Carlo method) using equation (27) with $\gamma = 0.11$ (see Heggie & Mathieu 1986; Giersz & Heggie 1994; Makino 1996). The agreement between the N-body and Monte Carlo results is excellent over the entire range of Lagrange radii and time. The small discrepancy in the outer Lagrange radii is caused in part by a different treatment of escaping stars in the two models. In the Monte Carlo model, escaping stars are removed from the simulation and therefore not included in the determination of the Lagrange radii, whereas in the N-body model escaping stars are not removed. The difference is further explained by the effect of strong encounters, which is greater in the N-body simulation by a factor $\sim \ln(10^5)/\ln(16384)$, or about 20%. In an isolated cluster, the overall evaporation rate is very low (less than 1% of stars escape up to core collapse). In this regime, the escape of stars is dominated by strong interactions in the core. Since the orbit-averaged Fokker-Planck equation is only valid when the fractional energy change per orbit is small, it does not account for strong interactions. Hence, our Monte-Carlo simulations cannot accurately predict the rate of evaporation from an isolated cluster (see, e.g., Binney & Tremaine 1987, §8.4). This problem does not occur in tidally truncated clusters, where the escape rate is much higher, and is dominated by the diffusion of stars across the tidal boundary, and not by strong interactions.

In Figure 3-3 we show the evolution of various global quantities for the system during the same simulation as in Figure 3-2. The virial ratio ($K/|W|$, where K and W are the total kinetic and potential energies of the cluster) remains very close to 0.5 (within 1%), indicating that dynamical equilibrium is maintained very well during the entire simulation. The virial ratio provides a very good measure of the quality of our numerical results, since it is not controlled in our calculations (except for the

initial model, which is constructed to be in equilibrium). We see that in the absence of a tidal radius, there is very little mass loss (less than 1%), and hence very little energy is carried away by escaping stars.

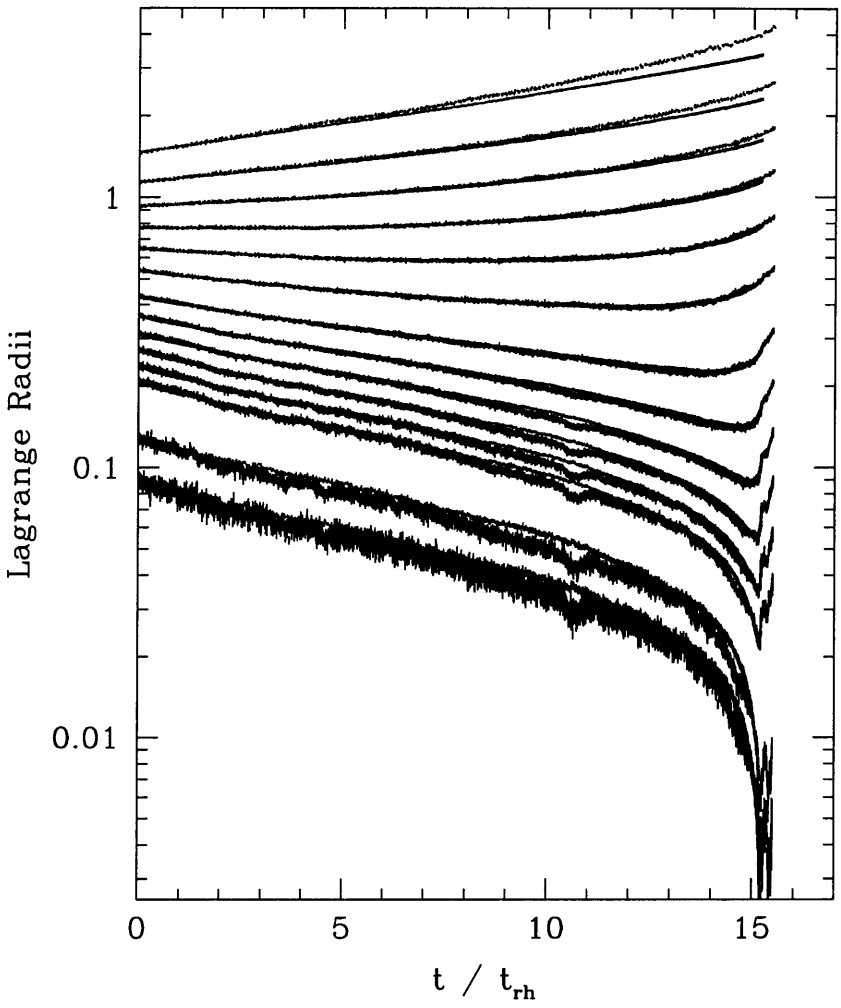

Figure 3-2: Lagrange radii indicating the evolution of the Plummer model, with $N = 10^5$ stars, compared with an N-body simulation with $N = 16384$ stars. Lagrange radii shown correspond to radii containing 0.35, 1, 3.5, 5, 7, 10, 14, 20, 30, 40, 50, 60, 70, and 80 percent of the total mass. The Monte-Carlo simulation is terminated at core-collapse, while the N-body simulation continues beyond core-collapse.

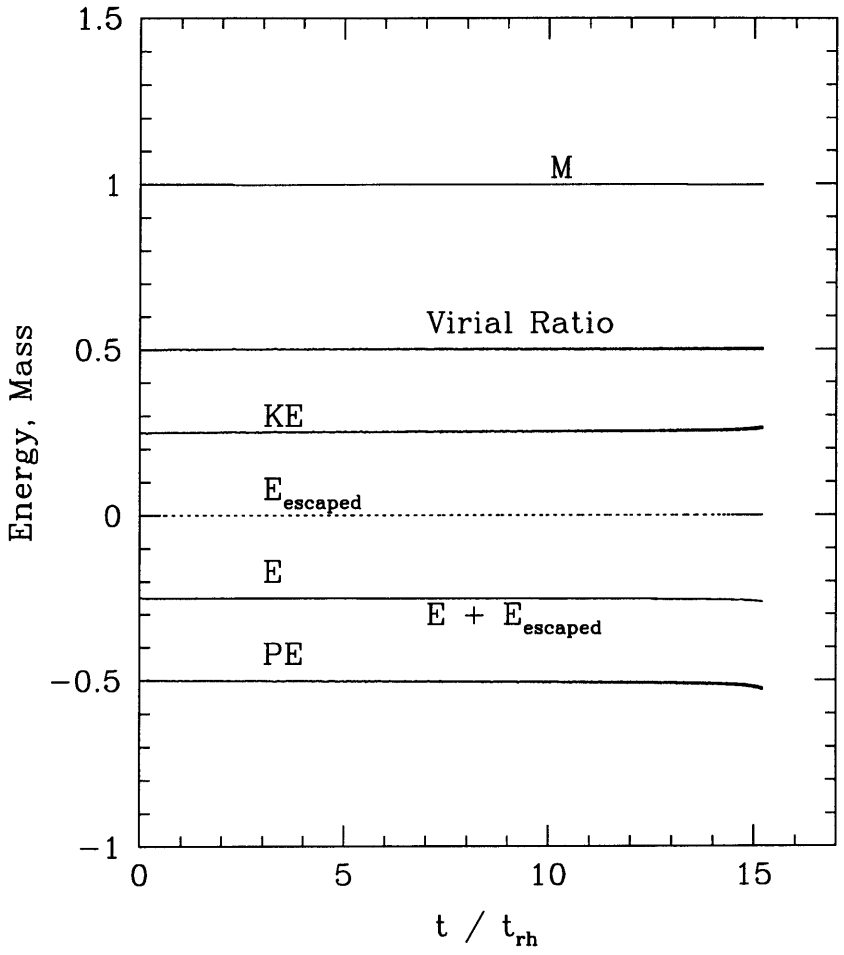

Figure 3-3: The evolution of the total mass and energies for the same Plummer model as in Fig. 3-2. The total mass loss at the time of core-collapse is 0.3%, and the total energy loss is about 4%. Most of the energy is lost during the late stages of evolution, with the energy loss up to $t = 10\,t_{rh}$ being less than 1%. Here the energy carried away by escaping stars ($E_{escaped}$) is negligible.

3.2 Evolution of Isolated and Tidally Truncated King models

King models (King 1966) have long been used to fit observed profiles of globular clusters. They usually provide a very good fit for most clusters, except for those which have reached core collapse. A King model has a well-defined, nearly constant-density core, and a "lowered Maxwellian" velocity distribution, which represents the presence of a finite tidal radius. A King model is usually specified in terms of the dimensionless central potential W_0 or, equivalently, the central concentration $c = \log(r_t/r_c)$, where r_t is the tidal radius, and r_c is the core radius.

We study the evolution of the entire family of King models from $W_0 = 1$ to $W_0 = 12$, in two different configurations. We first consider the evolution of an isolated cluster i.e., even though the initial King model is truncated at its finite tidal radius, we do not enforce that tidal boundary during the evolution, allowing the cluster to expand indefinitely. We compute the core-collapse times for the entire sequence of King models. We then redo the calculations with a tidal boundary in place, to determine the enhanced rate of mass loss from the cluster and the final remaining mass at the time of core collapse. We compare our results for the sequence of King models with equivalent results obtained by Quinlan (1996) using direct Fokker-Planck integrations in 1-D. In Table 3.1, we show the core collapse times for the various models, along with the equivalent results from Quinlan (1996). All our Monte-Carlo calculations were performed using $N = 10^5$ stars. We see that the agreement in the core collapse times for isolated clusters is excellent (within a few percent for the low-W_0 models, and within 10% up to $W_0 = 9$). For $W_0 > 9$, the agreement is still good, considering that the models start off in a highly collapsed state and therefore have very short core-collapse times, which leads to larger fractional errors.

In Figure 3-4, we show the evolution of the Lagrange radii for a tidally truncated King model with $W_0 = 3$. The initial tidal radius is $\simeq 3.1$ times the virial radius. In this case, the mass loss through the tidal boundary is very significant, as is seen from the evolution of the outer Lagrange radii. The mass loss causes the tidal radius to

	Isolated		Tidally Truncated			
W_0	t_{cc}/t_{rh}	t_{cc}/t_{rh} (Quinlan)	t_{cc}/t_{rh}	t_{cc}/t_{rh} (Quinlan)	M_{final}	M_{final} (Quinlan)
1	18.1	17.89	10.0	5.98	0.30	0.10
2	17.9	17.85	10.8	7.74	0.37	0.17
3	17.7	17.61	12.0	9.49	0.44	0.24
4	17.3	17.24	12.9	11.26	0.53	0.33
5	15.9	16.37	13.3	12.73	0.64	0.44
6	13.9	14.49	12.4	12.94	0.76	0.57
7	10.6	10.84	9.30	10.50	0.86	0.72
8	5.32	5.79	5.21	5.76	0.88	0.85
9	2.10	2.25	2.01	2.25	0.96	0.92
10	0.86	0.93	0.80	0.93	0.97	0.96
11	0.41	0.47	0.40	0.47	0.99	0.98
12	0.20	0.26	0.20	0.26	0.99	0.99

Table 3.1: Core-collapse times for the sequence of isolated and tidally truncated King models, computed using $N = 10^5$ stars. Comparison is made with similar results obtained by Quinlan (1996) using a 1-D Fokker-Planck method.

constantly move inward, which further accelerates the process. Figure 3-5 shows the evolution of the total mass and energy of the tidally truncated cluster. Only 44% of the initial mass is retained in the cluster at core-collapse. Also, the binding energy of the cluster is significantly lower at core-collapse, since the escaping stars carry away mass as well as kinetic energy from the cluster. In contrast, the evolution of an isolated $W_0 = 3$ King model is very much like that of the isolated Plummer model described earlier, with a very low mass loss rate, and a longer core-collapse time of $t_{cc} = 17.7\, t_{rh}$ (in excellent agreement with the value of $17.6\, t_{rh}$ computed by Quinlan 1996).

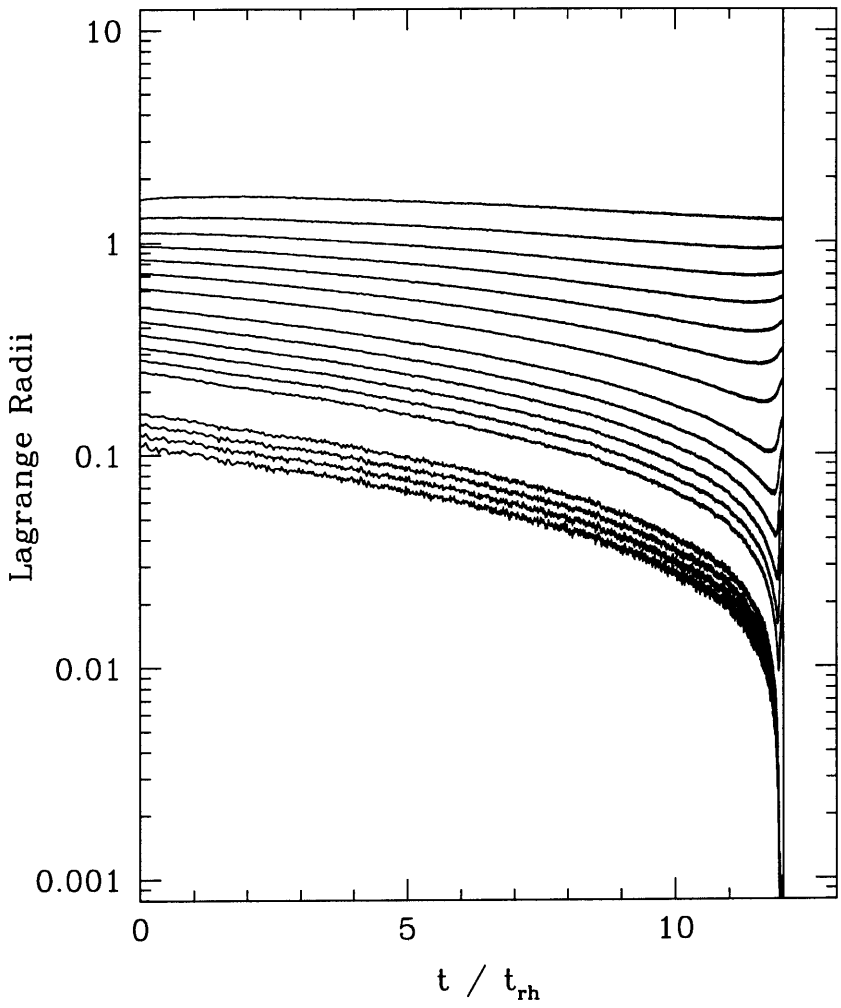

Figure 3-4: Lagrange radii for the evolution of a *tidally truncated* King model with $W_0 = 3$. The tidal boundary causes stars to be lost at a much higher rate compared to the isolated model. The vertical line indicates the core-collapse time $t_{cc} = 12.0\, t_{rh}$. The presence of the tidal boundary reduces the core-collapse time by about 32% compared to the isolated model. In contrast, the evolution of an *isolated* $W_0 = 3$ King model is very much like that of the Plummer model shown in Fig. 3-2, with a total mass loss $< 1\%$, and $t_{cc} = 17.7\, t_{rh}$.

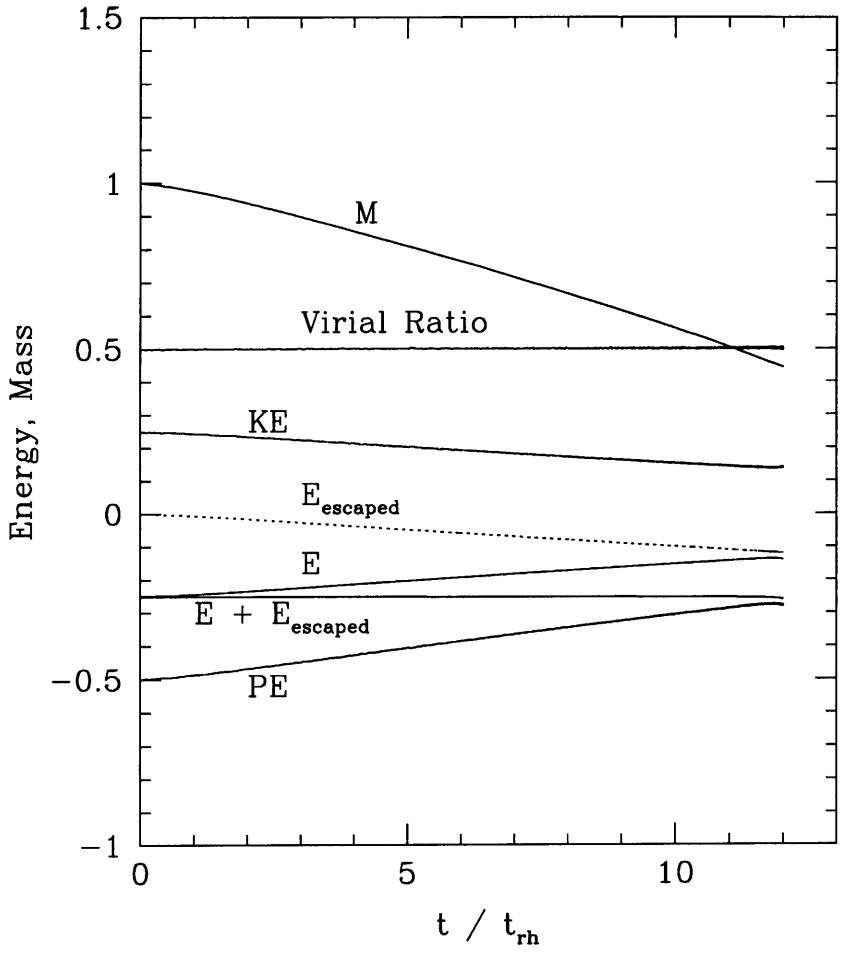

Figure 3-5: The evolution of the total mass and energies for the model shown in Fig. 3-4. Only 44% of the initial mass remains in the cluster at core collapse. The dotted line indicates the energy carried away by escaping stars. The large mass loss due to the tidal boundary causes the overall binding energy of the cluster to decrease significantly.

Our results for clusters with a tidal boundary show systematic differences from the 1-D Fokker-Planck results of Quinlan (1996). We find that the mass loss through the tidal boundary is significantly higher for the low-concentration models ($W_0 < 6$) in the Fokker-Planck models. For the high-concentration ($W_0 > 6$) models, the difference between isolated models and tidally truncated models is small, and the agreement between the methods remains very good. Hence, for low W_0, our models undergo core collapse at a much later time compared to the Fokker-Planck models, and retain more mass at core collapse. This discrepancy is caused by the 1-D nature of the Fokker-Planck models. In 1-D Fokker-Planck calculations, stars are considered lost from the cluster when their energy is greater than the energy at the tidal radius. This clearly provides an overestimate of the escape rate, since it assumes the most extended radial orbits for stars, and ignores stars on more circular orbits with high angular momentum, which would have much smaller orbits at the same energy. In contrast, in the Monte-Carlo method, the orbit of each star is computed using its energy *and* angular momentum, which allows the apocenter distance to be determined correctly. Stars are considered lost only if their apocenter distances from the cluster center are greater than the tidal radius. As stars on radial orbits are removed preferentially, this creates an anisotropy within the cluster, which affects the overall evolution. The artificially high rate of mass loss in 1-D Fokker-Planck simulations has also been pointed out recently in comparisons with N-body results (Portegies Zwart et al. 1998; Takahashi & Portegies Zwart 1999). These authors show that, with appropriate modifications, the results of 2-D Fokker-Planck calculations can be made to agree much better with those from N-body simulations. Indeed, we find that our result for the $W_0 = 3$ model with a tidal boundary ($t_{cc} = 12.0\, t_{rh}$, and $M_{final} = 0.44$) agrees much better with that obtained using the improved 2-D Fokker-Planck method, which gives $t_{cc} = 11.3\, t_{rh}$, and $M_{final} = 0.34$ (Takahashi 1999, private communication). For further comparison, and to better understand the cause of the higher mass loss in the 1-D Fokker-Planck calculation, we have performed a Monte-Carlo simulation using the same energy-based escape criterion that is used in the 1-D Fokker-Planck integrations. We find that using the energy-based escape criterion for $W_0 = 3$ gives

$t_{cc} = 10.9\,t_{rh}$, and $M_{final} = 0.30$, which agrees better with the 1-D Fokker-Planck result, but a significant discrepancy still remains. This is not surprising, since, even when using a 1-D escape criterion, our underlying method still remains 2-D. Again, our result agrees better with the corresponding result obtained by Takahashi (1999, private communication) using the energy-based escape criterion in his 2-D Fokker-Planck method, $t_{cc} = 10.2\,t_{rh}$, and $M_{final} = 0.28$. It is reassuring to note that the differences between our 2-D results and 1-D Fokker-Planck results are also mirrored in the 2-D Fokker-Planck calculations of Takahashi. Since our Monte-Carlo method is intrinsically 2-D, it is not possible for us to do a true 1-D (isotropic) calculation to compare results directly with 1-D Fokker-Planck calculations.

3.3 Summary

We have presented results obtained using our new Monte-Carlo code for the evolution of clusters containing 10^5 stars, up to core collapse. We have compared our results with those of 1-D Fokker-Planck calculations (Quinlan 1996) for isolated as well as tidally truncated King models with $W_0 = 1-12$. We find very good agreement for the core-collapse times of isolated King models. For tidally truncated models (especially for $W_0 < 6$), we find that the escape rate of stars in our models is significantly lower than in the 1-D Fokker-Planck models. This is to be expected, since the 1-D Fokker-Planck models use an energy-based escape criterion, which does not account for the anisotropy in the orbits of stars, and hence overestimate the escape rate. This effect is most evident in tidally truncated clusters, since stars on radial orbits are preferentially removed, while those on more circular orbits (with the same energy) are not. In one case ($W_0 = 3$), we have verified that our results are in good agreement with those from new 2-D Fokker-Planck calculations (Takahashi 1999, private communication), which properly account for the velocity anisotropy, and use the same apocenter-based escape criterion as in our models. Further comparisons of our results with 2-D Fokker-Planck calculations are presented in the next chapter. Our detailed comparison of the evolution of the Plummer model with an equivalent direct N-body simulation also

shows excellent agreement between the two methods up to core collapse.

Our results clearly show that the Monte-Carlo method provides a robust, scalable and flexible alternative for studying the evolution of globular clusters. Its strengths are complementary to those of other methods, especially N-body simulations, which are still prohibitively expensive for studying large systems with $N \gtrsim 10^5$. The Monte-Carlo method requires more computational resources compared to Fokker-Planck methods, but it is several orders of magnitude faster than N-body simulations. The star-by-star representation of the system in this method makes it particularly well suited for studying the evolution of interesting sub-populations of stars within globular clusters, such as pulsars, blue stragglers, or black holes.

Our method also presents the interesting possibility of performing hybrid simulations that use the Monte-Carlo method for the bulk of the evolution of a cluster up to the core collapse phase, and then switch to an N-body simulation to follow the complex core-collapse phase during which the high reliability of the N-body method is desirable. The discreteness of the Monte-Carlo method, and the fact that it follows the same phase space parameters for a cluster as the N-body method, make it easy to switch from one method to the other during a single simulation.

Chapter 4

Mass Spectra, Stellar Evolution and Cluster Lifetimes in the Galaxy

[1]

4.1 Introduction

The evolution of globular clusters in the Galactic environment has been studied using a variety of theoretical and numerical techniques. The first comprehensive study of cluster lifetimes was conducted by Chernoff & Weinberg (1990, hereafter CW) using F-P simulations. They included the effects of a power-law mass spectrum, a tidal cut-off radius imposed by the tidal field of the Galaxy, and mass loss due to stellar evolution. Their results were surprising, and far reaching, since they showed for the first time that the majority of clusters with a wide range of initial conditions would be disrupted in $\lesssim 10^{10}$ yr, and would not survive until core collapse. CW carried out their calculations using a 1-D F-P method, in which the stellar distribution function in phase space is assumed to depend on the orbital energy only. However, more

[1] Based on the results in Joshi, Nave & Rasio 2000

recently, similar calculations undertaken using direct N-body simulations gave cluster lifetimes up to an order of magnitude longer compared to those computed by CW (Fukushige & Heggie 1995; Portegies Zwart et al. 1998). The discrepancy appears to be caused by an overestimated mass loss rate in the 1-D F-P formulation (Takahashi & Portegies Zwart 1998), which does not properly account for the velocity anisotropy in the cluster. To overcome this problem, new 2-D versions of the F-P method (in which the distribution function depends on both energy and angular momentum) have been employed (Takahashi 1995, 1996, 1997; Drukier et al. 1999).

The 2-D F-P models provide cluster lifetimes in significantly better agreement with direct N-body integrations (Takahashi & Portegies Zwart 1998). However, the 2-D F-P models still exhibit a slightly higher mass loss rate compared to N-body simulations. This may result from the representation of the system in terms of a continuous distribution function in the F-P formulation, which effectively models the behavior of the cluster in the $N \rightarrow \infty$ limit. To test this possibility, Takahashi & Portegies Zwart (1998) introduce an additional free parameter $\nu_{\rm esc}$ in their F-P models, attempting to take into account the finite ratio of the crossing time to the relaxation time (see also Lee & Ostriker 1987; Ross et al. 1997). They use this free parameter to lower the overall mass loss rate in their F-P models and obtain agreement with N-body simulations (performed with up to $N = 32,768$). Takahashi & Portegies Zwart (1999, hereafter TPZ) show that, after calibration, a single value of $\nu_{\rm esc}$ gives consistent agreement with N-body simulations for a broad range of initial conditions .

In chapter 3, we presented our results for a series of calculations with isolated and tidally truncated King models. We found excellent agreement between the results of our calculations and those of direct N-body and 1-D Fokker-Planck simulations for a variety of single-component clusters (i.e., containing equal-mass stars). However, we found that, for tidally truncated clusters, the mass loss rate in our models was significantly lower, and the core-collapse times significantly longer, than in corresponding 1-D F-P calculations. We noted that, for a single case (a $W_0 = 3$ King model), our results were in good agreement with those of 2-D F-P calculations by Takahashi

(1999).

In this chapter, we extend our Monte-Carlo calculations to multi-component clusters (described by a continuous, power-law stellar mass function), and we study the evolution of globular clusters with a broad range of initial conditions. Our calculations include an improved treatment of mass loss through the tidal boundary, as well as mass loss due to stellar evolution. Our new method treats the mass loss through the tidal boundary more carefully in part by making the timestep smaller, especially in situations where the tidal mass loss can lead to an instability resulting in rapid disruption of the cluster. We also also account for the shrinking of the tidal boundary in each timestep by iteratively removing stars with apocenter distances greater than the tidal boundary, and recomputing the tidal radius using the new (lower) mass of the cluster. We compare our new results with those of CW and TPZ. We also go beyond these previous studies and explore several other issues relating to the pre-collapse evolution of globular clusters. We study in detail the importance of the velocity anisotropy in determining the stellar escape rate. We also compare the orbital properties of escaping stars in disrupting and collapsing clusters. Finally, we consider the effects of an eccentric orbit in the Galaxy, allowing for the possibility that a cluster may not fill its Roche lobe at all points in its orbit.

The calculations presented in this chapter are for clusters containing single stars only. The dynamical effects of hard primordial binaries for the overall cluster evolution are not significant during most of the the *pre-collapse* phase. Energy generation through binary – single star and binary – binary interactions becomes significant only when the cluster approaches core collapse and interaction rates in the core increase substantially (Hut, McMillan & Romani 1992; Gao et al. 1991; McMillan & Hut 1994). Formation of hard "three-body" binaries can also be neglected until the cluster reaches a deep core-collapse phase. During the pre-collapse evolution, hard binaries behave approximately like single more massive stars, while soft binaries (which have a larger interaction cross section) may be disrupted. Since we do not include the effects of energy generation by primordial binaries in our calculations, the (well-defined) core-collapse times presented here may be re-interpreted as corresponding approxi-

mately to the onset of the "binary-burning" phase, during which a similar cluster containing binaries would be supported in quasi-equilibrium by energy-generating interactions with hard binaries in its core (Spitzer & Mathieu 1980; Goodman & Hut 1989; McMillan, Hut & Makino 1990). Our calculations of disruption times (for clusters that disrupt in the tidal field of the Galaxy before reaching core collapse) are largely independent of the cluster binary content, since the central densities and core interaction rates in these clusters always remain very low.

4.2 Additions to the Monte-Carlo Method

Our code, described in detail in chapter 2, is based on the orbit-averaged Monte-Carlo method. Although in chapter 3 we only presented results of test calculations performed for single-component clusters, the method is completely general, and the implementation of an arbitrary mass spectrum is straightforward. This section describes additional features of our code that were not included in Chapter 2: an improved treatment of mass loss through the tidal boundary (§2.1), and a simple implementation of stellar evolution (§2.2). The construction of initial multi-component King models for our study of cluster lifetimes is described in §3.3. The highly simplified treatments of tidal effects and stellar evolution adopted here are for consistency with previous studies, since one of our objectives in this chapter is also to establish the accuracy of our code by presenting detailed comparisons with the results of other methods.

4.2.1 Tidal Stripping of Stars

In an isolated cluster, the mass loss rate (up to core collapse) is relatively small, since escaping stars must acquire positive energies mostly through rare, strong interactions in the dense cluster core (see the discussion in Chapter 3). In contrast, for a tidally truncated cluster, the mass loss is dominated by diffusion across the tidal boundary (also referred to as "tidal stripping"). In our Monte-Carlo simulations, a star is assumed to be tidally stripped from the cluster (and lost instantaneously) if the

apocenter of its orbit in the cluster is outside the tidal radius. This is in contrast to the *energy-based* escape criterion that is used in 1-D F-P models, where a star is considered lost if its energy is greater than the energy at the tidal radius, regardless of its angular momentum. As noted in Chapter 3, the 2-D treatment is crucial in order to avoid overestimating the escape rate, since stars with high angular momentum, i.e., on more circular orbits, are less likely to be tidally stripped from the cluster than those (with the same energy) on more radial orbits.

A subtle, yet important aspect of the mass loss across the tidal boundary, is the possibility of the tidal stripping process becoming *unstable* if the tidal boundary moves inward too quickly. As the total mass of the cluster decreases through the escape of stars, the tidal radius of the cluster shrinks. This causes even more stars to escape, causing the tidal boundary to shrink further. If at any time during the evolution of the cluster the density gradient at the tidal radius is too large, this can lead to an unstable situation, in which the tidal radius continues to shrink on the dynamical timescale, causing the cluster to disrupt. The development of this instability characterizes the final evolution of all clusters with a low initial central concentration that disrupt in the Galactic tidal field before reaching core collapse.

We test for this instability at each timestep in our simulations, by iteratively removing escaping stars and recomputing the tidal radius with the appropriately lowered cluster mass. For stable models, this iteration converges quickly, giving a finite escape rate. Even before the development of the instability, this iterative procedure must be used for an accurate determination of the mass loss rate. When the mass loss rate due to tidal stripping is high, we also impose a timestep small enough that no more than 1% of the total mass is lost in a single timestep. This is to ensure that the potential is updated frequently enough to take the mass loss into account. This improved treatment of tidal stripping was not used in our calculations for Paper I. However, all the results presented in Paper I were for clusters with equal-mass stars, with no stellar evolution. Under those conditions, all models reach core collapse, with no disruptions. The issue of unstable mass loss is not significant in those cases, and hence the results of Paper I are unaffected.

4.2.2 Stellar Evolution

Our simplified treatment follows those adopted by CW and TPZ. We assume that a star evolves instantaneously to become a compact remnant at the end of its main-sequence lifetime. Indeed, since the evolution of our cluster models takes place on the relaxation timescale (i.e., the timestep is a fraction of the relaxation time $t_r \gtrsim 10^9\,\mathrm{yr}$), while the dominant mass loss phase during late stages of stellar evolution takes place on a much shorter timescale ($\sim 10^6\,\mathrm{yr}$), the mass loss can be considered instantaneous. We neglect mass losses in stellar winds for main-sequence stars. We assume that the main-sequence lifetime and remnant mass is a function of the initial stellar mass only. Table 1 shows the main-sequence lifetimes of stars with initial masses up to $15\,\mathrm{M}_\odot$, and the corresponding remnant masses. In order to facilitate comparison with F-P calculations (CW, and TPZ), we use the same lifetimes and remnant masses as CW. For stars of mass $m < 4\,\mathrm{M}_\odot$, the remnants are white dwarfs of mass $0.58{+}0.22\,(m{-}1)$, while for $m > 8\,\mathrm{M}_\odot$, the remnants are neutron stars. Stars with intermediate masses are completely destroyed (Iben & Renzini 1983). The lowest initial mass considered by CW was $\simeq 0.83\,\mathrm{M}_\odot$. For lower mass stars, in order to maintain consistency with TPZ, we extrapolate the lifetimes assuming a simple $m^{-3.5}$ scaling (Drukier 1995). We interpolate the values given in Table 1 using a cubic spline to obtain lifetimes for stars with intermediate masses, up to $15\,\mathrm{M}_\odot$. In our initial models (see §2.3), we assign masses to stars according to a continuous power-law distribution. This provides a natural spread in their lifetimes, and avoids having large numbers of stars undergoing identical stellar evolution. In contrast, in F-P calculations, the mass function is approximated by 20 discrete logarithmically spaced mass bins over the entire range of masses. The mass in each bin is then reduced linearly in time from its initial mass to its final (remnant) mass, over a time interval equal to the maximum difference in main-sequence lifetimes spanned by the stars in that mass bin (see TPZ for further details). This has the effect of averaging the effective mass loss rate over the masses in each bin.

We assume that all stars in the cluster were formed in the same star formation

$m_{initial}[M_\odot]$	$\log(\tau_{MS}[yr])$	$m_{final}[M_\odot]$
0.40	11.3	0.40
0.60	10.7	0.49
0.80	10.2	0.54
1.00	9.89	0.58
2.00	8.80	0.80
4.00	7.95	1.24
8.00	7.34	0.00
15.00	6.93	1.40

Table 4.1: Main-Sequence Lifetimes and Remnant Masses. For consistency, we use the same main-sequence lifetimes and remnant masses as CW, from Iben & Renzini (1983) and Miller & Scalo (1979).

epoch, and hence all stars have the same age throughout the simulation. During each timestep, all the stars that have evolved beyond their main-sequence lifetimes are labelled as remnants, and their masses are changed accordingly. In the initial stages of evolution ($t \lesssim 10^8$ yr), when the mass loss rate due to stellar evolution is highest, care is taken to make the timestep small enough so that no more than 1% of the total mass is lost in a single timestep. This is to ensure that the system remains very close to virial equilibrium through this phase.

4.2.3 Initial Models

The initial condition for each simulation is a King model with a power-law mass spectrum. In order to facilitate comparison with the F-P calculations of CW and TPZ, we select the same set of initial King models for our simulations, with $W_0 = 1$, 3, and 7. Most of our calculations were performed with $N = 10^5$ stars, with a few calculations repeated with $N = 3 \times 10^5$ stars and showing no significant differences in the evolution. We construct the initial model by first generating a single-component King model with the selected W_0. We then assign masses to the stars according to a

power-law mass function

$$f(m) \propto m^{-\alpha}, \tag{4.1}$$

with m between $0.4\,M_\odot$ and $15\,M_\odot$. We consider three different values for the power-law index $\alpha = 1.5$, 2.5, and 3.5, assuming no initial mass segregation. Although this method of generating a multi-component initial King model is convenient and widely used to create initial conditions for numerical work (including N-body, F-P, and Monte-Carlo simulations), the resulting initial model is not in strict virial equilibrium since the masses are assigned independently of the positions and velocities of stars. However, we find that the initial clusters relax to virial equilibrium within just a few timesteps in our simulations. Virial equilibrium is then maintained to high accuracy during the entire calculation, with the virial ratio $2T/|W| = 1$ to within $< 1\%$.

In addition to selecting the dimensionless model parameters W_0, N, and α (which specify the initial dynamical state of the system), we must also relate the dynamical timescale with the stellar evolution timescale for the system. The basic unit of time in our models is scaled to the relaxation time. Since the stellar evolution timescale is not directly related to the dynamical timescale, the lifetimes of stars (in years) cannot be computed directly from our code units. Hence, in order to compute the mass loss due to stellar evolution, we must additionally relate the two timescales by converting the evolution time to physical units. To maintain consistency with F-P calculations, we use the same prescription as CW. We assume a value for the initial relaxation time of the system, which is defined as follows:

$$t_{\rm r} = 2.57\,F\ [\mathrm{Myr}], \tag{4.2}$$

where

$$F \equiv \frac{M}{\mathrm{M}_\odot}\frac{R_{\rm g}}{\mathrm{kpc}}\frac{220\ \mathrm{km\,s^{-1}}}{v_{\rm g}}\frac{1}{\ln N}. \tag{4.3}$$

Here M is the total mass of the cluster, $R_{\rm g}$ is its distance to the Galactic center (assuming a circular orbit), $v_{\rm g}$ is the circular speed of the cluster, and N is the total number of stars. (This expression for the relaxation time is derived from CW's eqs. [1],

[2], and [6] with $m = \mathrm{M}_\odot$, $r = r_\mathrm{t}$, and $c_1 = 1$.) Following CW, a group of models with the same value of F (constant relaxation time) at the beginning of the simulation is referred to as a "Family." Our survey covers CW's Families 1, 2, 3 and 4. For each value of W_0 and α, we consider four different models, one from each Family.

To convert from our code units, or "virial units" (see Chapter 2, §2.8 for details) to physical units, we proceed as follows. For a given Family (i.e, a specified value of F), cluster mass M, and N, we compute the distance to the Galactic center R_g using equation (3). The circular velocity of 220 $\mathrm{km\,s^{-1}}$ for the cluster (combined with R_g) then provides an inferred value for the mass of the Galaxy M_g contained within the cluster orbit. Using M, M_g, and R_g, we compute the tidal radius for the cluster, as $r_t = R_g\,(M/3M_g)^{1/3}$, in physical units (pc). The ratio of the tidal radius to the virial radius (i.e., r_t in code units) for a King model depends only on W_0, and hence is known for the initial model. This gives the virial radius in pc. The unit of mass is simply the total initial cluster mass M. Having expressed the units of distance and mass in physical units, the unit of evolution time (which is proportional to the relaxation time) can easily be converted to physical units (yr) using equation (31) from Chapter 2.

Table 4.2 shows the value of F for the four selected Families. For reference, we also give the relaxation time at the half-mass radius t_rh for the models with $W_0 = 3$ and $\alpha = 2.5$ (mean stellar mass $\bar{m} \simeq 1\,\mathrm{M}_\odot$), which we compute using the standard expression (see, e.g., Spitzer 1987),

$$t_\mathrm{rh} = 0.138 \frac{N^{1/2} r_\mathrm{h}^{3/2}}{\bar{m}^{1/2} G^{1/2} \ln N}, \tag{4.4}$$

where r_h is the half-mass radius of the cluster.

4.3 Results

In Chapter 3 we presented our first results for the evolution of single-component clusters up to core collapse. We computed core-collapse times for the entire sequence

Family	F	$t_{\rm rh}$ [Gyr]	R_g [kpc]
1	5.00×10^4	2.4	5.8
2	1.32×10^5	6.4	15
3	2.25×10^5	11	26
4	5.93×10^5	29	68

Table 4.2: Family Properties: Sample parameters for Families 1–4, for a $W_0 = 3$ King model, with $\bar{m} = 1\mathrm{M}_\odot$, and $N = 10^5$. Distance to the Galactic center R_g is computed assuming that the cluster is in a circular orbit, filling its Roche lobe at all times.

of King models ($W_0 = 1 - 12$), including the effects of a tidal boundary. Here we extend our study to clusters with a power-law mass spectrum, and mass loss due to stellar evolution.

4.3.1 Qualitative Effects of Tidal Mass Loss and Stellar Evolution

We begin by briefly reviewing the evolution of single-component, tidally truncated systems. In Figure 4-1, we show the core-collapse times for King models with $W_0 = 1 - 12$ (see Chapter 3). The core-collapse times for tidally truncated models are compared with equivalent isolated models. Although the isolated models also begin as King models with a finite tidal radius, the tidal boundary is not enforced during their evolution, allowing the cluster to expand freely. The most notable result is that the maximum core-collapse time for the tidally truncated clusters occurs at $W_0 \simeq 5$, compared to $W_0 = 1$ for isolated clusters. This is because the low W_0 King models have a less centrally concentrated density profile, and hence a higher density at the tidal radius compared to the high W_0 models. This leads to higher mass loss through the tidal boundary, which reduces the mass of the cluster and shortens the core-collapse time. This effect is further complicated by the introduction of a non-trivial mass spectrum, and mass loss due to stellar evolution in the cluster.

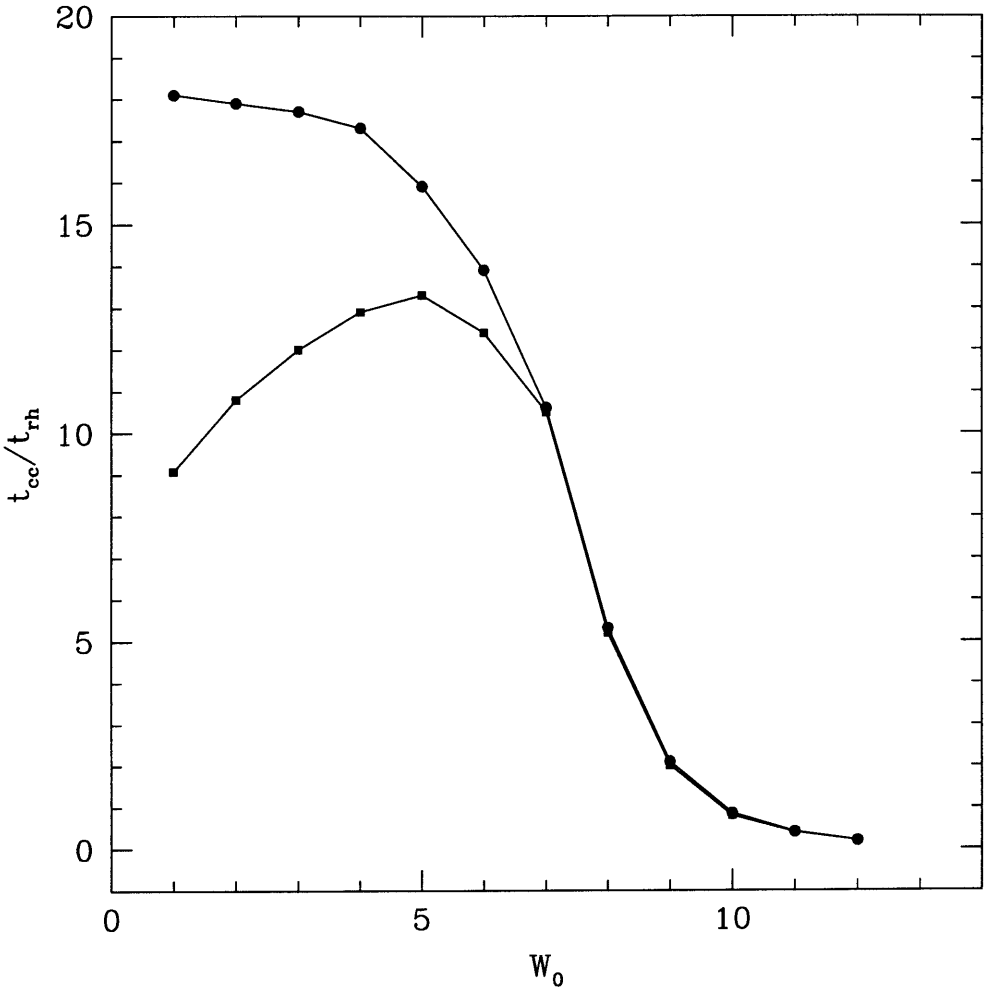

Figure 4-1: Comparison of core-collapse times for $W_0 = 1-12$ single-component King models. Isolated models, i.e., without an enforced tidal boundary, are indicated by solid circles, while tidally truncated models are indicated by squares.

In Figure 4-2, we show a comparison of the mass loss rate due to the tidal boundary, a power-law mass spectrum, and stellar evolution. We consider the evolution of a $W_0 = 3$ King model, in four different environments. All models considered in this comparison belong to Family 1 (cf. §2.2). We first compare an isolated, single component model (without an enforced tidal boundary), and a tidally truncated model (as in fig. [1]). Clearly, the presence of the tidal boundary is responsible for almost all the mass loss from the cluster, and greatly reduces the core-collapse time. Introducing a power-law mass spectrum further reduces the core-collapse time, since mass segregation increases the core density, and accelerates the development of the gravothermal instability. The shorter core-collapse time reduces the total loss through the tidal boundary by leaving less time for relaxation in the outer regions, and also lowering the density in the outer regions through mass segregation. This results in a higher final mass compared to the single-component system. Finally, allowing mass loss through stellar evolution causes even faster overall mass loss, which eventually disrupts the system. The introduction of a Salpeter-like power-law initial mass function ($\alpha = 2.5$) is sufficient to cause this cluster to disrupt before core collapse.

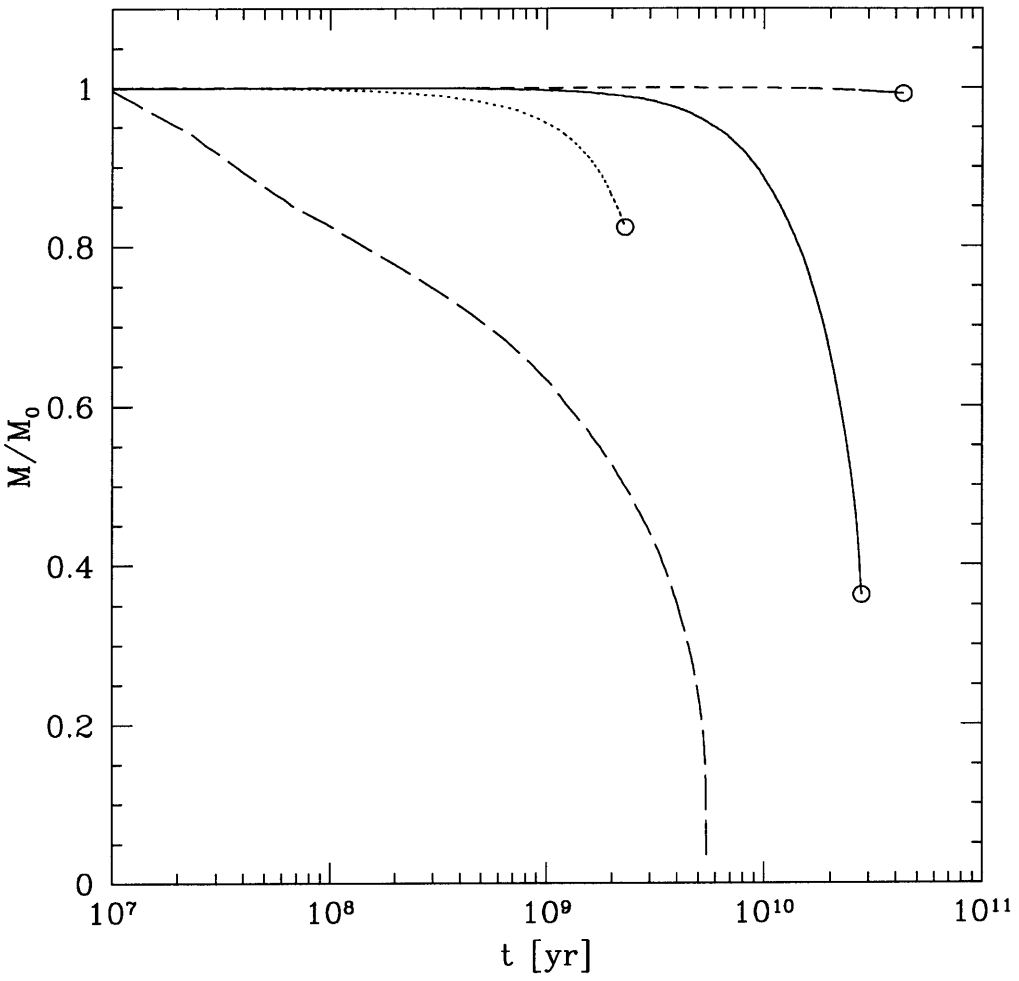

Figure 4-2: Comparison of the mass loss rate in a $W_0 = 3$ King model due to a tidal boundary, a power-law mass spectrum, and stellar evolution. The mass of the cluster, in units of the initial mass M_0, is shown as a function of time. The solid and short-dashed lines are for a single-component model, with and without a tidal boundary, respectively. The dotted line shows a model with a power-law mass spectrum, with $\alpha = 2.5$, and a tidal boundary. The long-dashed line is for a more realistic model with a tidal boundary, power-law mass spectrum, and stellar evolution. The circle at the end of the line indicates core collapse. The line without a circle indicates disruption of the cluster.

The presence of a tidal boundary causes stars on radial orbits in the outer regions of the cluster to be preferentially removed. This produces a significant anisotropy in the outer regions as the cluster evolves. As noted in Chapter 3, a proper treatment of this anisotropy is essential in computing the mass loss rate. A star in an orbit with low angular momentum has a larger apocenter distance compared to a star (with the same energy) in a high angular momentum orbit. Hence stars in low angular momentum (i.e., radial) orbits are preferentially lost through the tidal boundary, causing an anisotropy to develop in the cluster. In 1-D F-P models, this is not taken into account, and therefore 1-D F-P models predict a much larger mass loss compared to 2-D models. In Figure 4-3, we show the anisotropy parameter $\beta = 1 - \sigma_t^2/\sigma_r^2$, for a $W_0 = 3$ King model ($\alpha = 2.5$, Family 1), at two different times during its evolution. Here, σ_t and σ_r are the 1-D tangential and radial velocity dispersions, respectively. The initial King model is isotropic. At later times, the anisotropy in the outer region grows steadily as the tidal radius moves inward.

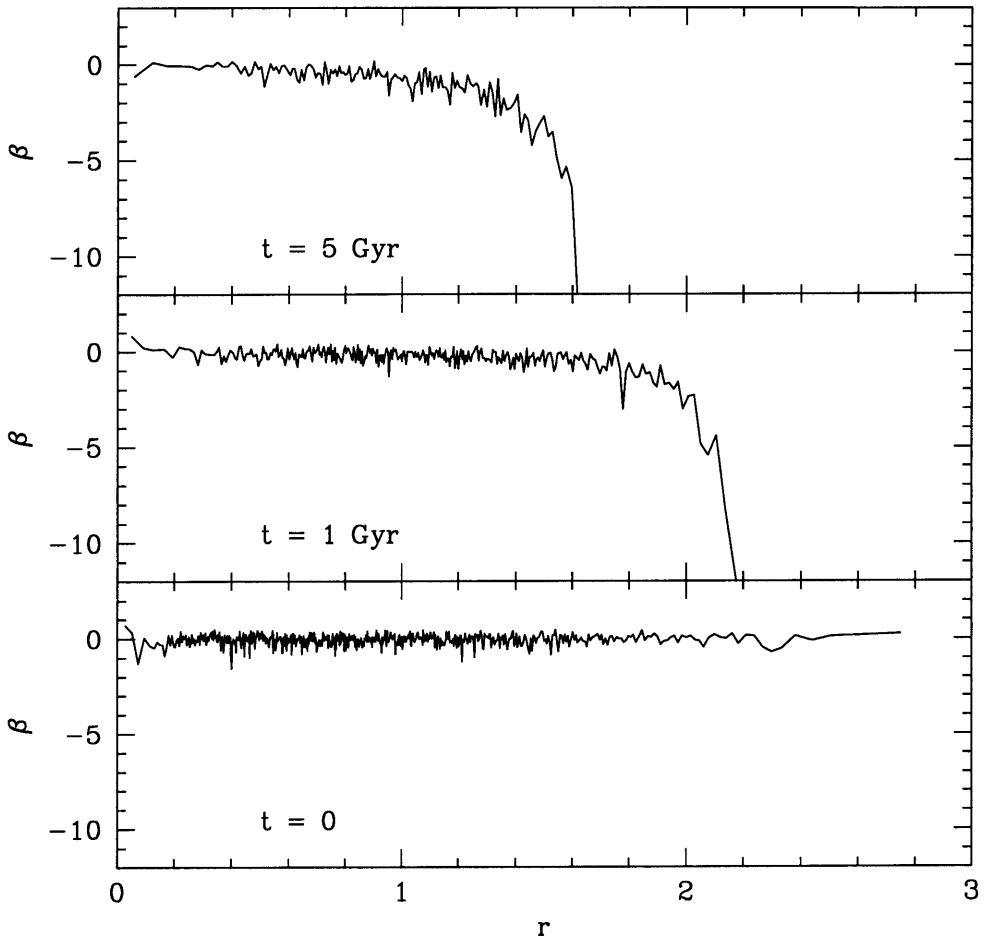

Figure 4-3: Evolution of the anisotropy parameter $\beta = 1 - \sigma_t^2/\sigma_r^2$ for a $W_0 = 3$ King model ($\alpha = 2.5$, Family 1). The bottom frame shows the initial isotropic King model. The top frame shows the anisotropy just before disruption. The radius is in units of the virial radius. Stars on highly eccentric orbits with large apocenter distances in the cluster are preferentially removed, causing σ_t^2/σ_r^2 to increase in the outer region.

4.3.2 Cluster Lifetimes: Comparison with Fokker-Planck results

We now present our survey of cluster lifetimes, and we compare our results with equivalent 1-D and 2-D F-P results. For each combination of W_0 and α, we perform four different simulations (Families $1-4$), corresponding to different initial relaxation times (cf. Table [4.2]). We follow the evolution until core collapse, or disruption, whichever occurs first. We also stop the computation if the total bound mass decreases below 2% of the initial mass, and consider the cluster to be disrupted in such cases. We compare our results with those of two different F-P studies: the 1-D F-P calculations of Chernoff & Weinberg (1990, CW), and the more recent 2-D calculations of Takahashi & Portegies Zwart (1999, TPZ).

Comparison with 1-D Fokker-Planck models

Table 4.3 compares our Monte-Carlo (MC) models with the 1-D F-P calculations conducted by CW. Following the same notation as CW, the final core collapse of a cluster is denoted by 'C', and disruption is denoted by 'D'. The final mass of the cluster (in units of the initial mass) and the lifetime in units of 10^9 yr (time to disruption or core collapse) are also given. The evolution of clusters that reach core collapse is not followed beyond the core-collapse phase. For disrupting clusters, CW provide a value for the final mass, which corresponds to the point at which the tidal mass loss becomes unstable and the cluster disrupts on the dynamical timescale. However, we find that the point at which the instability develops depends sensitively on the method used for computing the tidal mass loss and requires the potential to be updated on a very short timescale. In this regime, since the system evolves (and disrupts) on the dynamical timescale, the orbit-averaged approximation used to solve the Fokker-Planck equation also breaks down. This is true for both Monte-Carlo and F-P simulations. The only way to determine the point of instability reliably is to follow the evolution on the dynamical timescale using direct N-body integrations. Hence, for disrupting models, we quote the final mass as zero, and only provide the

disruption time (which can be determined very accurately).

We find that *all* our Monte-Carlo models disrupt later than those of CW. However, for models that undergo core collapse, the core-collapse times are earlier in some cases compared to CW. The discrepancy in the disruption times sometimes exceeds an order of magnitude (e.g., $W_0 = 1$, $\alpha = 2.5$). On the other hand, the discrepancy in the lifetime of the clusters with $\alpha = 1.5$ and $W_0 = 1$ and those with $W_0 = 3$ is only a factor of three. These models disrupt very quickly and a proper treatment of anisotropy does not extend their lifetimes very much, since the combination of a flat initial mass function and a shallow initial potential leads to rapid disruption.

Out of 36 models, we find that half (18) of our Monte-Carlo models reach core collapse before disruption, compared to fewer than 30% (10) of models in the CW survey. The longer lifetimes of our models allow more of the clusters to reach core collapse in our simulations. All the clusters that experience core collapse according to CW also experience core collapse in our calculations. Since the main difference between our models and those of CW comes from the different mass loss rates, we predictably find that our results match more closely those of CW in all cases where the overall mass loss up to core collapse is relatively small. For example, the more concentrated clusters ($W_0 = 7$) with steep mass functions (α =2.5 and 3.5) show very similar behavior, with the discrepancy in final mass and core-collapse time being less than a factor of two. However, we cannot expect complete agreement even in these cases, since the effects of anisotropy cannot be completely ignored.

The overall disagreement between our Monte-Carlo models and 1-D F-P models is very significant. This was also evident in some of the results presented in Chapter 3, where we compared core-collapse times for tidally truncated single-component King models, with 1-D F-P calculations by Quinlan (1996). This discrepancy has also been noted by Takahashi & Portegies Zwart (1998), and Portegies Zwart et al. (1998). The improved 2-D F-P code developed by Takahashi (1995, 1996, 1997) is now able to properly account for the anisotropy, allowing a more meaningful comparison with other 2-D calculations, including our own.

W_0	α	**Family**	**1**	**Family**	**2**	**Family**	**3**	**Family**	**4**
		CW	**MC**	**CW**	**MC**	**CW**	**MC**	**CW**	**MC**
1	1.5	D	D	D	D	D	D	D	D
		0.0092	0.03	0.0094	0.03	0.0093	0.03	0.0092	0.03
		0	0	0	0	0	0	0	0
	2.5	D	D	D	D	D	D	D	D
		0.034	0.55	0.034	0.62	0.035	0.66	0.034	0.70
		0	0	0	0	0	0	0	0
	3.5	D	C	D	C	D	D	D	D
		2.5	27	2.9	52	3.1	58	3.2	85
		0	0.12	0	0.02	0	0	0	0
3	1.5	D	D	D	D	D	D	D	D
		0.014	0.032	0.014	0.032	0.014	0.032	0.014	0.032
		0	0	0	0	0	0	0	0
	2.5	D	D	D	D	D	D	D	D
		0.28	5.2	0.29	8.8	0.29	10	0.29	11
		0	0	0	0	0	0	0	0
	3.5	C	C	C	C	D	C	D	C
		21.5	31	44.4	90	42.3	130	43.5	390
		0.078	0.28	0.035	0.23	0	0.20	0	0.18
7	1.5	D	C	D	C	D	C	D	C
		1.0	3.1	3.0	7.7	4.2	12	5.9	27
		0	0.08	0	0.05	0	0.05	0	0.05
	2.5	C	C	C	C	C	C	C	C
		9.6	3	22.5	6	35.5	10	83.1	20
		0.26	0.60	0.26	0.55	0.26	0.57	0.25	0.50
	3.5	C	C	C	C	C	C	C	C
		10.5	6.0	31.1	20	51.3	38	131.3	90
		0.57	0.80	0.51	0.70	0.48	0.68	0.49	0.67

Table 4.3: Comparison of Monte-Carlo results with 1-D Fokker-Planck calculations. The results of Chernoff & Weinberg (1990, CW) are taken from their Table 4.5. MC denotes our Monte-Carlo results. The first line describes the final state of the cluster at the end of the simulation: C indicates core collapse, while D indicates disruption. The second line gives the time to core collapse or disruption, in units of 10^9 yr. The third line gives the final cluster mass in units of the initial mass.

Comparison with 2-D Fokker-Planck models

Comparisons of the mass loss evolution is shown in Figures 4-4, 4-5, and 4-6, where the solid lines show our Monte-Carlo models, and the dashed lines show the 2-D F-P models from TPZ.

In Figure 4-4, we show the evolution of $W_0 = 1$ King models. The very low initial central density of these models makes them very sensitive to the tidal boundary, leading to very rapid mass loss. As a result, all the $W_0 = 1$ models disrupt without ever reaching core collapse. In addition, these models demonstrate the largest variation in lifetimes depending on their initial mass spectrum. For a relatively flat mass function ($\alpha = 1.5$), the disruption time is less than 3×10^7 yr. The large fraction of massive stars in these models, combined with the shallow initial central potential, leads to very rapid mass loss and complete disruption. For a more realistic, Salpeter-like initial mass function ($\alpha = 2.5$), the $W_0 = 1$ models have a longer lifetime, but still disrupt in $\lesssim 10^9$ yr. The $\alpha = 3.5$ models have very few massive stars, and hence behave almost like models without stellar evolution. We see that it is only with such a steep mass function, that the $W_0 = 1$ models can survive until the present epoch ($\gtrsim 10^{10}$ yr). We also find that the Family 1 and 2 models can just barely reach core collapse, despite having lost most of their mass. The Family 3 and 4 models are disrupted, having slightly higher mass loss rates.

We see very good agreement throughout the evolution between our Monte-Carlo models and the 2-D F-P models. In all cases, the qualitative behaviors indicated by the two methods are identical, even though the Monte-Carlo models consistently have somewhat longer lifetimes than the F-P models. The average discrepancy in the disruption times for all models is approximately a factor of two. The discrepancy in disruption times is due to a slightly lower mass loss rate in our models, which allows the clusters to live longer. Since the F-P calculations correspond to the $N \rightarrow \infty$ limit, they tend to overestimate the overall mass loss rate (we discuss this issue in more detail in the next section). This tendency has been pointed out by Takahashi & Portegies Zwart (1998), who compared the results of 2-D F-P simulations with those of

direct N-body simulations with up to $N = 32,768$. They have attempted to account for the finiteness of the system in their F-P models by introducing an additional parameter in their calculations to modify the mass loss rate. The comparison shown in Figures 4-4, 4-5 and 4-6 is for the unmodified $N \to \infty$ F-P models.

We find complete agreement with TPZ in distinguishing models that reach core collapse from those that disrupt. The only case in which there is some ambiguity is the $W_0 = 1, \alpha = 3.5$, Family 2 model, which collapses in our calculations, while TPZ indicate disruption. This is clearly a borderline case, in which the cluster reaches core collapse just prior to disruption in our calculation. Since the cluster has lost almost all its mass at core collapse, the distinction between core collapse and disruption is largely irrelevant. It is important to note, however, that we find the boundary between collapsing and disrupting models at almost exactly the same location in parameter space (W_0, α, and relaxation time) as TPZ. This agreement is as significant, if not more, than the comparison of final masses and disruption times.

In Figure 4-5, we show the comparison of $W_0 = 3$ King models. Again, the overall agreement is very good, except for the later disruption times for the Monte-Carlo models. The most notable difference from the $W_0 = 1$ models, is that the $W_0 = 3$ models clearly reach core collapse prior to disruption for $\alpha = 3.5$. The core collapse times for the $\alpha = 3.5$ models are very long ($\gtrsim 3 \times 10^{10}$ yr), with only a small fraction of the initial mass remaining bound at core collapse. Again, we find excellent agreement between the qualitative behaviors of the F-P and Monte-Carlo models.

In Figure 4-6, we show the evolution of the $W_0 = 7$ King models. In the presence of a tidal boundary, the $W_0 \simeq 5$ King models have the distinction of having the longest core-collapse times (see Fig. 4-1). This is because they begin with a sufficiently high initial core density, and do not expand very much before core collapse. Hence, the mass loss through the tidal boundary is minimal. King models with a lower W_0 lose more mass through the tidal boundary, and evolve more quickly toward core collapse or disruption, while models with higher W_0 have very high initial core densities, leading to short core-collapse times. All our $W_0 = 7$ models reach core collapse. Even the models with a relatively flat mass function ($\alpha = 1.5$) achieve core collapse,

although the final bound mass in that case is very small. We again see good overall agreement between the Monte-Carlo and F-P models. In the next section, we discuss the possible reasons for the small discrepancy in the mass loss rate between the Monte-Carlo and F-P models.

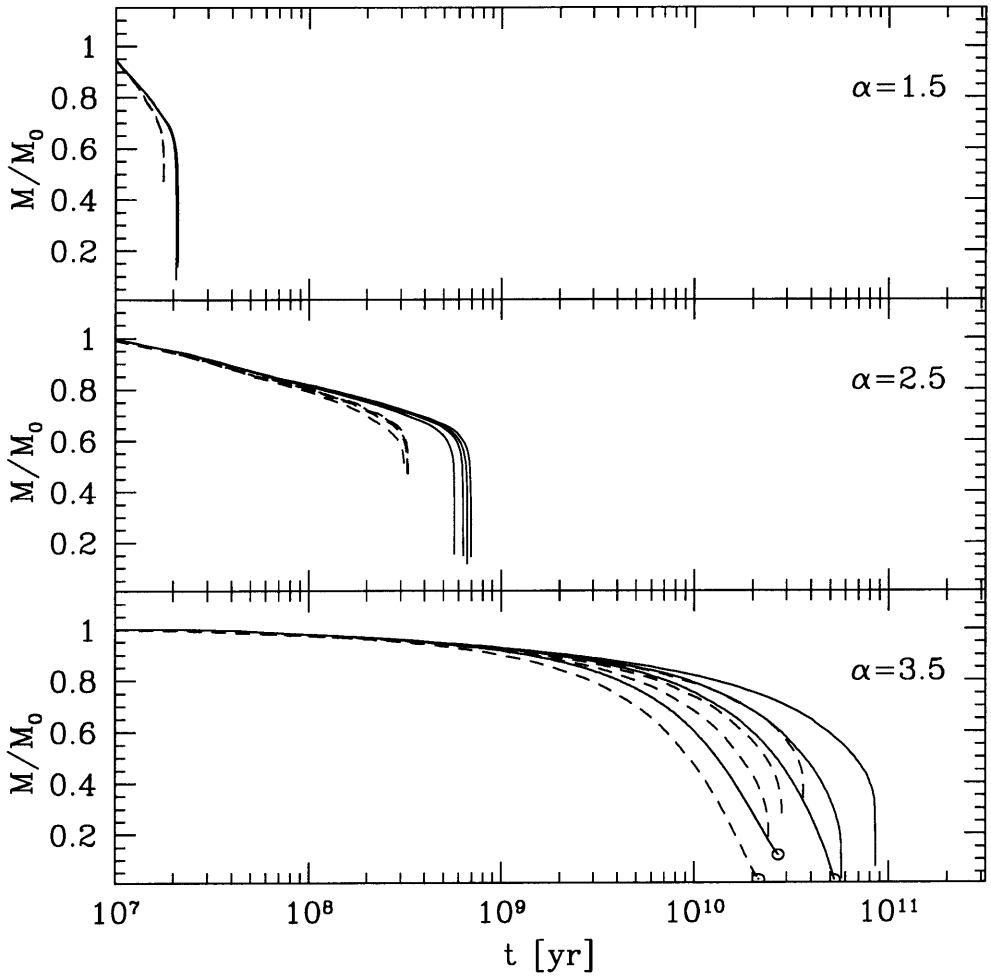

Figure 4-4: Evolution of the total mass with time for $W_0 = 1$ King models, Families 1–4. Comparison is made between our Monte-Carlo models (solid lines) and 2-D F-P models (dashed lines). The three panels show results for different values of the exponent α of the *initial* power-law mass function ($m^{-\alpha}$). The four lines for each case, represent Families $1-4$, from left to right. We indicate a core collapsed model with a circle at the end of the line. Lines without a circle at the end indicate disruption.

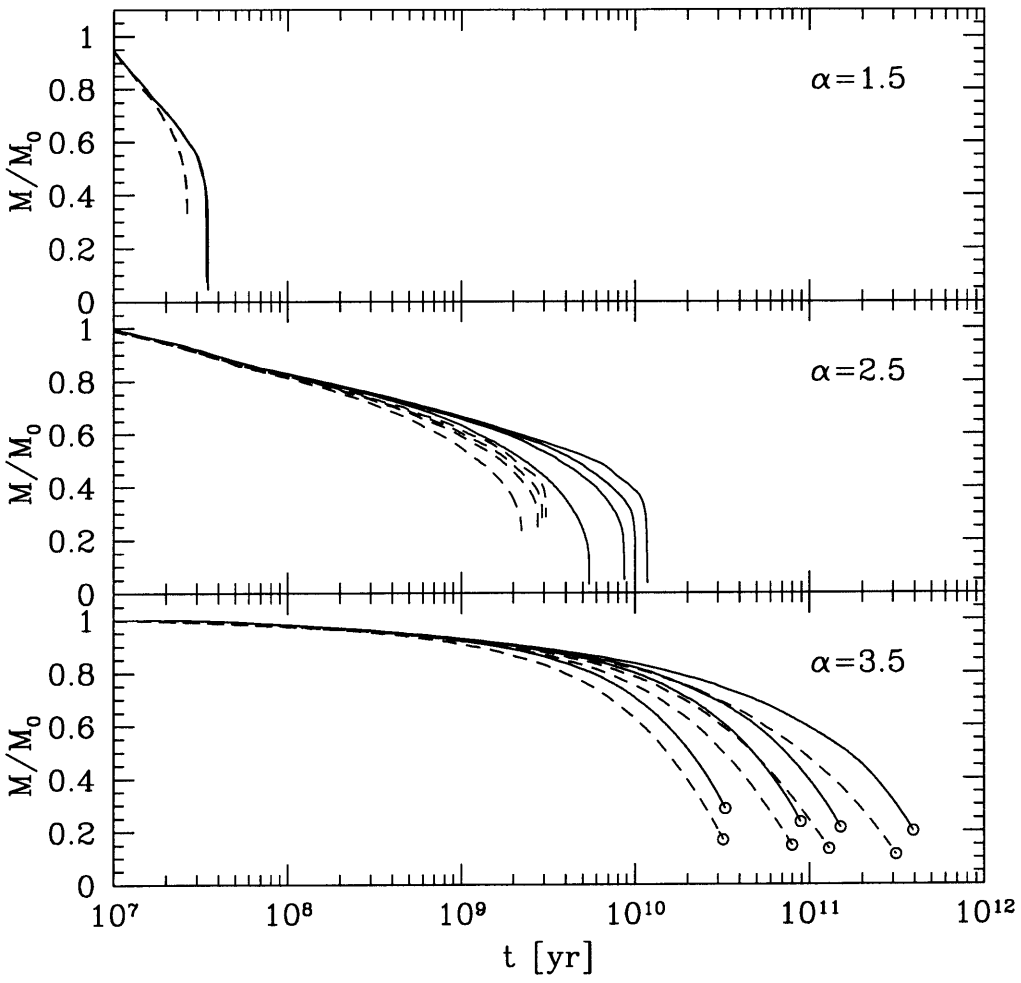

Figure 4-5: Same as Figure 4-4, but for $W_0 = 3$ King models.

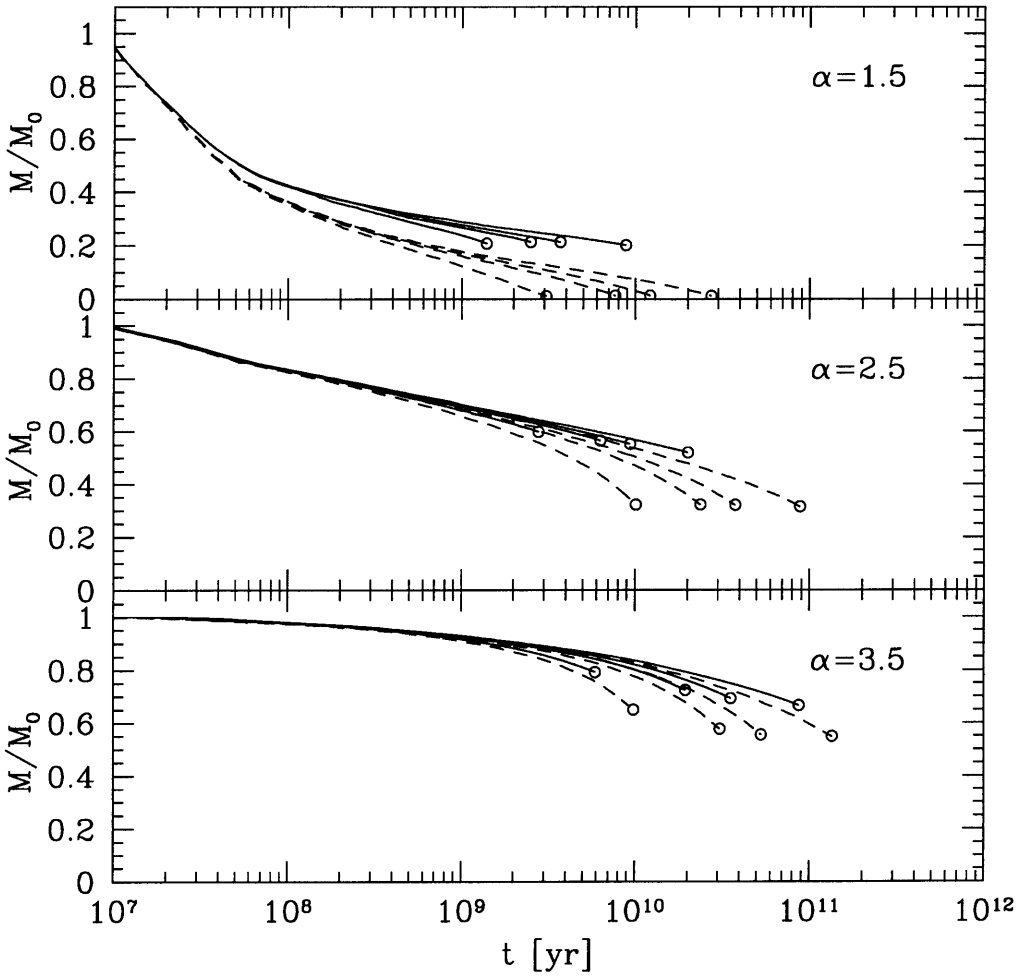

Figure 4-6: Same as Figure 4-4, but for $W_0 = 7$ King models.

Comparison with finite Fokker-Planck models

We first highlight some of the general issues relating to mass loss in the systems we have considered. In Figure 4-7, we show the relative rates of mass loss due to stellar evolution and tidal stripping, for W_0 =1, 3, and 7 King models, with different mass spectra ($\alpha = 1.5$, 2.5, and 3.5). We see that stellar evolution is most significant in the early phases, while tidal mass loss dominates the evolution in the later phases. The relative importance of stellar evolution depends on the fraction of massive stars in the cluster, which dominate the mass loss early in the evolution. Hence, the $\alpha = 1.5$ models suffer the greatest mass loss due to stellar evolution, accounting for up to 50% of the total mass loss in some cases (e.g., $W_0 = 7, \alpha = 1.5$). All models shown belong to Family 2. It is important to note the large variation in the timescales, and in the relative importance of stellar evolution versus tidal mass loss across all models.

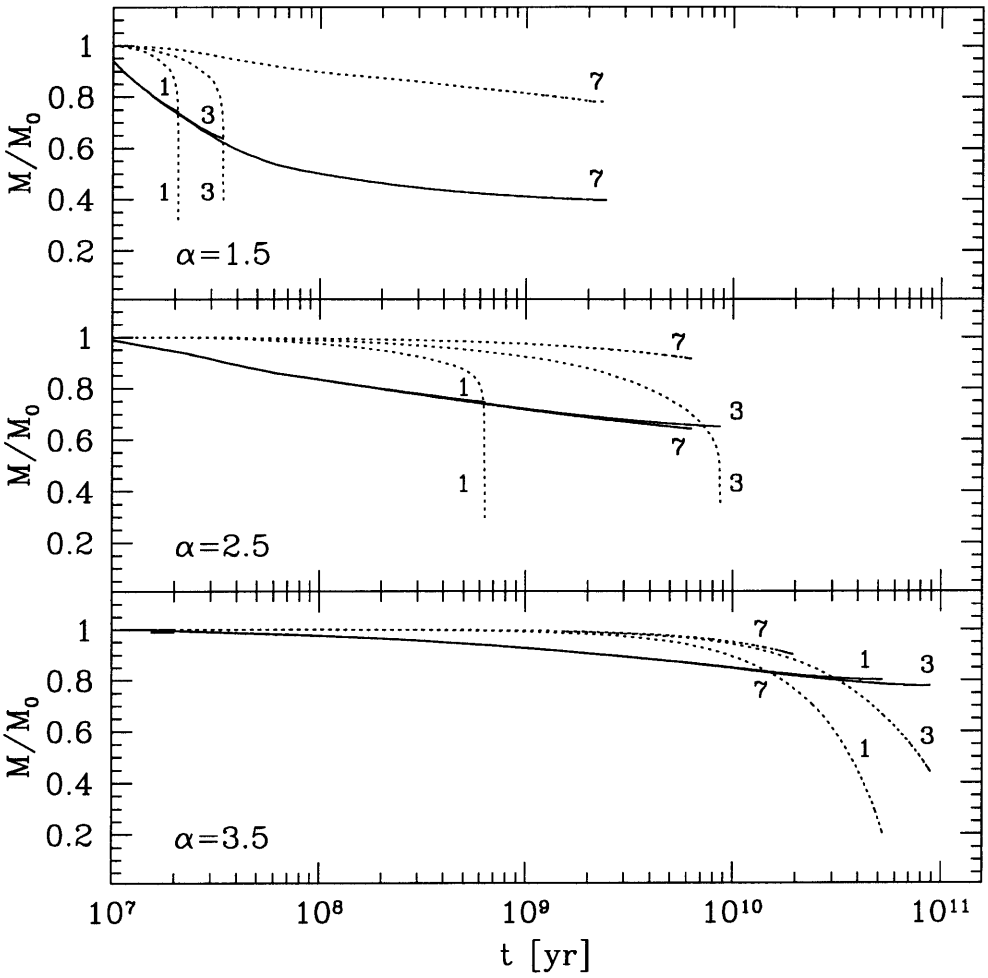

Figure 4-7: Comparison of the mass loss due to stellar evolution (solid lines), and mass loss due to tidal stripping of stars (dotted lines), for W_0 = 1, 3, and 7 King models, with initial mass functions $m^{-\alpha}$, α = 1.5, 2.5, and 3.5. The numbers 1, 3, and 7 next to the lines indicate an initial model with W_0 =1, 3, and 7, respectively. All models belong to Family 2. Results for other Families show similar trends. Note that the mass loss due to stellar evolution is almost independent of W_0 (as expected), but the tidal mass loss varies significantly with W_0. In the early phases of evolution, the mass loss due to stellar evolution dominates, while in the later stages, tidal stripping of stars is the dominant mechanism.

Through comparisons with N-body simulations, Takahashi & Portegies Zwart (1998) have argued that assuming $N \to \infty$ leads to an overestimate of the mass loss rate due to tidal stripping of stars. To compensate for this, they introduce a free parameter $\nu_{\rm esc}$ in their calculations, to account for the finite time (of the order of the crossing time) it takes for an escaping star to leave the cluster. They calibrate this parameter through comparisons with N-body simulations, for $N = 1,024 - 32,768$). Since for low N, the N-body models are too noisy, and the F-P models are insensitive to $\nu_{\rm esc}$ for large N, TPZ find that the calibration is most suitably done using $N \sim 16,000$ (for further details, see the discussion by TPZ). They show that a single value of this parameter gives good agreement with N-body simulations for a wide range of initial conditions. Using this prescription, TPZ provide results of their calculations for finite clusters with $N = 3 \times 10^5$ in addition to their $N \to \infty$ results. They find that their finite models, as expected, have lower mass loss rates, and consequently longer lifetimes compared to their infinite models.

In Table 4.4, we compare the results of our Monte-Carlo calculations with $N = 3 \times 10^5$ stars with the finite and infinite F-P models of TPZ. We consider four cases: $W_0 = 1$ and 3, Families 1 and 4, $\alpha = 2.5$. All finite TPZ models have longer lifetimes than their infinite models. However, there is practically no difference between their finite and infinite models for core-collapsing clusters. Hence we focus our attention only on the disrupting models. We see that in all four cases, the longer lifetimes of the finite models are in better agreement with our Monte-Carlo results, although the agreement is still not perfect. The largest difference between the finite and infinite F-P models is for $W_0 = 1$, Family 4, in which case the Monte-Carlo result lies in between the finite and infinite F-P results. In the remaining cases, the Monte-Carlo disruption times are longer than those of the finite F-P models.

Both Monte-Carlo and F-P methods are based on the orbit-averaged Fokker-Planck approximation, which treats all interactions in the weak scattering limit, i.e., it does not take into account the effect of strong encounters. Both methods compute the *cumulative* effect of distant encounters in one timestep (which is a fraction of the relaxation time). In this approximation, events on the crossing timescale (such as the

Model	Fokker-Planck ($N \to \infty$)	Fokker-Planck ($N = 3 \times 10^5$)	Monte-Carlo ($N = 3 \times 10^5$)
$W_0 = 1$, Family 1	3.1×10^8 yr	4.8×10^8 yr	5.5×10^8 yr
$W_0 = 1$, Family 4	3.3×10^8 yr	12.2×10^8 yr	7.0×10^8 yr
$W_0 = 3$, Family 1	2.2×10^9 yr	2.6×10^9 yr	5.3×10^9 yr
$W_0 = 3$, Family 4	3.1×10^9 yr	5.3×10^9 yr	10.1×10^9 yr

Table 4.4: Comparison of disruption times for infinite ($N \to \infty$) and finite ($N = 3 \times 10^5$) F-P models from TPZ with Monte-Carlo ($N = 3 \times 10^5$) models. All models have a mass function $m^{-\alpha}$ with $\alpha = 2.5$ ($\bar{m} = 1\mathrm{M}_\odot$).

escape of stars) are treated as being instantaneous. Since the relaxation time is proportional to $N/\ln N$ times the crossing time, this is equivalent to assuming $N \to \infty$ in the F-P models. However, in our Monte-Carlo models, there is *always* a finite N, since we maintain a discrete representation of the cluster at all times and follow the same phase space parameters as in an N-body simulation. Thus, although both methods make the same assumption about the relation between the crossing time and relaxation time, for all other aspects of the evolution, the Monte-Carlo models remain finite. This automatically allows most aspects of cluster evolution, including the escape of stars, stellar evolution, and computation of the potential, to be handled on a discrete, star-by-star basis. On the other hand, the F-P models use a few coarsely binned individual mass components represented by continuous distribution functions (consistent with $N \to \infty$) to model all processes. In this sense, the Monte-Carlo models can be regarded as being intermediate between direct N-body simulations and F-P models.

The importance of using the correct value of N in dynamical calculations for realistic cluster models has also been demonstrated through N-body simulations, which show that the evolution of finite clusters scales with N in a rather complex way (see Portegies Zwart et al. 1998 and the "Collaborative Experiment" by Heggie et al. 1999). Hence, despite correcting for the crossing time, it is not surprising that the finite F-P models are still slightly different from the Monte-Carlo models. It is also possible that the calibration of the escape parameter obtained by TPZ may not

be applicable to large N clusters, since it was based on comparisons with smaller N-body simulations. It is reassuring to note, however, that the Monte-Carlo models, without introducing any new free parameters, have consistently lower mass loss rates compared to the infinite F-P models, and show better agreement with the finite F-P models.

4.3.3 Velocity and Pericenter Distribution of Escaping Stars

A major advantage of the Monte-Carlo method is that it allows the evolution of specific subsets of stars, or even individual stars, to be followed in detail. We use this capability to examine, for the first time in a cluster simulation with realistic N, the properties of stars that escape from the cluster through tidal stripping. We also examine the differences between the properties of escaping stars in clusters that reach core collapse, and those that disrupt. In Figure 4-8, we show the distribution of escaping stars for two different models ($W_0 = 3$ and 7, Family 1, $\alpha = 2.5$). In each case, we show the distribution of the pericenter distance and the velocity at infinity for all the escaping stars. The velocity at infinity is computed as $v_\infty = \sqrt{2(E - \phi_t)}$, where E is the energy per unit mass of the star, and ϕ_t is the potential at the tidal radius. We see that the distribution of pericenters is very broad, indicating that escape takes place from within the entire cluster, and not just near the tidal boundary. We see that the distribution of pericenters is more centrally peaked in the $W_0 = 7$ model than in the $W_0 = 3$ case. This is because the collapsing cluster has a hotter core, which can lead to a higher escape rate from the center. In a disrupting cluster, the core never gets very dense, and hence the distribution of pericenter distances drops sharply near the center. Note that the sizes of the cores are very different for the two clusters. The $W_0 = 7$ cluster initially has a core radius of 0.2 (in virial units), which gets smaller as the cluster evolves, while the $W_0 = 3$ cluster has an initial core radius of 0.5, which does not change significantly as the cluster evolves. The striking difference between the clusters, however, is in the velocity distribution of escaping stars. In the disrupting cluster, the distribution shows a wide range of energies for the escaping stars. But in the collapsing cluster, the distribution is bimodal, with two

distinct peaks. The peak near zero velocity dominates the distribution. This peak represents stars escaping with close to the minimum energy, and hence from deep within the cluster. They must have very eccentric orbits in order to get beyond the tidal radius of the cluster. The smaller and wider peak represents the stars escaping from the outer region of the cluster. Since the density profile of a $W_0 = 7$ King model is quite steep, the density in the region near the tidal radius is relatively low. This limits the overall tidal mass loss from the outer regions of the cluster.

The bimodal velocity distribution for the collapsing cluster shows that there are two fundamentally different mechanisms for escape. It also suggests that the single escape parameter used by TPZ to correct for the tidal mass loss rate in their finite F-P calculations may be insufficient in correcting for both types of escaping stars. This might account for the fact that TPZ find almost no change in the mass loss rate after introducing their $\nu_{\rm esc}$ parameter in core-collapsing models, while disrupting models show a significant difference.

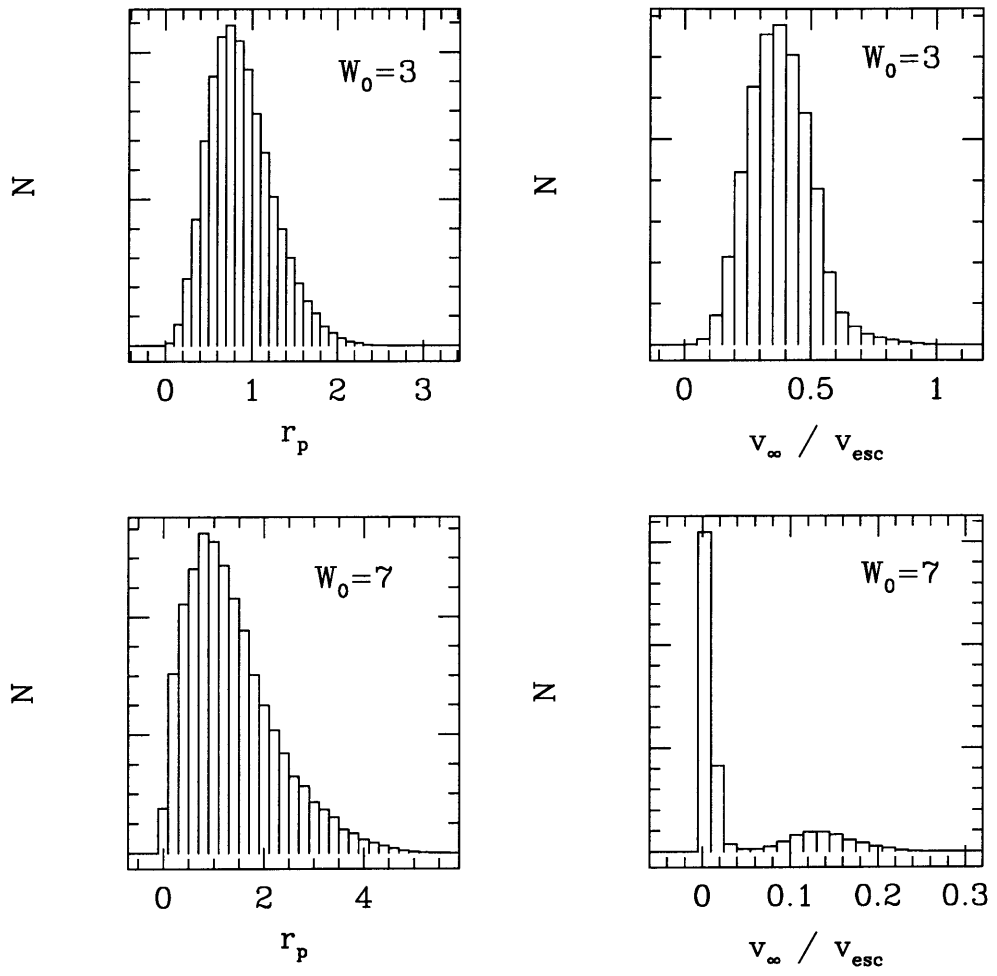

Figure 4-8: Distribution of the pericenter distance and velocity of the escaping stars, for two different King models: $W_0 = 3$ and 7 (Family 1, $\alpha = 2.5$). The $W_0 = 3$ model disrupts, while the $W_0 = 7$ model undergoes core collapse. The pericenter distance is given in units of the virial radius of the cluster. The velocity "at infinity" is computed as $v_\infty = \sqrt{2(E - \phi_t)}$, where E is the energy per unit mass of the star, and ϕ_t is the potential at the tidal radius. The escape velocity is defined as $v_{esc} = \sqrt{2(\phi_t - \phi_0)}$, where ϕ_0 is the potential at the center of the cluster. While the distribution of pericenter distances of escaping stars looks quite similar in the two clusters, the distribution of velocities is strikingly different. In the disrupting cluster ($W_0 = 3$), the escaping stars have a wide range of energies, whereas in the collapsing cluster ($W_0 = 7$), most stars escape with close to the minimum energy. The velocity distribution in the collapsing cluster also shows *two* distinct peaks, indicating that there are two fundamentally different mechanisms for escape.

4.3.4 Effect of Non-circular Orbits on Cluster Lifetimes

In all the calculations presented above (as in most previous numerical studies of globular cluster evolution), we assumed that the cluster remained in a circular orbit at a fixed distance from the center of the Galaxy. We also assumed that the cluster was born filling its Roche lobe in the tidal field of the Galaxy. Both of these assumptions are almost certainly unrealistic for the majority of clusters. However, one could argue that even for a cluster on an eccentric orbit, one might still be able to model the evolution using an appropriately *averaged* value of the tidal radius over the orbit of the cluster. We briefly explore the effect of an eccentric orbit, by comparing the evolution of one of our Monte-Carlo models ($W_0 = 3$, $\alpha = 2.5$, Family 2) on a Roche-lobe filling circular orbit, and on an eccentric orbit. We assume that the *pericenter* distance of the eccentric orbit is equal to the radius of the circular orbit. This is to ensure that the cluster fills its Roche lobe at the same location in the models being compared.

In Figure 4-9, we show the evolution of the selected model for three different orbits. The leftmost line shows the evolution for the circular orbit. The rightmost line shows the evolution for an eccentric *Keplerian* orbit with a typical eccentricity of 0.6 (see, e.g., Odenkirchen et al. 1997). The Keplerian orbit assumes that the inferred mass of the Galaxy interior to the circular orbit is held fixed for the eccentric orbit as well. The intermediate line shows the evolution for an orbit in a more realistic potential for the Galaxy, which is still spherically symmetric, but with a constant circular velocity of $220\,\mathrm{km\,s^{-1}}$ in the region of the cluster orbit (Binney & Tremaine 1987). The orbit is chosen so that it has the same pericenter and apocenter distance as the Keplerian orbit. However, since the orbital velocity is higher, it has a shorter period compared to the Keplerian orbit. In each of the two eccentric orbits, we see that the cluster lifetime is extended slightly (by a factor of ~ 2). Most of the mass loss takes place during the short time that the cluster spends near its pericenter, where it fills its Roche lobe. The Keplerian orbit gives the longest lifetime, since the cluster spends most of its time near its apocenter, where it does not fill its Roche lobe.

If we alternatively selected the orbit such that the cluster fills its Roche lobe at apocenter, instead of pericenter, the outcome would be obvious: the mass loss at pericenter would be considerably higher, leading to much more rapid disruption of the cluster compared to the circular orbit. This comparison indicates that the lifetime of a cluster can vary by a factor of a few, depending on the shape of its orbit. It also indicates that such corrections should be taken into account in building accurate numerical models of real clusters.

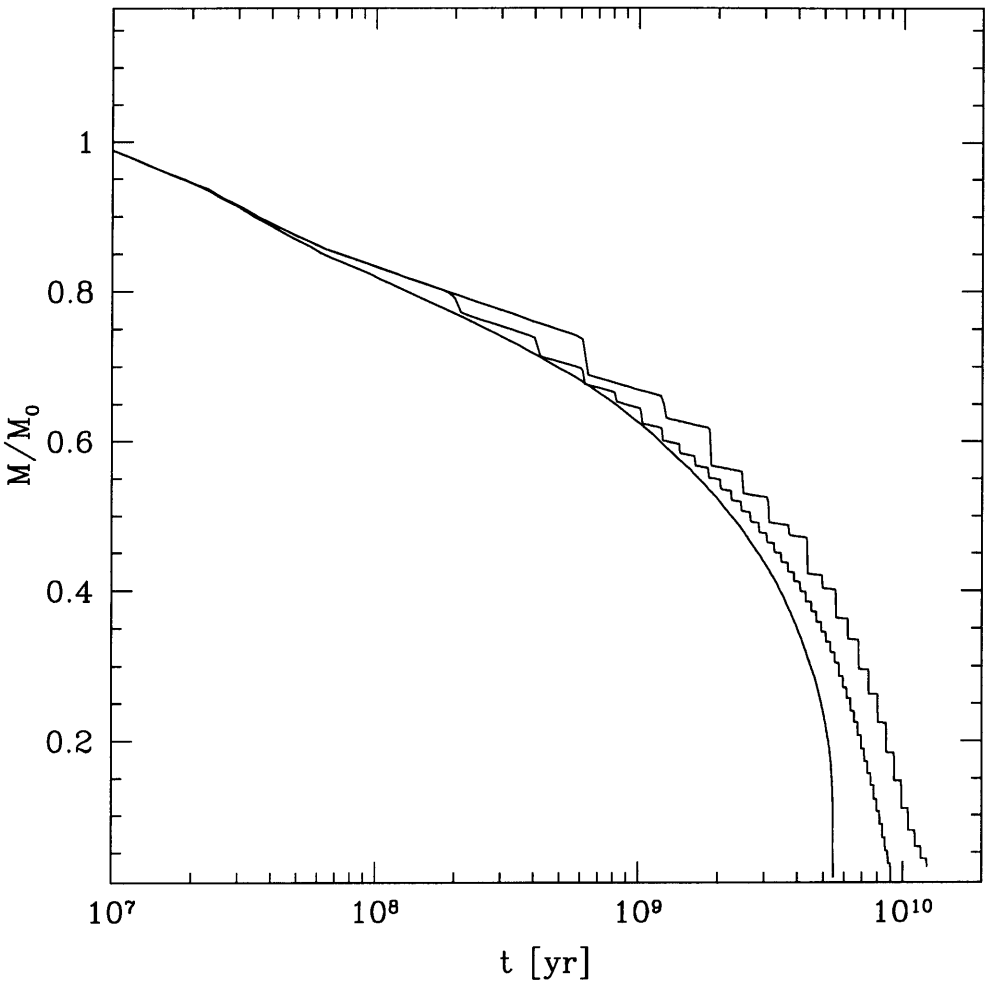

Figure 4-9: Comparison of the mass loss for a $W_0 = 3$, $\alpha = 2.5$ (Family 2) King model, on three different assumed orbits in the Galaxy. The leftmost line shows a circular orbit, with radius $R_g = 5.76$ kpc. The cluster is assumed to fill its Roche lobe at this distance. The rightmost line shows a Keplerian elliptical orbit with eccentricity 0.6 and a *pericenter* distance of 5.76 kpc. Since the cluster on such an orbit spends most of its time at a larger distance, the cluster does not fill its Roche lobe at all times. This results in a sharp mass loss every time the cluster approaches pericenter. The lifetime of the cluster is longer by almost a factor of 2. The intermediate line is for an orbit in a more realistic Galactic potential, with a constant circular velocity of $220\,\mathrm{km\,s^{-1}}$, with the same pericenter and apocenter distances as for the Keplerian elliptical orbit. The orbit is no longer elliptical, and the orbital period is shorter, resulting in a lifetime that is intermediate between the circular and elliptical cases.

4.4 Summary

We have calculated lifetimes of globular clusters in the Galactic environment using 2-D Monte-Carlo simulations with $N = 10^5 - 3 \times 10^5$ King models, including the effects of a mass spectrum, mass loss in the Galactic tidal field, and stellar evolution. We have studied the evolution of King models with $W_0 = 1$, 3, and 7, and with power-law mass functions $m^{-\alpha}$, with $\alpha = 1.5$, 2.5, and 3.5, up to core collapse, or disruption, whichever occurs first. In our broad survey of cluster lifetimes, we find very good overall agreement between our Monte-Carlo models and the 2-D F-P models of TPZ for all 36 models studied. This is very reassuring, since it is impossible to verify such results using direct N-body integrations for a realistic number of stars. The Monte-Carlo method has been shown to be a robust alternative for studying the evolution of multi-component clusters. It is particularly well suited to studying finite, but large-N systems, including many different processes, such as tidal stripping and stellar evolution, which operate on different timescales. We find that our Monte-Carlo models are in better agreement with the finite-N F-P models of TPZ, compared to their standard F-P ($N \rightarrow \infty$) models, although our models still appear to have a slightly lower overall mass loss rate.

Even though our simulations are getting more sophisticated and realistic with the inclusion of most of the dominant effects, there still remain substantial difficulties in relating our results directly to observed clusters. We ignore several important effects in these calculations, including the tidal shock heating of the cluster due to passages through the Galactic disk, and the presence of primordial binaries, which can support the core against collapse. In recent studies using 1-D F-P calculations, it has been shown that shock heating and shock-induced relaxation of clusters caused by repeated close passages near the bulge, and through the disk of the Galaxy can be as important as 2-body relaxation for their overall dynamical evolution (Gnedin, Lee, & Ostriker 1999). In addition, the initial mass function of clusters is poorly constrained observationally. In our study, we assume that clusters begin their lives filling their Roche lobes. But, as we have shown, a cluster on an eccentric orbit may

spend most of its time further away in the galaxy, where it might not fill its Roche lobe. This can lead to somewhat longer lifetimes.

The broad survey of cluster lifetimes presented here, and the similar effort by TPZ, lay the foundations for more detailed calculations, which may one day allow us to conduct reliable population synthesis studies to understand in detail the history, and predict the future evolution, of the Galactic globular cluster system.

Chapter 5

Mass Segregation and Equipartition in Globular Clusters

5.1 Introduction

In previous chapters, we have studied the evolution of isolated and tidally truncated globular clusters, taking into account the effects of a mass spectrum, stellar evolution, and a tidal radius. As we have seen in chapter 4, the time required for a cluster to reach core collapse is strongly dependent on the initial mass function (IMF), as well as on the central concentration of the initial model. In general, the presence of a mass spectrum speeds up the evolution, causing core collapse to occur earlier. This is mainly due to mass segregation, which quickly concentrates the heavier stars in the core while depleting the core of lighter stars. Clusters with a "flat" IMF ($m^{-\alpha}$ with $\alpha \lesssim 1.5$) evolve more than an order of magnitude faster than single component clusters, since they have larger numbers of massive stars. On the other hand, clusters with a steep IMF ($\alpha \gtrsim 3$) behave almost like single component clusters. Hence, the mass segregation timescale plays a crucial role in the pre-collapse evolution of clusters. The evolution of the cluster during the final core collapse, and in the post-collapse phase, is governed mostly by interactions involving binaries, which become more significant as the core density increases. We defer a detailed discussion of binary interactions until the next chapter, and instead focus here only on the pre-collapse

evolution during which mass segregation is most significant.

We have seen that the pre-collapse evolution is also affected by mass loss due to stellar evolution and tidal stripping of stars (cf. Chap. 4). The stellar evolution timescale is completely determined by the initial mass spectrum, since the main-sequence lifetimes of stars are (in principle) completely determined by their initial masses, at least in the case of stars which are not in binary systems. Similarly, the mass loss due to the tidal boundary is determined by the density profile of the cluster near the tidal boundary. Similarly, the mass segregation timescale for a component of a given mass m, is determined by the local relaxation time within the cluster, the mass ratio to the mean mass $m/\bar{m}$, and the overall mass spectrum. In this chapter, we examine the mass segregation timescale for massive ($m > \bar{m}$) stars, as well as for very low-mass stars ($m << \bar{m}$) in the pre-collapse phase. Since mass segregation is a direct consequence of the tendency of the system to move toward equipartition of kinetic energy between the various mass components, we also examine the approach toward equipartition during the pre-collapse evolution of clusters.

Our Monte-Carlo method is extremely well suited to study mass segregation in globular clusters, since it allows the orbital elements of each star, including the peri-center and apocenter distances of its orbit, to be followed easily. In N-body simulations, the exact pericenter and apocenter distances of stellar orbits are more difficult to compute in each timestep due to the complex regularization schemes implemented to obtain maximum computational efficiency, and hence the evolution of individual stellar orbits over time cannot be studied easily. On the other hand, in Fokker-Planck calculations, the entire cluster is represented as a continuous (smooth) distribution function, and hence well-defined orbits for individual stars are not available. Since our code combines the benefits of speed from the Fokker-Planck approximation, while maintaining the discrete representation of the system, it is perfectly suited to study the evolution of trace populations of interesting species of stars within clusters. We use that capability here to study mass segregation, by following the evolution of a small number ($N_{trace} = 1000$) of trace stars self-consistently within an evolving background cluster with $N = 10^5$.

5.2 Mass Segregation and Equipartition in Two-Component Clusters

[1]

Remarkable advances have been made over the last three decades in our understanding of spherical star clusters with two mass components. The two-component case is traditionally regarded as the second level of sophistication and therefore a logical challenge for new methods that have tackled the single-component case. Two-component clusters were originally examined because they better resemble real clusters, which contain a continuous spectrum of masses. While somewhat more realistic in this regard, clusters with only two mass components still represent a simplification with respect to real clusters. It has been suggested recently, however, that for a range of configurations in mass types and the relative size of the two populations, two-component clusters can resemble real clusters that are mostly comprised of neutron stars and main sequence stars (Kim, Lee, & Goodman 1998). Perhaps the best reason to examine a simplified model of any physical system, however, is to obtain a more profound understanding of individual processes.

Much of the discourse regarding two-component systems has focused upon the following questions. First, for what configurations of the cluster is dynamical equilibrium precluded (i.e., the system is not stable on dynamical time scales)? Second, for what configurations of the cluster is thermal equilibrium precluded (i.e., equipartition of kinetic energies between each component is not allowed)? Both questions originate from an analysis by Spitzer (1969), in which he noticed that simultaneous thermal and dynamical equilibrium was impossible for some clusters. In particular, the heavier stars sink into the center as they lose kinetic energy to the lighter stars during the approach to equipartition. If equipartition is not attained, then the heavier stars will continue sinking until their self-gravity dominates the cluster's potential in the core. Shortly thereafter, the heavier component will undergo a gravothermal collapse, forming a small dense core comprised mainly of the heavier stars (Spitzer 1969). Re-

[1] Based on the results in Watters, Joshi & Rasio 2000

finements to this analysis have obtained similar constraints upon the configurations of two-component clusters in dynamical and thermal equilibrium (Lightman & Fall 1978).

Several methods have been used to address questions about dynamical and thermal equilibrium in two-component systems. These include the construction and study of one-parameter families of models in dynamical equilibrium (Kondrat'ev & Ozernoy 1982; Katz & Taff 1983), Monte Carlo approaches to the numerical integration of the Fokker-Planck equation (Spitzer & Hart 1971), direct integration of the Fokker-Planck equation in phase space (Inagaki & Wiyanto 1984; Kim, Lee, & Goodman 1998), and also direct N-body simulations (Portegies Zwart & McMillan 2000). The majority of work using any one of these methods has been undertaken at least partly in order to confirm Spitzer's conclusion (Yoshizawa et al. 1978) or refute it (Merritt 1981).

Dynamical equilibrium is attained and maintained on time scales that are very short compared to the amount of time needed for relaxation or equipartition. A so-called "equilibrium model" (i.e., whose phase-space distribution function satisfies the equation for hydrostatic equilibrium) therefore resembles a possible stage or snapshot in the evolution of a dynamically stable cluster. It is interesting to construct a parameterized family of equilibrium models, for which equipartition is either assumed or the temperature ratio allowed to vary, in order to determine under what conditions the dynamical equilibrium becomes impossible. In the majority of previous work, the distribution functions of such families take the form of lowered Maxwellians or spatially-truncated isothermal spheres.

5.2.1 Theoretical Overview

According to Spitzer (1969), simultaneous dynamical and thermal equilibrium is impossible for two-component star clusters within a certain range of configurations. Let us consider a cluster with stars of two masses, m_1 and m_2, where $m_2 > m_1$. Moreover, let M_2 and M_1 be the total mass in each component. Spitzer assumed that $M_2 \ll M_1$, which is normally the case for real clusters. He concluded that for certain values of

the ratios M_2/M_1 and m_2/m_1, equipartition will not be attained as the heavier and lighter stars exchange kinetic energy, and hence the heavier stars will sink very far into the center. Moreover, the heat exchange with lighter stars promotes them to higher orbits, so that eventually insufficient numbers will remain in the center to conduct heat rapidly away from the heavier stars. If the mass-stratification proceeds far enough, then the self-gravity of the heavier stars will dominate the potential in the core, and this sub-system will undergo gravothermal collapse. The result is a very dense core comprised exclusively of heavier stars.

In his analysis, Spitzer begins by assuming global equipartition. Global equipartition is not realistic, however, because the relaxation and equipartition times vary greatly throughout the cluster, becoming longer than the age of the universe in the outer halo. In fact, we expect equipartition only in the inner region where relaxation times are shortest. His discussion is mostly unchanged by this, so long as we confine its relevance to processes in this inner region. Let v_{m1}^2 and v_{m2}^2 represent the mean-square velocities of stars in each component. As mentioned, Spitzer begins by assuming equipartition, i.e., the temperature ratio ξ is equal to unity,

$$\xi \equiv \frac{(1/2)m_2 v_{m2}^2}{(1/2)m_1 v_{m1}^2} = 1\,. \tag{5.1}$$

Spitzer assumes that (a) $M_2 \ll M_1$, and (b) $m_2 \gg m_1$, so that the heavier stars will be concentrated in the center of the system. Spitzer & Hart (1971) noticed that the second assumption often does not hold strictly. In particular, even far into the evolution many heavier stars can still reside well outside of the core. Merritt (1981) constructed equilibrium models that violate this assumption by great amounts and discovered that equipartition is possible for some (admittedly unrealistic) configurations which can be realized for all values of m_2/m_1 and M_2/M_1. Spitzer commits to assumptions (a) and (b), and obtains the following condition for equipartition to be possible (as a direct consequence of eq. [5.1]),

$$S \equiv \left(\frac{M_2}{M_1}\right)\left(\frac{m_2}{m_1}\right)^{3/2} < 0.16. \tag{5.2}$$

Spitzer suggests that for smaller values of the individual mass ratio m_2/m_1, the inequality (5.2) remains valid, except that $\beta \to 1$ as $m_2/m_1 \to 1$.

Lightman & Fall (1978) have also developed an approximate theory for the core collapse of two-component clusters which resembles that of Spitzer. They examined two constant-density isothermal spheres representing the cores of the heavier and lighter components, where the radius of the former is smallest. By applying a component-wise virial theorem and several simplifying assumptions, they find a set of four ordinary differential equations for the virial radii and total masses in each component. They obtain the following condition for equipartition of energies between the two components, where we let $\tilde{m} \equiv m_2/m_1$ and $\tilde{M} \equiv M_2/M_1$:

$$\Gamma(\tilde{m}, \tilde{M}) \equiv \tilde{m}^3 \tilde{M}^2 \left[\frac{27}{4} \left(1 + \frac{3\tilde{M}}{2\tilde{m}} \right) \left(1 + \frac{5}{2}\tilde{M} \right)^{-3} \right] \leq 1 \,. \tag{5.3}$$

5.2.2 Numerical Study of Equipartition in Two-Component Clusters

We illustrate the difference in the evolution of "stable" models (i.e., those models which satisfy the condition for equipartition between the two components in the core), and "unstable" models (in which equipartition is never attained). The evolution of the core temperature ratio ξ is shown in Figure 5-1 for three different two-component King models ($W_0 = 6$), with $S = 0.05$ (top), $S = 0.5$ (middle), and $S = 1.24$ (bottom). Figure 5-2 shows the core temperatures of the lighter stars (top) and the heavier stars (bottom) for the case $S = 1.24$. Several features that we expect and that have been mentioned already in §5.2.1 are easily recognizable. The temperature ratio begins with a value m_2/m_1 and then decreases gradually as equipartition is approached. It is clear that ξ reaches a minimum value that is greater than 1 for the case $S = 1.24$, so that equipartition is clearly never attained. Equipartition is nearly attained for $S = 0.5$, and $\xi_{\rm min} = 1$ to within 5% for $S = 0.05$. It is clear from Figure 5-2 that the heavier component cools initially, then maintains a constant mean kinetic energy, and then begins to heat prior to core collapse. At the same time,

the lighter component steadily becomes hotter as it receives energy from the heavier component. The temperature ratio in the last time steps becomes very noisy because the temperatures are computed using the relatively few stars that remain in the core.

The temperature ratio ξ reaches a minimum value at different times with respect to core collapse for each of the models shown in Figure 5-1. In cases where the minimum value is greater than 1, it sometimes appears that the gravothermal catastrophe has beaten the approach to equipartition. In such cases, one may ask whether an initial model with a less concentrated spatial distribution and a different initial relaxation time would yield a different minimum temperature ratio. In fact, we find that $\xi_{\rm min}$ is robust with respect to changes in the initial value of the dimensionless potential W_0. The evolution of the temperature ratio for three calculations, where $W_0 = 1$, 5, and 10 for $S = 1$ and $m_2/m_1 = 5$, are shown in Figure 5-3. In all three cases the minimum temperature ratio is approximately 1.55.

Approximate values of the minimum core temperature ratio $\xi_{\rm min}$ are plotted using three symbols in the parameter space determined by M_2/M_1 and m_2/m_1 in Figure 5-4 for 30 calculations in the set A. Also drawn are the Spitzer and Lightman-Fall "stability boundaries," above which simultaneous dynamical and thermal equilibrium are supposedly prohibited ($S = 0.16$ and $\Gamma = 1$, respectively; cf. eqs. [5.2] & [5.3]). We calculate $\xi_{\rm min}$ with a numerical accuracy of 5%. That is, $\xi_{\rm min}$ is calculated as the average core temperature ratio from 90% to 95% of the pre-collapse evolution, and this average has a standard deviation of approximately 0.05 in our calculations for $N = 10^5$ stars. Therefore, those calculations marked with a square in Figure 5-4 have been determined to reach equipartition within our numerical accuracy. One can see that the Spitzer boundary $S = 0.16$ is approximately respected for $m_2/m_1 \geq 2$. By comparison, the Lightman-Fall boundary falls well inside the range of clusters which have clearly not attained equipartition. In spite of this, the Lightman-Fall boundary better reproduces the shape of boundaries between regions of constant $\xi_{\rm min}$. A more properly-drawn Spitzer boundary has a similar shape, recalling that $\beta \to 1$ as $m_2/m_1 \to 1$. Based upon the results shown in Figure 5-4, we propose our

own condition for equipartition,

$$\Lambda \equiv \left(\frac{M_2}{M_1}\right)\left(\frac{m_2}{m_1}\right)^{2.4} \geq 0.32. \tag{5.4}$$

The boundary determined by equation (5.4) is valid for $1.75 < m_2/m_1 < 7$, and is also drawn in Figure 5-4. For $m_2/m_1 < 1.75$, equipartition is achieved for all clusters considered.

All of the calculations were terminated at core-collapse, at which time the radius containing 1% of the mass in the heavier component diminishes sharply. The time t_{cc} is measured at the instant when a number density of 10^8 is attained within the core. Values of the core collapse time t_{cc} for several values of m_2/m_1 are plotted in Figure 5-5. These trends confirm that the onset of core collapse is accelerated by the presence of a small and heavier subpopulation, in agreement with the findings of others (Quinlan 1996; Inagaki & Wiyanto 1984).

Finally, we concur with the findings of Spitzer & Hart (1971) that many heavier stars remain *outside* the core throughout the evolution. This is clear from plots of radii containing several percentages of the total mass in the heavier component which clearly exceed the core radius throughout the evolution (Fig. 5-6). This casts doubt on the assumption, committed in Spitzer's original analysis, that all of the heavier stars quickly become concentrated in the core (see §5.2.1). In particular, we find that for $S = 1.24$, $M_2/M_1 = 0.111$, and $m_2/m_1 = 5$, the radius containing 75% of the mass in the heavier component diminishes to only 50% of its initial value (and hence remains larger than the core radius) throughout the evolution. Nevertheless, by the onset of core collapse, we frequently observe for calculations with large m_2/m_1 that no lighter stars remain in the core. We explore the issue of mass segregation for lighter stars in more detail later in this chapter.

The temperature ratio ξ in Figure 5-1 initially has the value m_2/m_1. While this is an artifact of the way our initial models were constructed, m_2/m_1 happens also to be the most realistic value of ξ for equilibrium models with a relatively shallow potential. In families of equilibrium models it is typical to find that $\xi \to m_2/m_1$ as $W_0 \to 0$

(Kondrat'ev & Ozernoy 1982; Katz & Taff 1983). In trials for which initial models were modified so that ξ had some value other than m_2/m_1, a brief period of rapid relaxation ensued which restored the value m_2/m_1. This effect has been observed in simpler models of the evolution calculated using other methods (Lightman & Fall 1978).

In the core, the initial behavior of the temperature ratio is mostly determined by the temperature of the heavier component, while the mean kinetic energy of the lighter stars, which are more abundant at first, increases gradually (Figure 5-2). Spitzer (1969) suggested that the approach to equipartition is characterized by the exponential decay of kinetic energy in the heavier component, with a time constant equal to *twice* the so-called equipartition time,

$$t_{\rm eq} = t_{r1} \frac{3\pi^{1/2}}{16} \frac{m_1}{m_2} \left(1 + \frac{v_{m2}}{v_{m1}}\right)^{3/2}, \tag{5.5}$$

where t_{r1} is a relaxation time for the stars of mass m_1. In the case where the mean-square velocities of each component are initially equal, the initial equipartition time is $t_{\rm eq} \approx t_{r1}(m_1/m_2)$. (It should be noted that $t_{\rm eq}$ decreases as equipartition is approached.) This characterization of the decline in kinetic energy of heavier stars agrees very well with our results for stars contained within the half-mass radius, where we assume $t_{r1} \approx t_{\rm rh}$, the initial half-mass relaxation time for the cluster as a whole. In particular, the kinetic energy of the heavier component diminishes to a fraction $1/e$ of its initial value (after subtracting its minimum value for the entire evolution) within $0.39t_{\rm rh}$ for $S = 1$, $m_2/m_1 = 5$, and within $1.3t_{\rm rh}$ for $S = 0.5$, $m_2/m_1 = 1.5$, in good agreement with the theory (which predicts a time $t_{\rm eq} \approx 2t_{rh}\, m_1/m_2$). However, we find that equipartition is approached on a similar time scale in the core, where the theory predicts that $t_{\rm eq}$ should be shorter by approximately $1/5$, and hence agreement is poor (the ratio of initial core and half-mass relaxation times for King models with $W_0 = 6$ is approximately $1/5$; see Quinlan 1996). This discrepancy is most likely due to the incorrect assumption made earlier that the heavier component is concentrated in the core from the beginning. As we have shown, the heavier component

never confined entirely to the core, and a significant fraction remains outside the core throughout the evolution. Hence it is not surprising that the timescale on which equipartition is attained in the core is longer than that predicted by the theory.

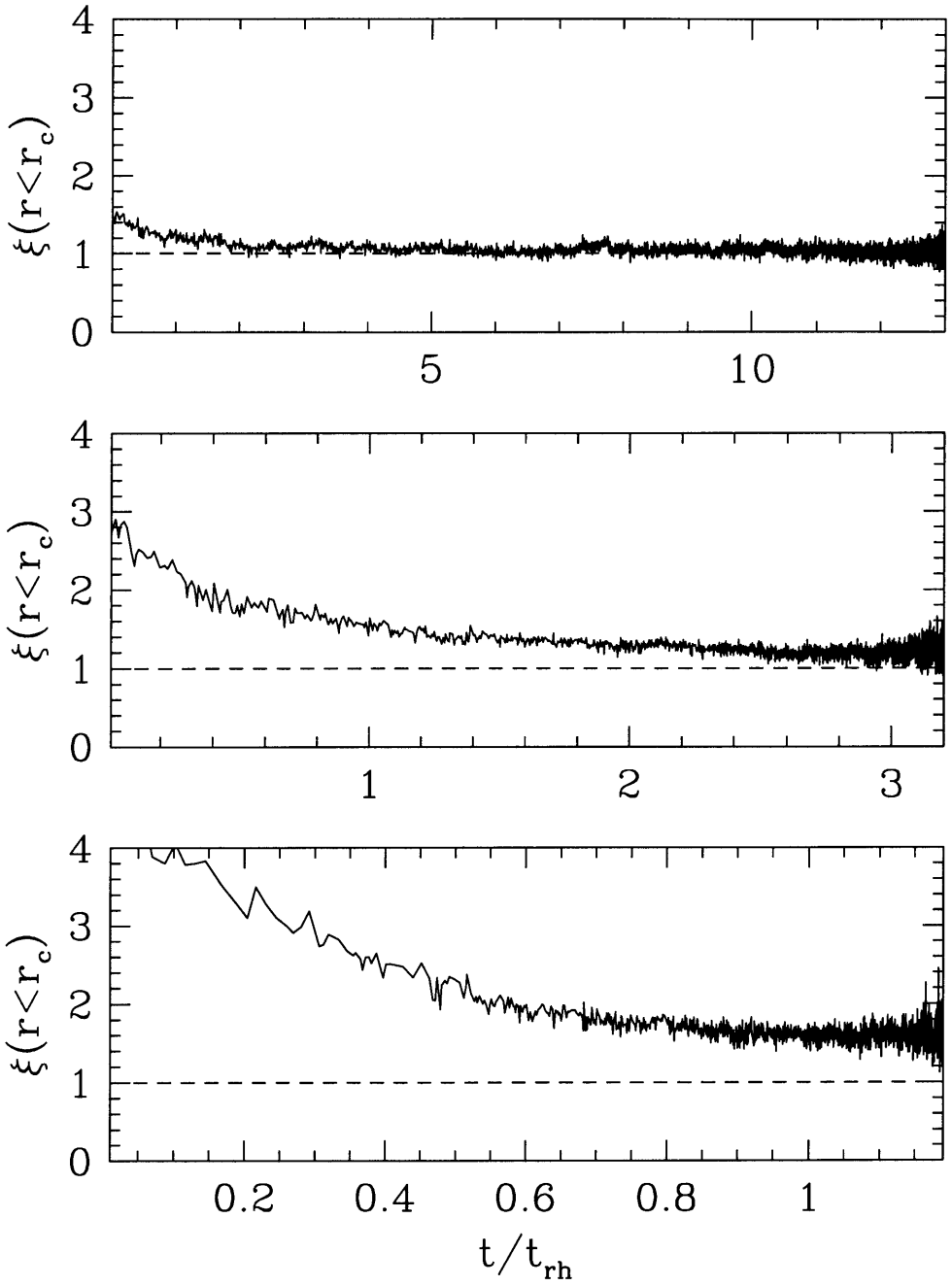

Figure 5-1: Evolution of the temperature ratio in the core for $S = 0.05$ and $m_2/m_1 = 1.5$ (top), $S = 0.5$ and $m_2/m_1 = 3$ (middle), and $S = 1.24$ and $m_2/m_1 = 5.0$ (bottom). The minimum temperature ratio attained in each calculation increases with S. Time is displayed in units of the initial half-mass relaxation time ($t_{\rm rh}$). In each case the evolution is shown until shortly before core collapse. Notice that core collapse occurs sooner with increasing S. The initial condition in each case was a two-component King model with $W_0 = 6$.

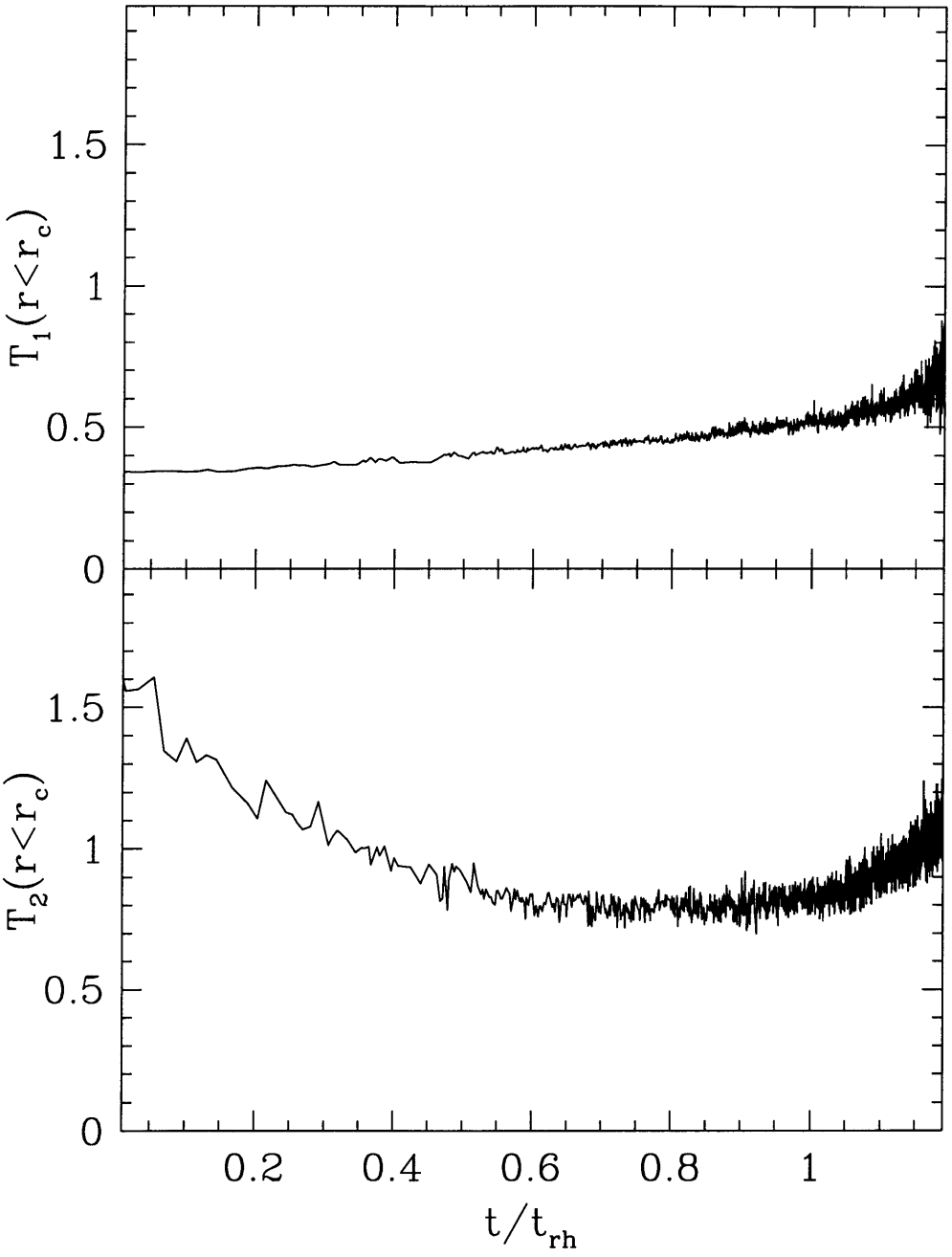

Figure 5-2: Evolution of the core temperature for the lighter stars ($T_1(r < r_c)$, top) and the heavier stars ($T_2(r < r_c)$, bottom) for the case $S = 1.24$ and $m_2/m_1 = 5.0$. (The ratio of these is shown in the bottom-most plot of Fig. 5-1.) Time is displayed in units of the initial half-mass relaxation time ($t_{\rm rh}$).

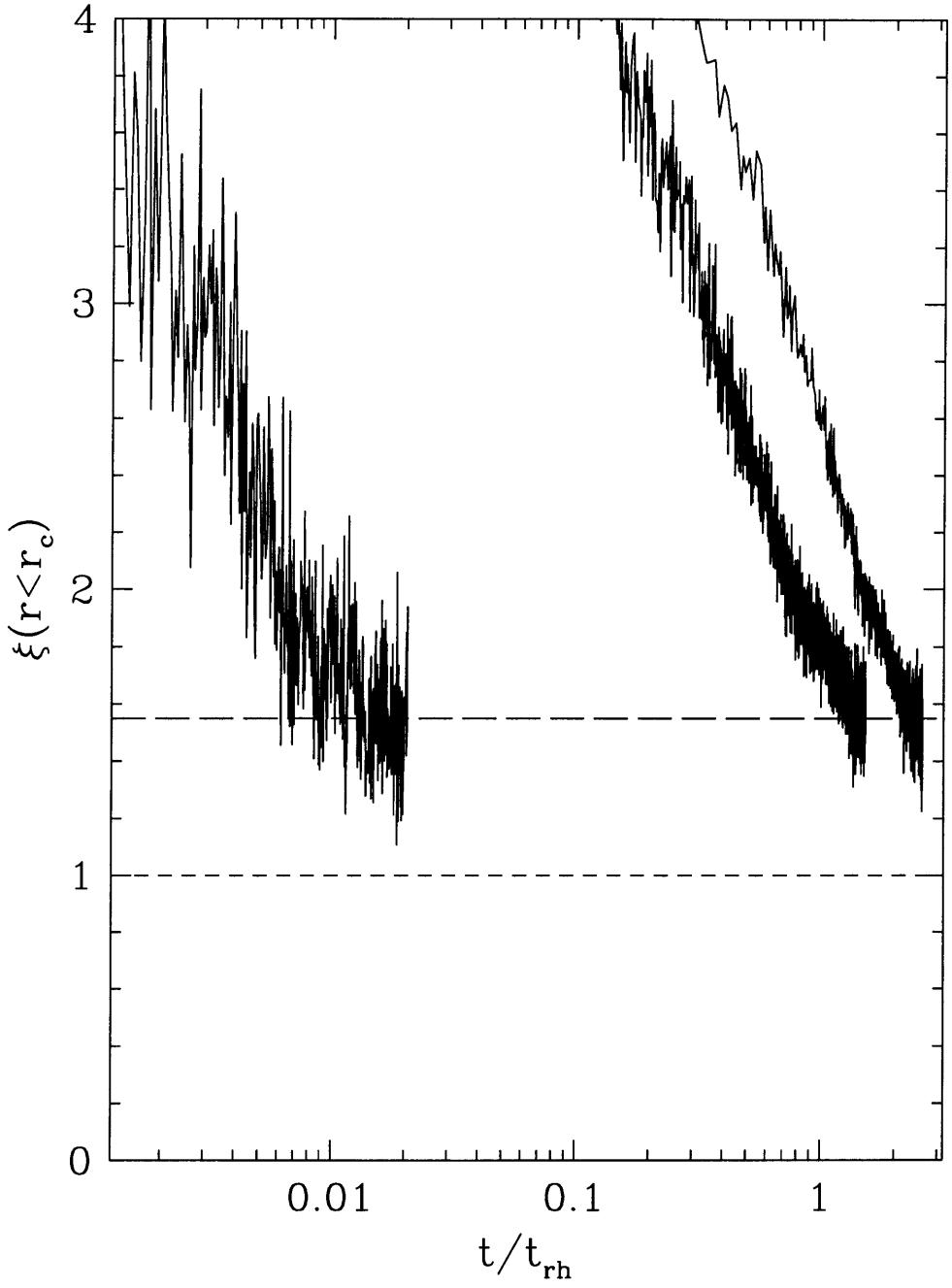

Figure 5-3: Evolution of the core temperature ratio for three calculations with different initial values of the dimensionless King model potential W_0, but all with $S = 1$ and $m_2/m_1 = 5$ ($M_2/M_1 \approx 0.09$). From left to right: $W_0 = 10$, $W_0 = 5$, and $W_0 = 1$. While the relaxation and core collapse times for these calculations span a wide range, in each case the temperature ratio reaches the same minimum value of approximately 1.55. The evolution is shown until shortly before core collapse in each case. Note that the logarithmic time scale has compressed the shapes of these curves, so that the leveling in the temperature ratio prior to core collapse is not as clearly apparent as in Fig. 1.

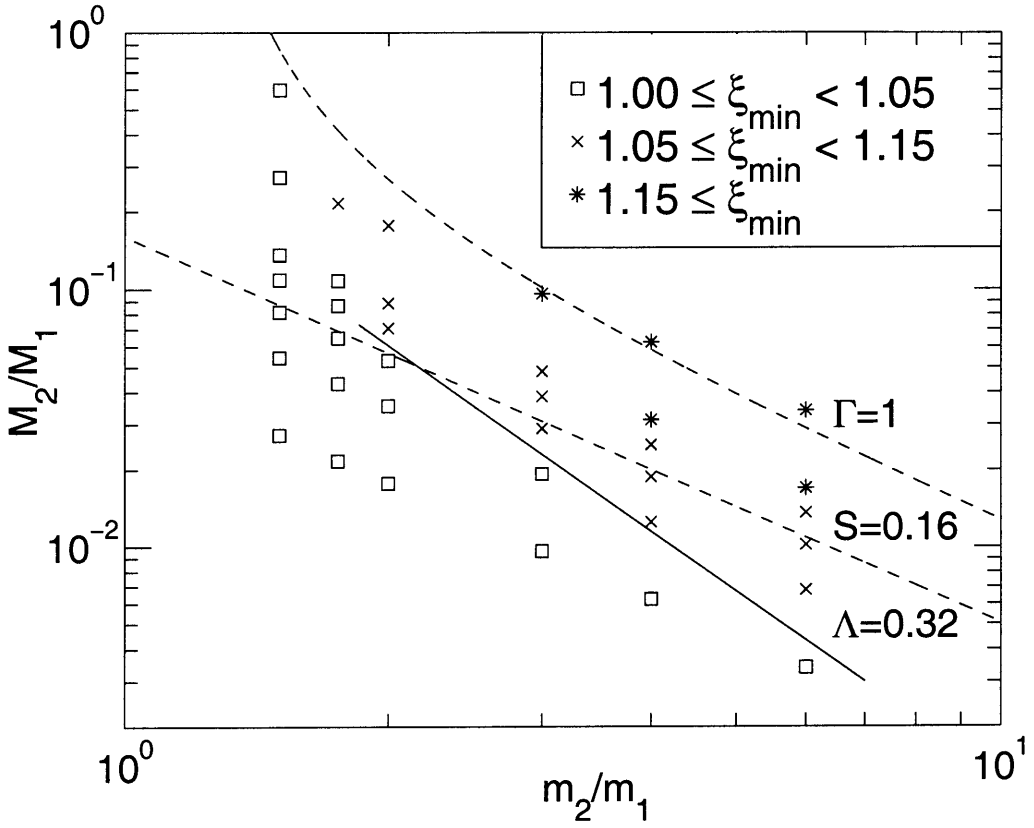

Figure 5-4: Minimum temperature ratio in the core for 30 calculations in set A, represented here using three symbols at points in the parameter space determined by M_2/M_1 and m_2/m_1. Also drawn are the Spitzer and Lightman-Fall stability boundaries ($S = 0.16$ and $\Gamma = 1$, respectively), and the boundary $\Lambda = 0.32$ suggested by these results (eq. [5.4]). Calculations marked with square are determined to have reached equipartition within our numerical accuracy.

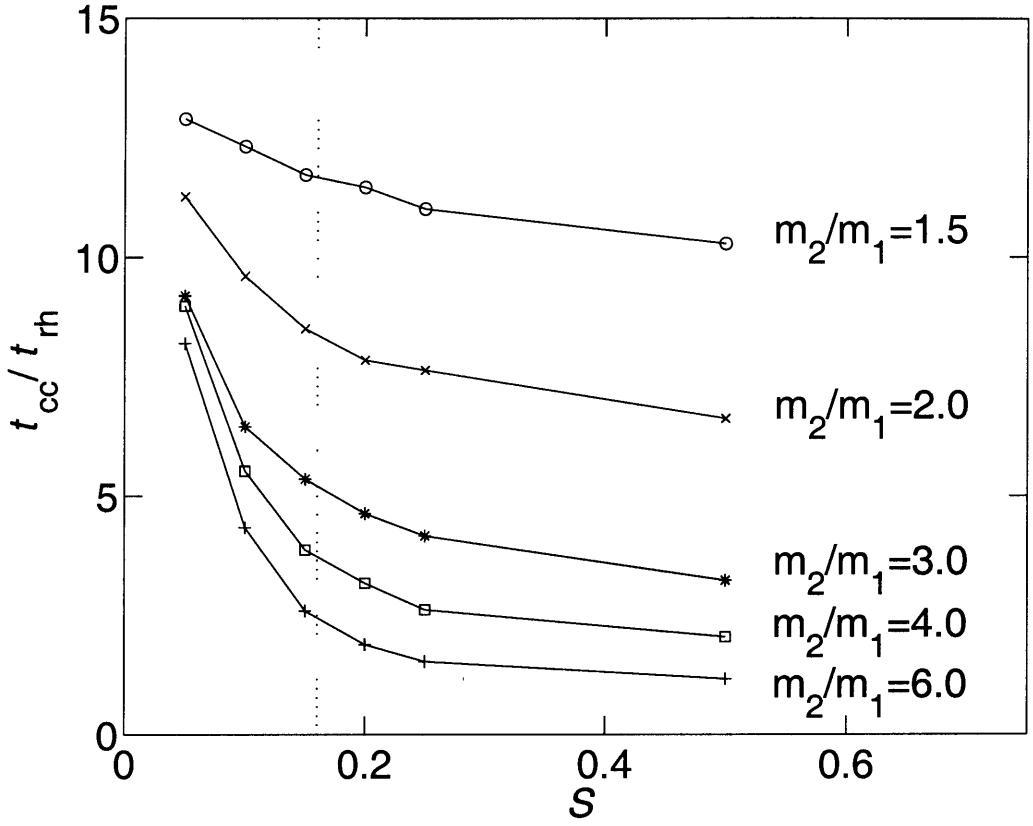

Figure 5-5: Core collapse times versus S for several values of m_2/m_1. The initial condition in each case was a two-component King model with $W_0 = 6$. The times are displayed in units of the initial half-mass relaxation time ($t_{\rm rh}$).

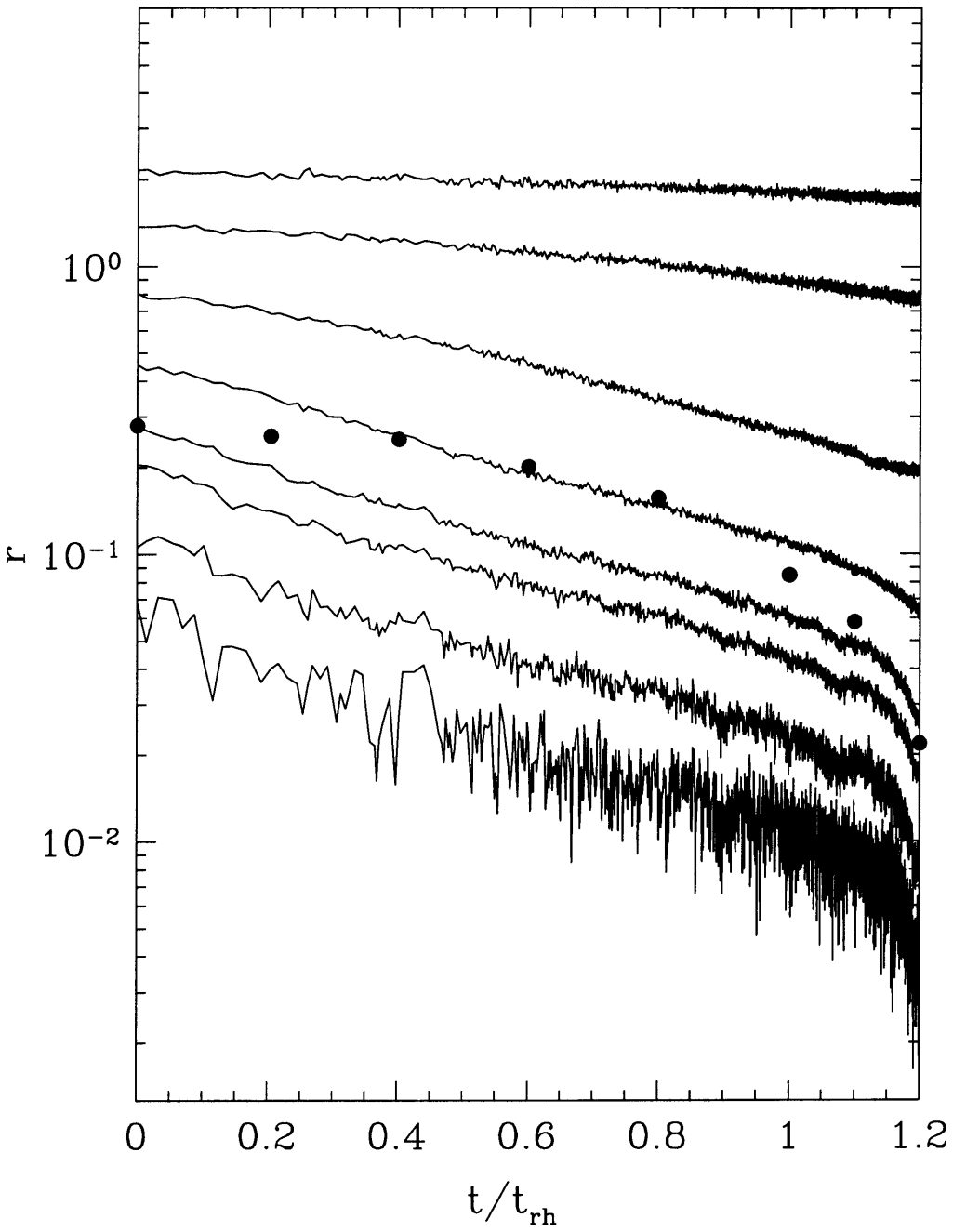

Figure 5-6: Eight Lagrange radii for the model with $S = 1.24$, $m_2/m_1 = 5$. From top to bottom: the radii containing 90%, 75%, 50%, 25%, 10%, 5%, 1%, and 0.1% of the total mass in the heavier component. Also drawn are several points in the evolution of the core radius (•). From this it is clear that many stars in the heavier component remain well outside of the core throughout the pre-collapse evolution.

5.3 Mass Segregation Timescales for High-Mass stars

Having examined the basic tendency of a cluster to evolve toward equipartition, we now undertake a more quantitative numerical study of the actual mass segregation timescales for heavy mass components in clusters. We do this by following the evolution of a small number (less than 1% of the total number of stars) of massive stars within a cluster. We study the effect of the density profile of the cluster on the mass segregation timescale, by using three different King models ($W_0 = 3$, 7, and 10) as the initial background cluster. In an effort to achieve energy equipartition with the rest of the cluster, a high-mass component steadily transfers energy to the lighter stars and in the process becomes increasingly concentrated in the inner regions of the cluster. In Figures 5-7-5-10, we show the evolution of the total number of high-mass stars remaining *outside* the half-mass radius as a function of time. The rate at which stars cross the half-mass radius is proportional to the relaxation time *and* the total number of stars remaining outside the half-mass radius. This leads to an exponential decrease in the number of stars outside the half-mass radius as $\sim e^{-t/\tau}$, with a characteristic e-folding time τ. Since the mass segregation is driven by the tendency of the system to move toward equipartition, we expect the mass segregation timescale to be the same as the equipartition timescale discussed in the previous section, $\tau \approx t_{\rm eq} \approx m_1/m_2$. Hence, the timescale τ can be obtained from our numerical simulations by fitting an exponential to our data. Since τ is proportional to the relaxation time (which changes as the cluster evolves), we obtain a good fit τ to the numerical data with a single exponential only in the early part of the evolution. This is because, as the relaxation time in the halo increases, the mass segregation timescale also gets longer, causing the $N_{r>r_h}$ to decrease at a slower rate. In each case, we find that our best-fit $\tau \approx 1/\mu$, in agreement with Spitzer's (1969) theoretical result.

In Figure 5-11, we show the best-fit mass-segregation timescale τ as a function of μ. We see that the mass segregation timescale scales roughly as $\tau = k/\mu$, with $k \simeq 1$ for $W_0 = 3$, $k \simeq 0.8$ for $W_0 = 7$, and $k \simeq 0.5$ for $W_0 = 10$. This is in good agreement

with the $1/\mu$ dependence obtained from theoretical studies (Spitzer 1987, 1968). We expect the constant k to be of order 1 in our calculations, since the evolution time in our simulations is always measured in units of the initial overall relaxation time. The small deviations of the value of k from 1 are most likely due to the varying background clusters used, in which the local relaxation time varies with radius to different extents. For example, in a low-concentration cluster, such as $W_0 = 3$, the relaxation time in the cluster does not vary significantly with distance from the center, and the ratio of the tidal radius to the core radius is small. Hence the overall relaxation time is a fairly good approximation of the local relaxation time within the cluster, giving a value of $k \simeq 1$. On the other hand, for a highly concentrated cluster like a $W_0 = 10$ King model, the ratio of the tidal radius to the core radius is much higher, and the overall relaxation time is in general an overestimate of the local relaxation time, except in the outer regions. Hence we would expect the value of k to be smaller. Thus in general we find that the mass segregation time $\tau \simeq (k/\mu)t_r$, where t_r is the relaxation time for the cluster.

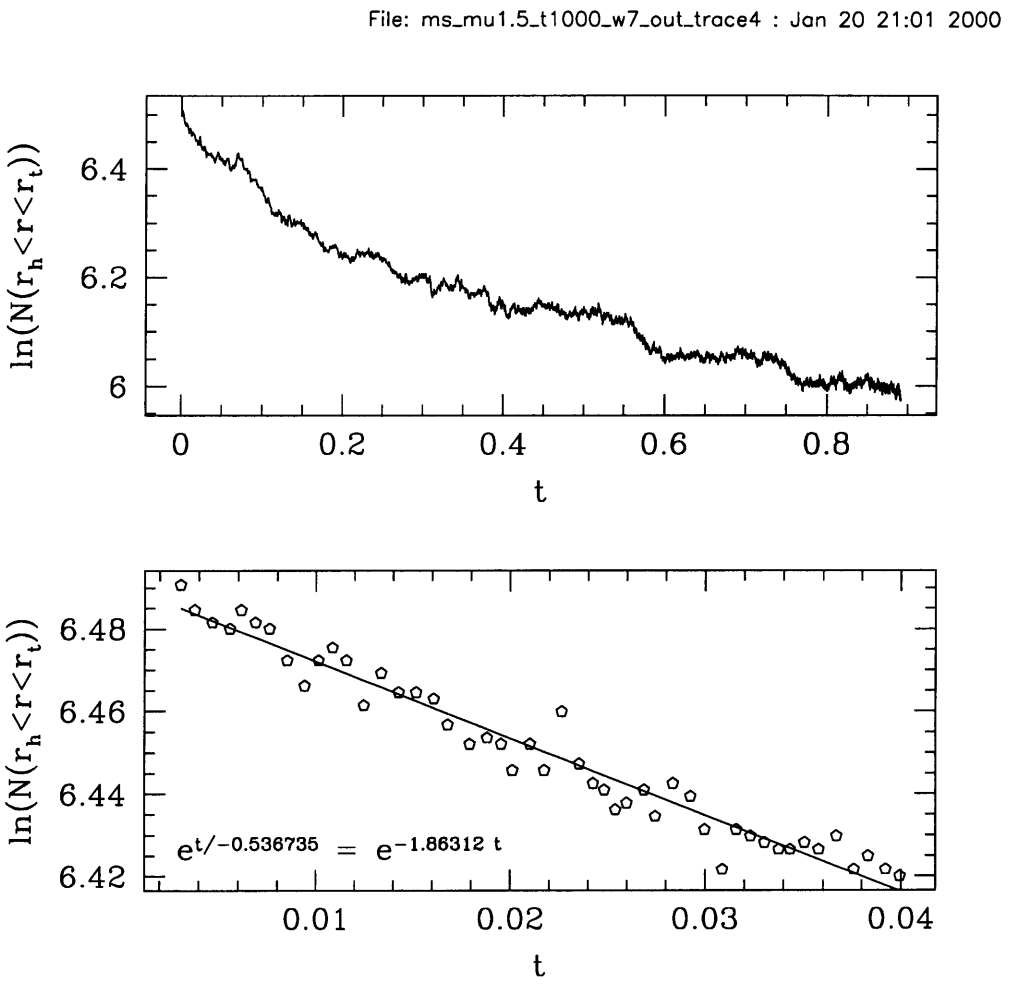

Figure 5-7: The evolution of the total number of heavy (trace) stars with $\mu = 1.5$ within the half-mass radius (top frame). The initial background cluster is a $W_0 = 7$ King model. The lower frame shows a fit to the numerical data for the early part of the evolution, in order to estimate the mass segregation timescale τ. We find that the timescale $\tau \simeq 1/1.8$, and scales roughly as $1/\mu$ (cf. Figs. 5-6, 5-7 and 5-8).

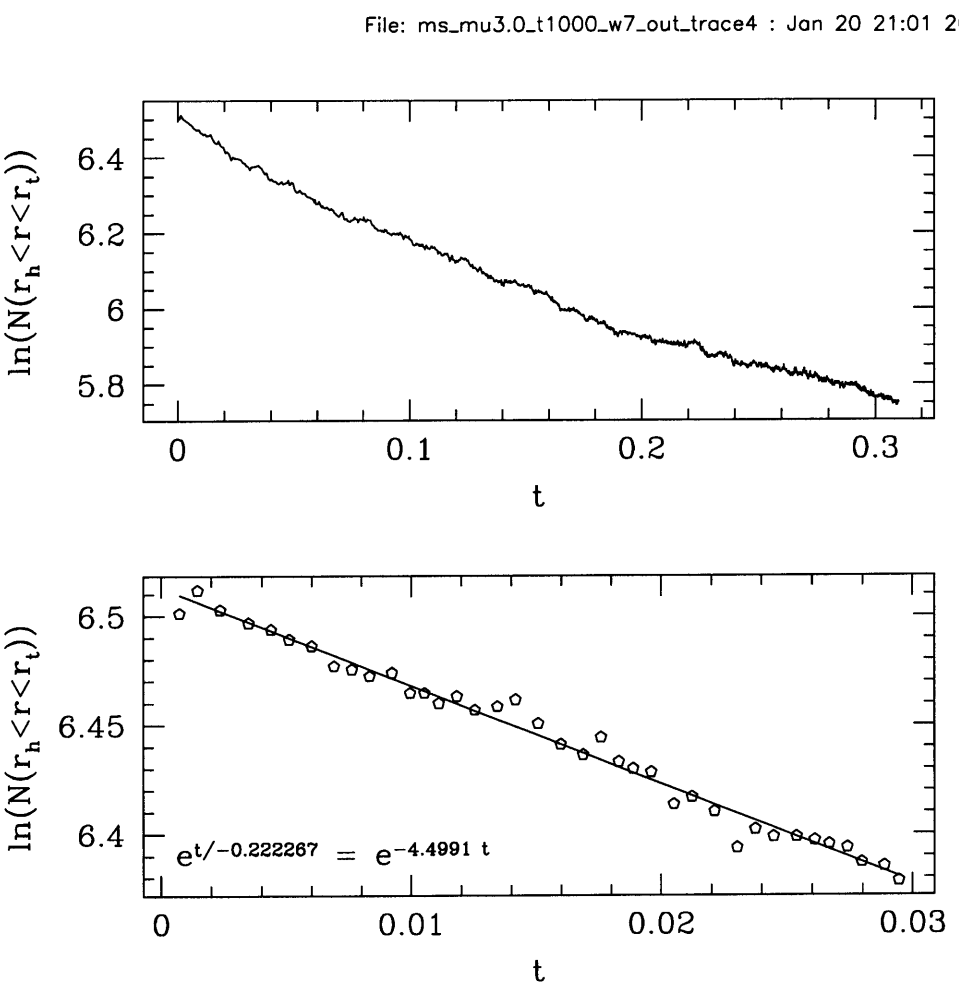

Figure 5-8: Same as Fig. 5-5, but with $\mu = 3$.

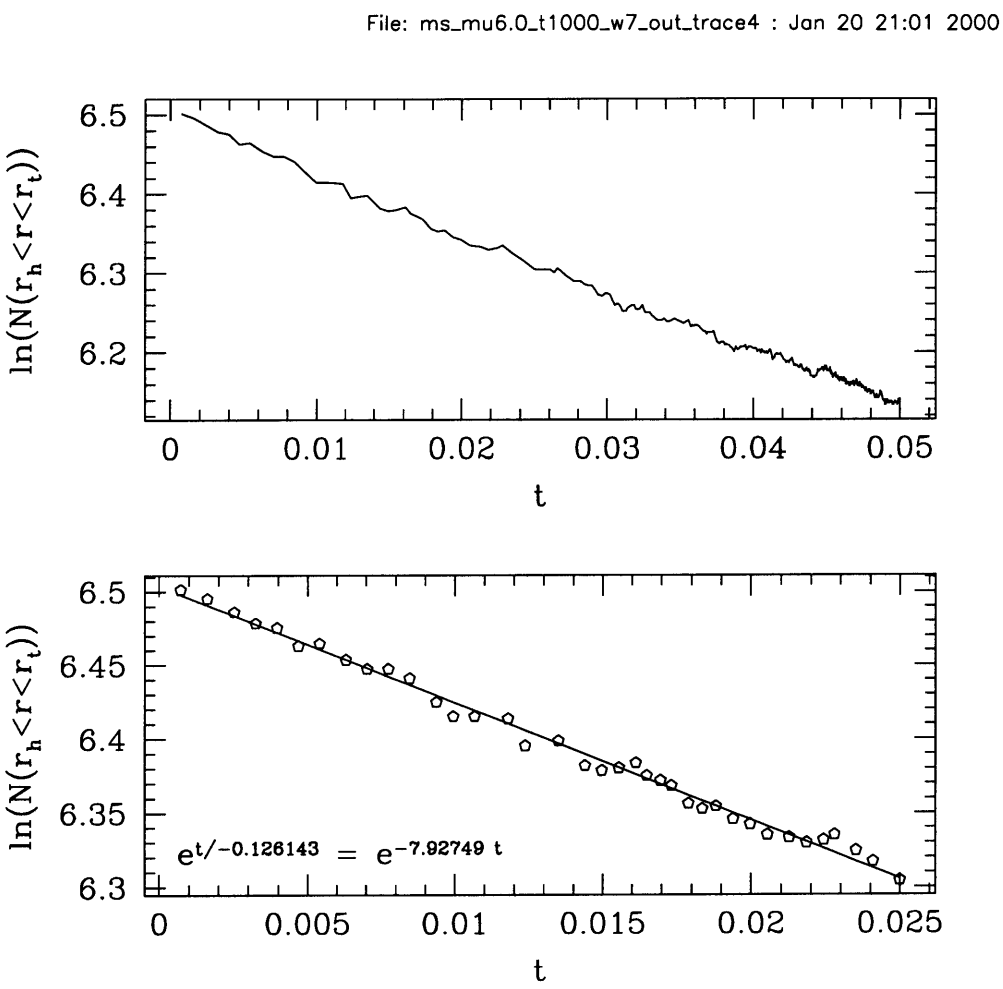

Figure 5-9: Same as Fig. 5-5, but with $\mu = 6$.

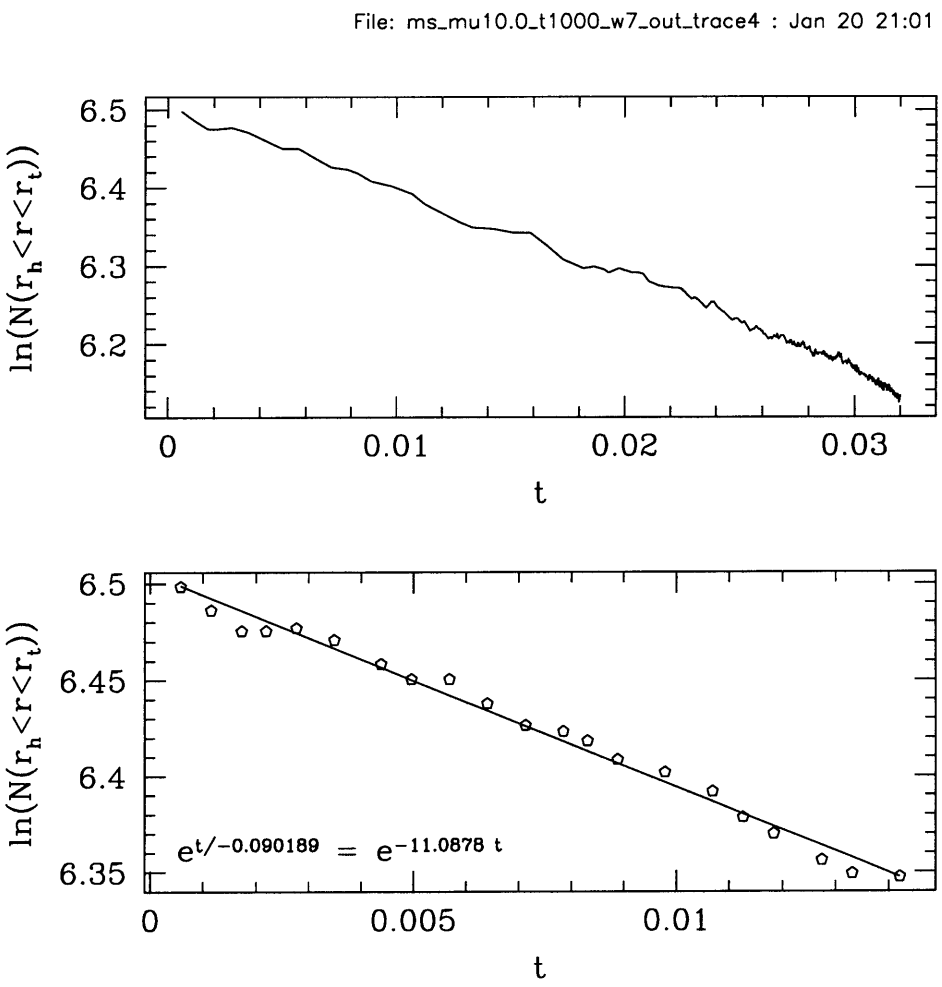

Figure 5-10: Same as Fig. 5-5, but with $\mu = 10$.

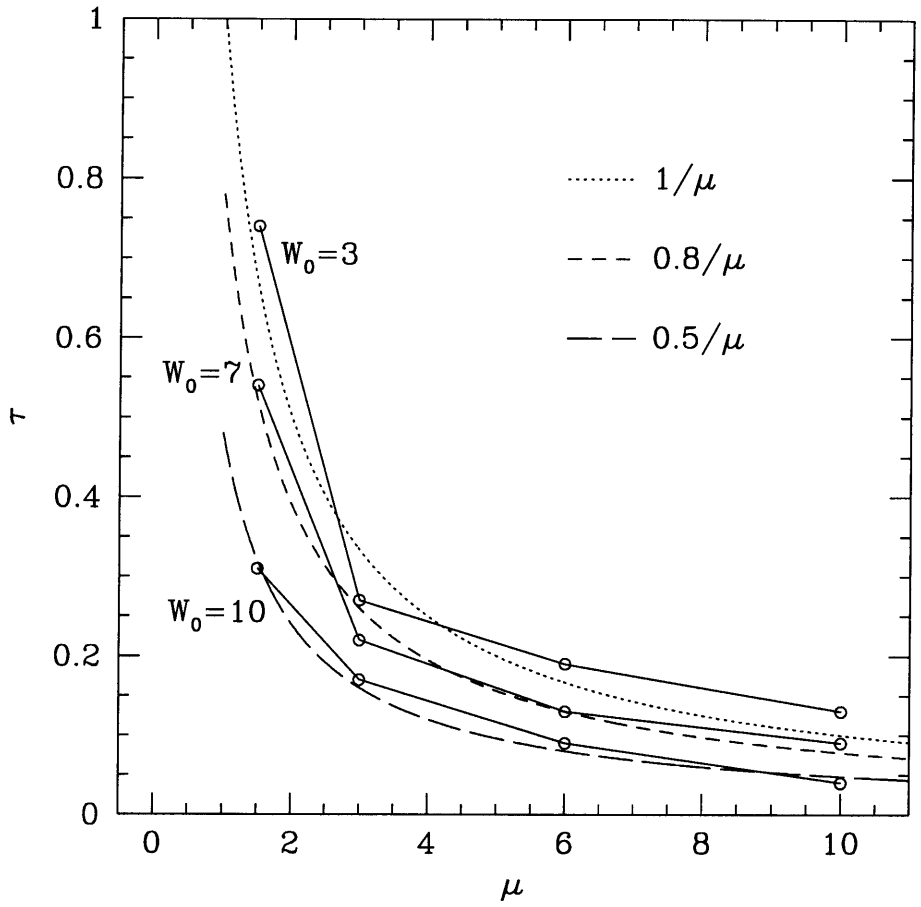

Figure 5-11: The best-fit mass-segregation timescale τ obtained from an exponential fit to the data. We see that the mass segregation timescale scales roughly as $\tau = k/\mu$, with $k \simeq 1$ for $W_0 = 3$, $k \simeq 0.8$ for $W_0 = 7$, and $k \simeq 0.5$ for $W_0 = 10$.

5.4 Millisecond Pulsars and Blue Stragglers in 47 Tuc

Recent observations by Camilo et al. (1999) and Freire et al. (1999) have now confirmed twenty millisecond radio pulsars in the globular cluster 47 Tuc. This is by far the largest sample of radio pulsars known in any globular cluster. These recent observations provide a unique opportunity to re-examine theoretically the formation and evolution of recycled pulsars in globular clusters. All pulsars are clearly recycled, with pulse periods $P \simeq 2 - 8\,\mathrm{ms}$. Accurate timing solutions, including positions in the cluster, are known for 14 of the pulsars. The pulsars can be divided into 3 groups: 7 are single; 8 are in short-period binaries with orbital periods $P_b < 0.5\,\mathrm{d}$; 5 are in wider binaries with $P_b > 1\,\mathrm{d}$ (see §3). The measured values of the period derivatives are probably all determined predominantly by the pulsar accelerations in the cluster potential (9 out of 14 pulsars have $\dot{P} < 0$). Under this assumption, Camilo et al. (1999) derive a central density $\rho_c \simeq 4 \times 10^5\,M_\odot\,\mathrm{pc}^{-3}$ using the method developed by Phinney (1993). This is somewhat larger than previous estimates (Pryor & Meylan 1993 give $\rho_c = 1.3 \times 10^5\,M_\odot\,\mathrm{pc}^{-3}$) (Rasio 2000).

The radial distribution of the pulsars appears surprising (Fig. 5-12) at first sight. Only 2 pulsars (47 Tuc O and L) are clearly inside the cluster core (assumed to have a radius $r_c = 12''$, from the latest determination by De Marchi et al. 1996 based on HST WF/PC images). One pulsar (47 Tuc F) is near the edge of the core in projection, and all others are in the region $r/r_c \simeq 1 - 6$ (the outermost, 47 Tuc C, has $r/r_c = 5.6$). No pulsar is detected in the region $r/r_c \simeq 6 - 35$, even though this region is well covered by the Parkes beam (with a half-power diameter of about 14 at 20 cm).

The roughly flat histogram in r (Fig. 5-12) suggests a deprojected 3D number density of pulsars $n(r) \propto r^{-2}$ out to $r \simeq 6\,r_c$, while the absence of pulsars outside that region indicates a much steeper density profile for $r > 6\,r_c$. This is actually consistent with a thermally relaxed radial distribution in the cluster, not too different from that of other stellar components such as red giants (Fig. 5-13). This is to be expected since the central relaxation time in 47 Tuc, $t_{rc} \sim 10^8\,\mathrm{yr}$, is much shorter than typical

characteristic ages of millisecond pulsars ($t_c \gtrsim 10^9$ yr). A very similar type of radial distribution has been observed for the 7 single millisecond pulsars near the center of M15 (see Phinney 1993 for a detailed theoretical analysis).

In a thermally relaxed stellar system, equipartition of energy leads to a more centrally concentrated spatial distribution for more massive stars. Since the main-sequence turnoff mass in the cluster ($m_{to} \simeq 0.85\,M_\odot$ for 47 Tuc) is a factor of $\sim 1.5 - 2$ lower than the masses of neutron star systems (including the companion masses for binaries), we would expect the radial distribution of pulsars to be more centrally concentrated than that of giants. This can be seen most convincingly by comparing integrated surface density profiles (Fig. 5-14). HST observations of the central region of 47 Tuc have revealed a large number of centrally concentrated, bright blue stragglers (Paresce et al. 1991; Guhathakurta et al. 1992), which are thought to be formed through collisions and mergers of main-sequence stars in the dense cluster core (Lombardi et al. 1996; Sills et al. 1999). These blue stragglers are main-sequence stars well above the turnoff, with theoretically derived masses in the range $m_{bs} \simeq 1.4 - 1.7\,M_\odot$ (one has a directly measured mass of $1.7 \pm 0.4\,M_\odot$; see Shara et al. 1997), i.e., very similar to the masses of neutron star systems. Indeed, we see in Figure 5-14 that the radial distributions of blue stragglers and millisecond pulsars in 47 Tuc appear strikingly similar (Rasio 2000).

In order to provide a theoretical understanding of the observed distribution of millisecond pulsars and blue stragglers, we have used a simple two component model to study the rate of mass segregation and the expected distribution of a heavy component (corresponding to neutron stars and blue stragglers). We begin with a two component King model ($W_0 = 7$), with $m_1 = 0.9\mathrm{M}_\odot$ and $m_2 = 1.4\mathrm{M}_\odot$. After trying several models with neutron star fractions varying from 1% to 10% by number in the cluster, we find that the models that most closely match the observed distribution are those with 5% neutron stars (by number). In figure 5-15, we show the distribution of millisecond pulsars, blue stragglers, and red giants in 47 Tuc, from actual observations (histograms), along with the distributions of red giants and neutron stars (NS) in our model cluster. The dotted line again shows the best-fitting modified Hubble law for

the distribution of red giants, while the solid line shows the distribution of giants in our model. The second solid line shows the distribution of neutron stars in our model cluster. The neutron star distribution in the model cluster seems to resemble the actual distribution of millisecond pulsars and blue stragglers in 47 Tuc reasonably in the inner regions. But outside of a few core radii, we do not see the steep rise in the NS distribution in our model to match the observed millisecond pulsar distribution. The distributions have all been normalized at 35 core radii in order to allow comparison. As expected, we see that the neutron star distribution is more centrally concentrated compared to the giants. The poor agreement of the neutron star distribution beyond a few core radii is characteristic of all the models we have tried. This problem has also been encountered in similar attempts to create theoretical models of the pulsars in M15 (Phinney 1993), where the pulsar distribution again has a steep outer edge, which has been difficult to understand theoretically. This suggests that besides mass segregation, there must be another mechanism, which we do not understand theoretically, that accounts for the peculiar distribution of millisecond pulsars.

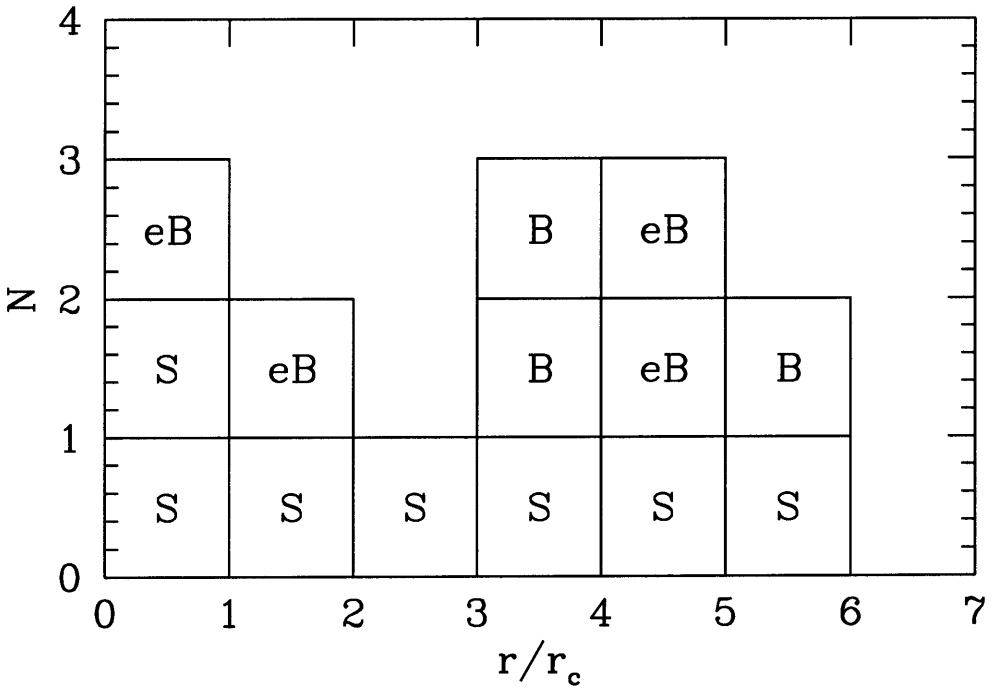

Figure 5-12: Projected radial distribution of the 47 Tuc pulsars. The histogram of the number of pulsars in each radial bin is shown (Rasio 2000). The radius (distance to the cluster center) is given in units of the core radius $r_c = 12''$ (from the HST WF/PC images of De Marchi et al. 1996). The labels have the following meaning: S denotes a single pulsar, eB an "eclipsing binary" ($P_b < 1\,\mathrm{d}$), and B a "normal binary" ($P_b > 1\,\mathrm{d}$).

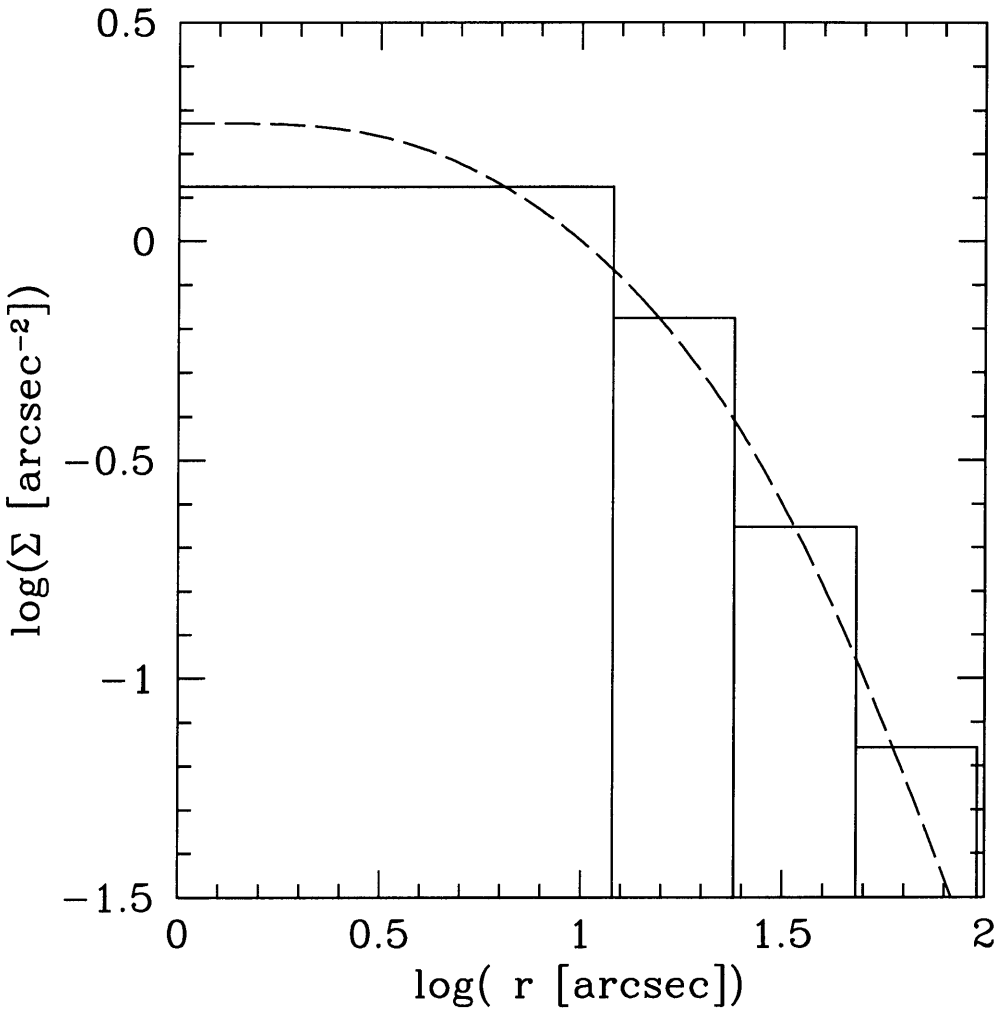

Figure 5-13: The surface density of pulsars (histogram) is compared to that of giants (dashed line; from Fig. 2 of De Marchi et al. 1996). Pulsars were grouped into one core bin ($r/r_c = 0 - 1$) and 3 logarithmically spaced outer bins ($r/r_c = 1 - 2$, $2 - 4$, and $4 - 8$). The surface density of pulsars was rescaled to match that of giants at $\log(r[farcs]) = 1.55$ (center of the third bin).

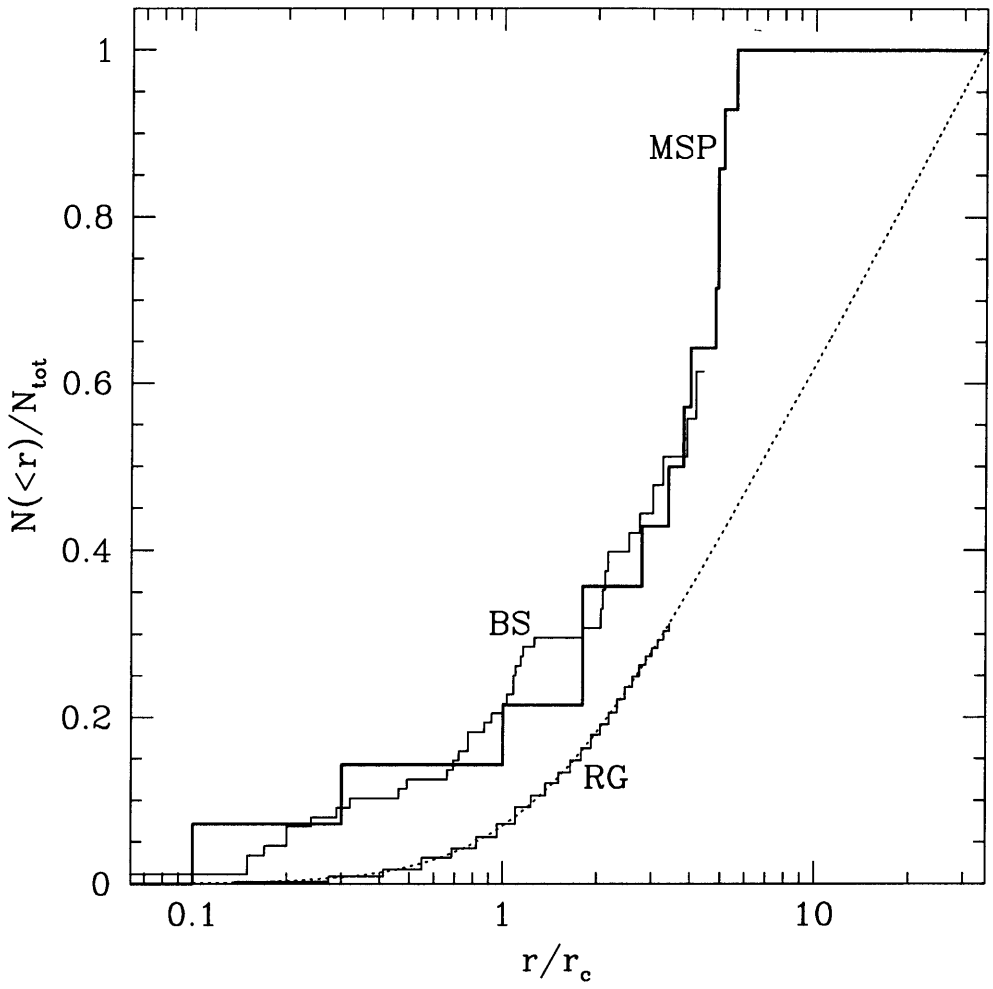

Figure 5-14: Cumulative radial distribution of the 47 Tuc pulsars (MSP, thick histogram), compared to that of red giants (RG) and blue stragglers (BS). The RG distribution was calculated by integrating the surface density profile given in Table 1 of De Marchi et al. (1996). The dotted line is the best fit to a modified Hubble law (which is analytic and closely approximates the inner regions of high-concentration King models; see, e.g., Binney & Tremaine 1987), extended to $r = 35\,r_c$ (near the edge the Parkes beam at 20 cm). Note that fitting the cumulative distribution leads to a tighter constraint on r_c than fitting the surface density (as done by De Marchi et al.). The best-fit model shown here gives a core radius about 30% larger than that quoted by De Marchi et al. (although we still give r in units of $r_c = 1\farcs2$, as in Fig. 1). The BS distribution was obtained by combining the data sets of Paresce et al. (1991, HST FOC) and Guhathakurta et al. (1992, HST PC). Star HST-12 of Paresce et al. was adopted as the cluster center. The surface density at $r \gtrsim 2\,r_c$ was corrected for incomplete radial annuli in the HST PC image (as in De Marchi et al. 1996). The BS distribution was normalized to match that of the millisecond pulsars at $r \simeq 4.2\,r_c$ (extent of the HST PC image).

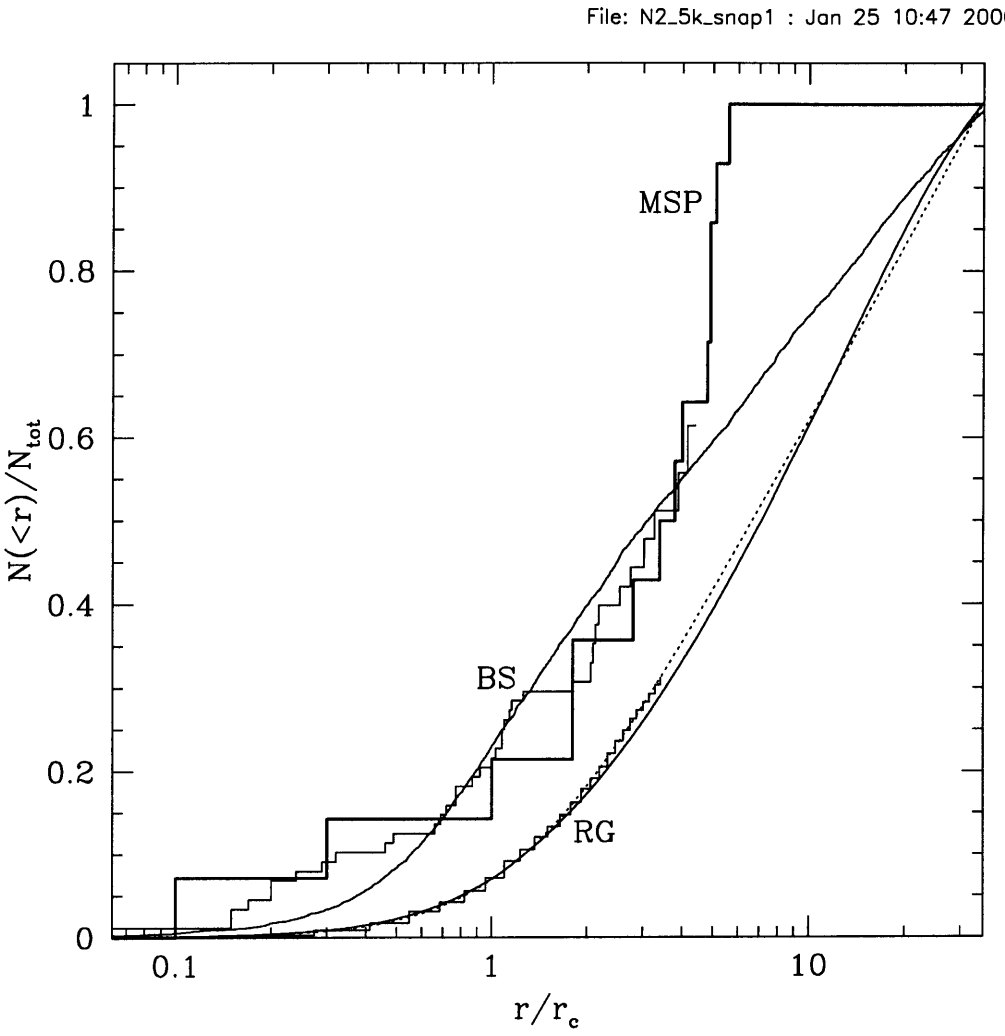

Figure 5-15: Distribution of millisecond pulsars, blue stragglers, and red giants in 47 Tuc, from actual observations (histograms). Also shown are the distributions of red giants and neutron stars (NS) in our model cluster. The dotted line shows the best-fitting modified Hubble law for the distribution of red giants, while the solid line shows the distribution of giants in our model. The second solid line shows the distribution of neutron stars in our model cluster. The neutron star distribution in the model cluster seems to resemble the actual distribution of millisecond pulsars and blue stragglers in 47 Tuc quite well in the inner regions. But outside of a few core radii, we do not see the steep cut-off in the NS distribution in our model to match the observed millisecond pulsar distribution. The distributions have all been normalized at 35 core radii in order to allow comparison.

5.5 Evolution of Low-Mass stars

We turn our attention to the evolution very-low-mass objects ($0.001\mathrm{M}_\odot \lesssim m \lesssim 0.1\mathrm{M}_\odot$) in clusters. Just as equipartition tends to concentrate stars that are heavier than the mean mass to concentrate in the inner regions of the cluster, it also has the reverse effect on stars with masses below the mean mass, causing them to segregate *outward*, thereby depleting their numbers in the inner regions. A simple analysis shows that, for a cluster with two mass components of mass m_1 and $m_2 < m_1$, as the two components approach equipartition on the equipartition timescale, the ratio of their velocities $\langle v_2^2 \rangle / \langle v_1^2 \rangle$ approaches $1/\mu$, where $\mu \equiv m_2/m_1$. Hence, if the mass ratio μ is small enough, the mean velocity of the lighter component could become greater than the escape velocity from the cluster, causing most (or all) of the lighter stars to evaporate from the cluster. For example, in a cluster with $< v_1 > \sim 10\,\mathrm{km\,s^{-1}}$ and $v_{esc} \sim 50\,\mathrm{km\,s^{-1}}$ the mean velocity of a light component with $m_2/m_1 \sim 0.01$ would be $< v_2 > \sim 100$, which might cause the light component to evaporate from the cluster on the relaxation timescale. This simple analysis suggests that clusters should lose all stars below a certain cut-off mass $\lesssim 0.01\mathrm{M}_\odot$ (depending on the mean mass in the cluster, and the average velocity dispersion) in a few relaxation times. However, the local relaxation time can vary by more than an order of magnitude within a cluster. Hence the time required to reach equipartition can be much longer in the halo, compared to that in the core. This leads to the possibility that even though the central regions of the cluster may be depleted of light stars very quickly, the lighter stars could still be retained in the cluster for a much longer time in an extended halo. We test this hypothesis by examining the evolution of a population of low-mass trace stars in an evolving background cluster.

In Figure 1, we show the evolution of the total number of low-mass (trace) stars contained within the core, the half-mass radius, and the tidal radius, for three different mass ratios $\mu = 0.1$, 0.01, and 0.001. We start with an initial King model with $W_0 = 7$. In Figures 2 and 3, we show similar results for an initial King model with $W_0 = 3$ and $W_0 = 1$, respectively. For $W_0 = 7$, the initial cluster has a high central concentration,

and hence is closer to core collapse. This results in relatively little *overall* tidal mass loss from the cluster. Hence, although we see the lighter stars being depleted from the core very quickly, a substantial fraction still remain within the tidal boundary of the cluster. Since the relaxation time in the halo is much longer, the lighter stars do not completely evaporate from the cluster, but instead a significant fraction accumulate in the outer halo. For $\mu = 0.1$, The number of trace stars within the half-mass radius drops from an initial value of $\simeq 300$ to only $\simeq 40$ at core collapse. In contrast, the *total* number of light stars within the cluster only decreases from its initial value of 1000 to about 700 (i.e., only 30% of the light stars completely escape from the cluster). The depletion of the light component from within the half-mass radius and the core is greater for $\mu = 0.01$ and 0.001. But in all cases, only about 30% of the light stars escape from the cluster. This is consistent with the overall escape rate from a tidally truncated $W_0 = 7$ King model, in which only 15% of the stars are lost up to core collapse (see chapter 3). As expected, the lighter stars have an escape rate higher than that of the background cluster.

In Figure 2, we show the same results as in Figure 1, but for a less concentrated initial King model ($W_0 = 3$). Here, the overall escape rate for the entire cluster is high enough so that the tidal boundary shrinks significantly as the cluster evolves. This causes the lighter stars to be removed much more efficiently as they accumulate in the halo. The shrinking tidal boundary causes more than 90% of the light stars to be tidally stripped from the cluster. The number of stars remaining within the half-mass radius at core collapse is only about 5% of the initial number within that radius. In Figure 3, we show the results for an even less concentrated initial King model ($W_0 = 1$). Here, the overall escape rate for the entire cluster is even higher, causing more than 95% of the light stars to be lost from the cluster. The number of stars remaining within the half-mass radius at core collapse is only about 5% of the initial number within that radius.

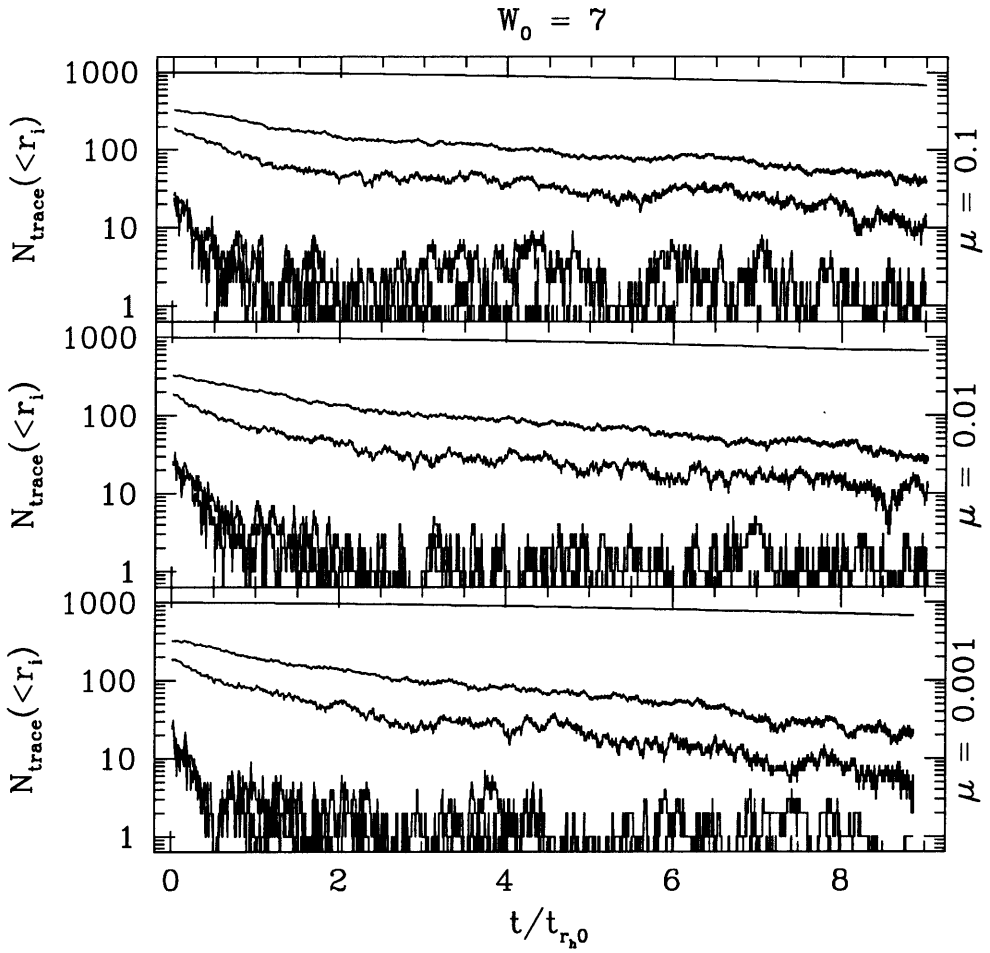

Figure 5-16: The evolution of the total number of light (trace) stars within five selected radii– the core radius (which get smaller as the cluster evolves), the *initial* core radius, the mean of the core radius and the half-mass radius, the initial half-mass radius, and the tidal radius of the cluster. The three frames (from top to bottom) show the results for $\mu = 0.1$, 0.01, and 0.001 respectively. In each case, the initial background cluster was a $W_0 = 7$ King model.

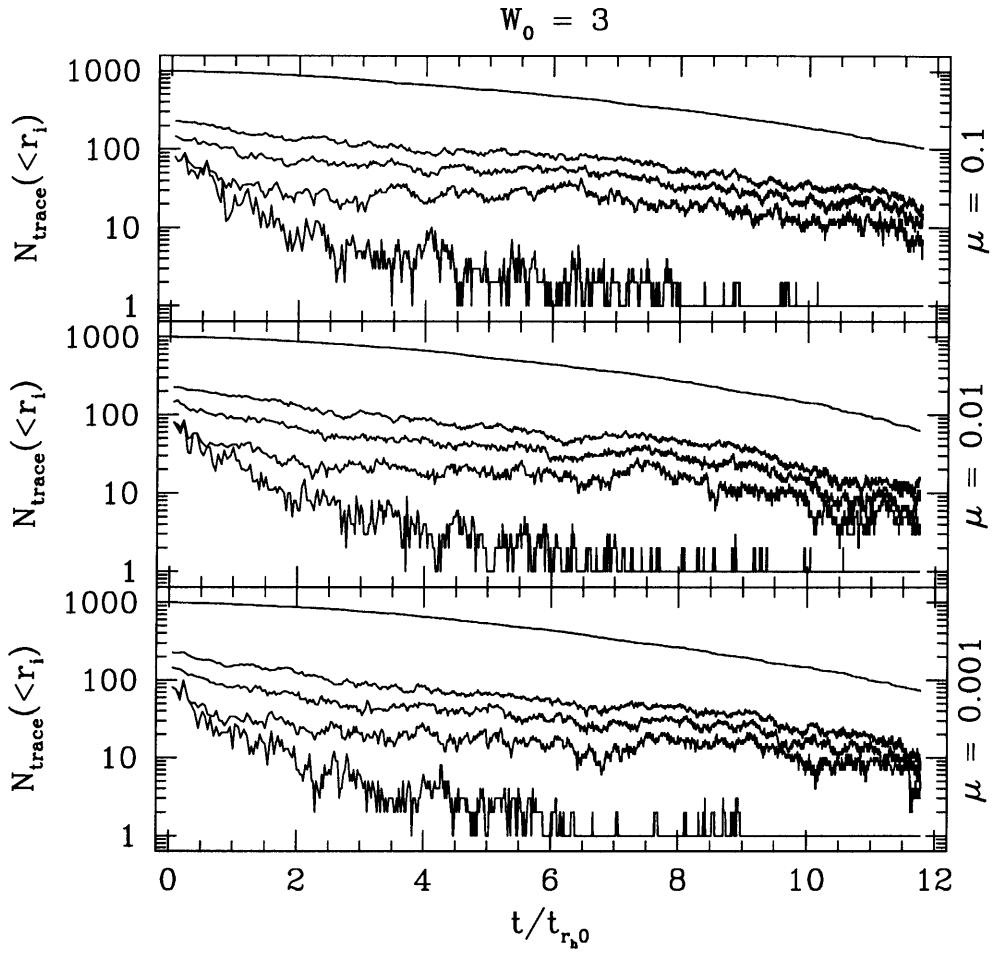

Figure 5-17: Same as Fig. 5-16, but with a $W_0 = 3$ initial King model.

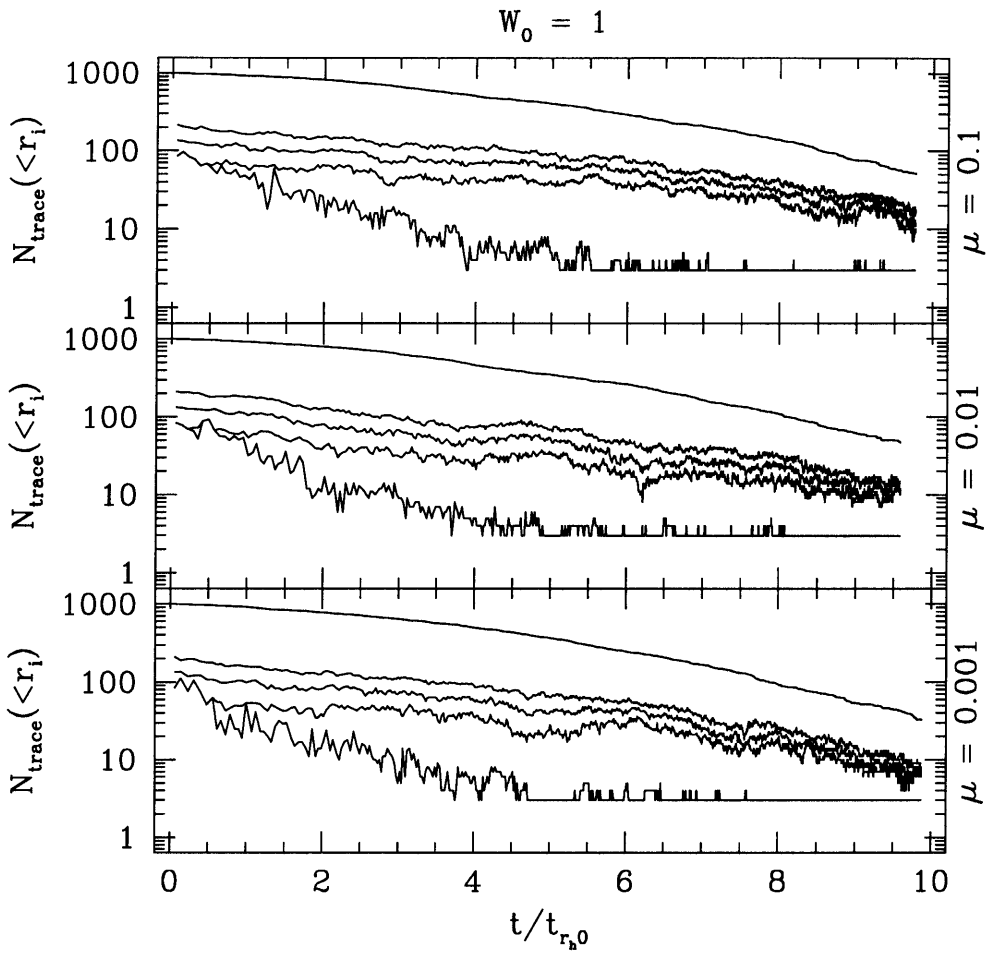

Figure 5-18: Same as Fig. 5-16, but with a $W_0 = 1$ initial King model.

In Figure 4, we show a comparison of the time required for 80% of the initial number of stars within the half-mass radius to drift beyond the half-mass radius. The timescales are given in units of the initial half-mass relaxation time in the cluster. We recall from the results of chapter 3, that the evolution of tidally truncated King models is slowest i.e., the core-collapse time is longest for $W_0 \simeq 5$. That effect is also reflected here in the mass segregation timescales, giving a longer timescale for the $W_0 = 3$ models, compared to $W_0 = 1$ and 7. We also see that the dependence of the timescale on μ gets weaker for $\mu \lesssim 0.01$.

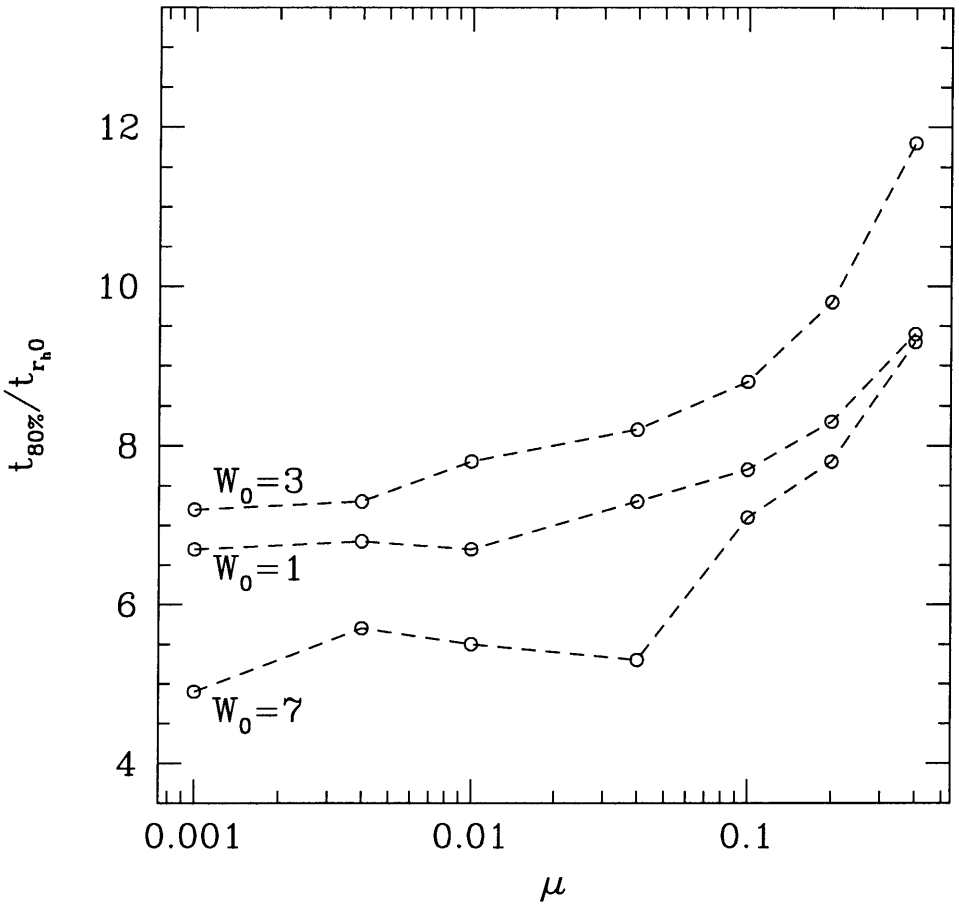

Figure 5-19: The time required for 80% of the initial number of stars within the half-mass radius to drift beyond the half-mass radius.

5.6 Summary

Although we have omitted the effects of binaries (which have been shown to retard the onset of core collapse) and also stellar evolution (which can have important implications for the early evolution) in our study of timescales for equipartition and mass segregation, the following observations and conclusions seem justified. (a) For some clusters the core temperature ratio becomes constant over some fraction of the evolution at a minimum value greater than one, in agreement with previous results obtained using other methods. (b) The departure from equipartition calculated for a range of individual and total mass ratios approximately respects the theoretical predictions of Spitzer (1969) and Lightman & Fall (1978). The agreement with Spitzer is reasonable for clusters with $m_2/m_1 \geq 2$, and the Lightman-Fall stability boundary ($\Gamma = 1$) appears to reflect the shape of regions of constant $\xi_{\rm min}$ in the parameter space determined by M_2/M_1 and m_2/m_1, although it lies well inside the region occupied by clusters for which equipartition is clearly not attained. A more accurate boundary that is suggested by our results is given by equation (5.4). (c) Stars in the heavier component do not immediately fall into the center as assumed by Spitzer in his analysis, and instead many remain outside the core throughout the evolution. (d) The approach to equipartition within the half-mass radius appears to occur on the time scale $2t_{\rm eq}$, as suggested by Spitzer (1969; see eq. (5.5)). (e) A core temperature ratio of m_2/m_1 appears to be a robust quantity for equilibrium models with a relatively shallow potential, in agreement with previous results obtained using other methods. For massive stars with $\mu \gtrsim 2$, we find that in agreement with theoretical results, the mass segregation timescale τ varies roughly as k/μ, with $k \lesssim 1$ for clusters with different central concentrations.

We have attempted to explain the observed distribution of neutron stars and blue stragglers in 47 Tuc using a simplified two-component theoretical model. The comparison of our model to the observed distributions indicates that although the relatively higher central concentration of millisecond pulsars and blue stragglers can be explained quite easily, the outer steep edge of the millisecond pulsar distribution

remains difficult to reconcile with our theoretical models.

Our results clearly indicate that it is possible to retain large numbers of very light $m < 0.1\mathrm{M}_{\odot}$ stars in the halos of globular clusters. This is contrary to the common belief that globular clusters are devoid of very low-mass objects. We find that the rate of mass loss for low-mass objects strongly depends on the evolutionary state of the cluster, and size of the strength of the Galactic tidal field. Clusters with a relatively high initial central concentration ($W_0 \gtrsim 7$) can retain over 70% of the low-mass stars in their outer halos, even after they lose more than 90% of the low-mass stars from within the half-mass radius. Occasional perturbations of these objects through strong interactions could also cause them to reenter the inner regions of the cluster as high velocity objects with predominantly radial orbits. Our results strongly suggest that the halos of even highly evolved clusters could be rich in low-mass stars, white dwarfs, brown dwarfs, and even planet-mass objects. The fact that these objects tend to accumulate in the least crowded regions of a cluster would make searches more efficient and easier to undertake. Unfortunately, low-mass objects in clusters have always been, and will continue to be difficult to observe directly due to their low luminosities. However, studies have shown that such objects might be observable during rare gravitational micro-lensing events, in which the low-mass object acts as foreground gravitational lens for a more distant background star. Hence searches for such gravitational micro-lensing events due to low-mass objects, especially in the outer regions of globular clusters may present new and unique opportunities for observing very-low-mass objects.

Chapter 6

Binary Interactions

6.1 Introduction

The realization over the last 10 years that primordial binaries are present in globular clusters in dynamically significant numbers has completely changed our theoretical perspective on these systems (see. e.g., the review by Hut et al. 1992). Most importantly, dynamical interactions between hard primordial binaries and other single stars or binaries are now thought to be the primary mechanism for supporting a globular cluster against core collapse (McMillan, Hut, & Makino 1990, 1991; Gao et al. 1991). In addition, exchange interactions between primordial binaries and compact objects can explain very naturally the formation of large numbers of X-ray binaries and recycled pulsars in globular cluster cores (Sigurdsson & Phinney 1995; Davies & Hansen 1998; Portegies Zwart et al. 1997). Previously, it was thought that primordial binaries were essentially nonexistent in globular clusters, and so other mechanisms such as tidal capture and three-body encounters had to be invoked in order to form binaries dynamically during core collapse. However, these other mechanisms have some serious problems, and are much more likely to result in mergers than in the formation of long-lived binaries (Chernoff 1996; Kochanek 1992; Kumar & Goodman 1996).

Hubble Space Telescope observations have provided direct constraints on primordial binary fractions in clusters. The binary fraction is a key input parameter for any realistic study of cluster dynamics. For example, the recent observation of a broad-

ened main sequence in NGC 6752, based on HST PC images of its core, suggest that the binary fraction is probably in the range 15%–38% in the inner core (Rubenstein & Bailyn 1997).

Despite the fact that binaries play a crucial role in the late phases of evolution of a cluster, the overall evolution of a binary population within a cluster, and its direct implications for the formation rate of observable binaries and blue stragglers remains poorly understood. In addition, the relative importance of binaries in a cluster, like many other physical processes, may depend on the actual size (N) of the cluster. This makes it difficult to extend results obtained from smaller N-body simulations to realistic globular cluster models. When the initial primordial binary fraction is below a certain critical value, a globular cluster core can run out of binaries before the end of its lifetime, i.e., before being evaporated in the tidal field of the Galaxy (McMillan & Hut 1994). Without the support of binaries, the cluster will undergo a much deeper core collapse and so-called gravothermal oscillations (Sugimoto & Bettwieser 1983; Breeden et al. 1994; Makino 1996). At maximum contraction, the core density may increase by many orders of magnitude, leading to greatly enhanced interaction rates.

Dynamical interactions involving primordial binaries can result in dramatically increased collision rates in globular clusters. This is because the interactions are often *resonant*, with all the stars involved remaining together in a small volume for a long time ($\sim 10^2 - 10^3$ orbital times, Portegies Zwart et al. 1999). For example, in the case of an interaction between two typical hard binaries with semi-major axes ~ 1 AU containing $\sim 1\,M_\odot$ main-sequence (MS) stars, the effective cross-section for collision between any two of the four stars involved is essentially equal to the entire geometric cross-section of the binaries (Bacon, Sigurdsson & Davies 1996; Portegies Zwart et al. 1999; Leonard 1994). This implies a collision rate ~ 100 times larger than for single stars.

Direct observational evidence for stellar collisions and mergers in globular clusters comes from the detection of large numbers of blue stragglers concentrated in the dense cluster cores. All observations suggest that they must be formed through the merger of two lower-mass stars, but this can occur in two different ways: following

the physical collision of two single stars, or through the coalescence of the two components in a close binary system (Bailyn 1995; Leonard 1989; Livio 1993). Direct evidence for binary progenitors has been found in the form of contact (W UMa type) binaries among blue stragglers in low-density globular clusters such as NGC 5466 (Mateo et al. 1990) and M71 (Yan & Mateo 1994), as well as in open clusters (Jahn et al. 1995; Kałużny & Ruciński 1993; Milone & Latham 1994). At the same time, strong indication for a collisional origin comes from recent detections by HST of large numbers of blue stragglers concentrated in the cores of some of the densest clusters, such as M15 (De Marchi & Paresce 1994), M30 (Yanny et al. 1994; Guhathakurta et al. 1998), NGC 6397 (Burgarella et al. 1994), and NGC 6624 (Sosin & King 1995). Further support for a collisional origin comes from the apparent lack of binaries in these very dense environments (Rubenstein & Bailyn 1996; Shara et al. 1995). Most of our current knowledge about the properties of blue stragglers in dense cluster cores comes from high-resolution HST WFPC and FOC images (e.g., Bailyn 1995; Burgarella et al. 1995; Gilliland et al. 1995; Sosin & King 1995; Piotto et al. 1999). The observed properties include numbers of blue stragglers in various clusters, colors and luminosities, photometric variability, central concentration in the cluster, all of which place strong constraints on theoretical models.

Other observational signatures of collisions or strong tidal interactions come from the existence of extended blue horizontal branches (HB) in high-central-density clusters such as NGC 6388 and NGC 6441 (Rich et al. 1997). Collisions or strong tidal interactions involving giants can lead to loss of envelope mass and therefore populate the blue side of the HB. Complete stripping of red-giant envelopes in collisions could lead to the formation of a population of young, low-mass white dwarfs with properties similar to those of a new class of blue stars discovered in recent HST FOS observations of the post-core-collapse cluster NGC 6397 (Edmonds et al. 1997).

While the high-luminosity X-ray sources in globular clusters have been identified clearly as accreting neutron stars in low-mass X-ray binaries (LMXBs; see, e.g., Lewin et al. 1993), the nature of the low-luminosity sources ($L_X \lesssim 10^{35}\,\mathrm{erg\,s^{-1}}$) — discovered by *Einstein* and further studied with ROSAT — remains controversial. Proposals

include cataclysmic variables (CVs; cf. Hertz & Grindlay 1983), LMXBs — either in quiescence (Verbunt et al. 1984) or viewed at high inclination (White & Mason 1985) — millisecond pulsars (Danner et al. 1994), and RS CVn systems (magnetically active, moderately evolved stars in a short-period binary; cf. Bailyn et al. 1990).

HST observations of the low-luminosity X-ray sources in NGC 6397 have provided several optical counterparts, with now four clearly identified CVs (Cool et al. 1995; Edmonds et al. 1997). Optical and UV observations of other clusters with HST have revealed interesting objects in the cluster cores that may be counterparts to low-luminosity X-ray sources (e.g., Ferraro et al. 1997b; Geffert et al. 1997). Unfortunately, the cluster cores are very crowded and the limited pointing accuracy of ROSAT ($\sim$ 5 arcsec) makes association of the optical/UV objects with the X-ray sources rather uncertain. AXAF provides an unprecedented opportunity to study the population of faint X-ray sources as a group, and to search globular clusters at lower luminosities for quiescent LMXBs, CVs, RS CVn systems, millisecond pulsars, and other binary systems. The ACIS CCDs have a sensitivity $\sim$ 10 times that of the ROSAT HRI for the soft ($T = 1 - 3$ keV) spectra of these sources, and AXAF also provides $\sim$ 10 times better spatial resolution, making it possible for the first time to resolve the cores of most Galactic globular clusters and to determine positions with an accuracy enabling optical follow-up. These observations are sure to provide many new constraints on theoretical models of globular clusters, and will allow us to make our simulations more realistic.

Previous studies of globular cluster evolution have mostly focused on binary interactions during deep core collapse, and the subsequent rebound of the core, leading to gravothermal oscillations (Makino 1996; Drukier et al. 1999). In these studies, binaries are allowed to form only during the late stages of core collapse through three-body interactions. Although the rate of three-body binary formation has been estimated analytically, the fundamental process of forming a binary through a three-body interaction is quite complex, and accurate cross sections are difficult to obtain, especially when stars of unequal masses are involved. The other mechanism which is often invoked to allow binary formation during core collapse is "tidal capture",

which also suffers from similar problems. For example, HST observations of the core of 47 Tuc have revealed a surprisingly low number of erupting dwarf novae, in clear conflict with the predictions of simple tidal capture models (Shara et al. 1996). This conflict is made particularly striking given the large numbers of white dwarfs that have now been detected in several clusters (e.g., Richer et al. 1997). These deficiencies notwithstanding, it has been demonstrated that the energy generated from even a few binary interactions is sufficient to cause the core to rebound from a deep core collapse. However, it is also possible that close interactions involving hard binaries could instead lead to an increased collision rate in the core, and possibly the build up (and eventual collapse) of a massive object in the core.

Although observational evidence for primordial binaries in clusters now clearly marks the need for including the influence of binaries in the pre-collapse evolution of clusters, detailed studies of cluster evolution with primordial binaries are still lacking, for several reasons. First, the inclusion of even a modest fraction of primordial binaries adds a very significant computational overhead in simulations. This is not only due to the extra computation required for binary interactions, but also because the lifetime of the cluster (i.e., the core-collapse time) can be significantly extended (by up to an order of magnitude) due to binary heating of the core. In addition, in N-body simulations, the extremely large ratio of the dynamical time to the orbital period of binaries introduces many inefficiencies in the calculations, resulting in much higher computational overhead. This makes N-body simulations with primordial binaries prohibitively expensive for $N \gtrsim 10^3$ stars. Orbit-averaged calculations like direct Fokker-Planck integrations, and Monte-Carlo methods get around this problem by treating binaries just like single stars, except during brief periods of strong interactions. Unfortunately, this requires the cross sections for strong interactions involving binaries to be known accurately, for a wide range of binary parameters (masses, semi-major axes, and eccentricities). These cross sections are difficult to determine in general, and reliable semi-analytic fits to numerical scattering experiments are only available for simple configurations such as those involving equal-mass stars. For these reasons, numerical studies involving primordial binaries have been

limited either to clusters with equal-mass stars (Gao et al. 1991; Spitzer & Mathieu 1980), or to clusters with very low $N \lesssim 10^3$ stars (McMillan et al. 1990). The results of Gao et al. (1991) were the first to clearly illustrate the dominant effect of even a small fraction of primordial binaries on the evolution of a cluster. Partly in order to allow better comparison of our results with theirs, we use similar initial conditions, and cross sections for binary-binary and binary-single interactions, even though our method for implementing these cross sections in the Monte-Carlo scheme is completely different.

An exact and complete comparison between our results is not possible due to the completely different algorithms used to compute interactions in the two methods. In addition, the results of Gao et al. (1991) were obtained using a 1-D Fokker-Planck method. True 2-D Fokker-Planck calculations with primordial binaries are still not possible. Even for the 1-D Fokker-Planck calculations based on energy alone, with only a single parameter representing the internal structure of binaries (namely, their binding energy, ignoring the eccentricity, semimajor axis and individual masses), inclusion of binary-binary interactions significantly increased the overall computation time. Since the Fokker-Planck method uses distribution functions to represent the system, every new parameter adds a new dimension to the phase space, making the Fokker-Planck equation more difficult to solve. In addition, the basic Fokker-Planck method used by Gao et al. (1991) was also 1-D (Cohn 1979, 1980). It has recently been shown that the 1-D treatment is inadequate in dealing with many aspects of the evolution, such as the escape rate from tidally truncated clusters (Takahashi & Portegies Zwart 1998, 1999). A generalization of the basic Fokker-Planck method with primordial binaries to 2-D has not yet been possible. Another deficiency of the Fokker-Planck method is due to its representation of the system as a smooth distribution function. Neglecting the discrete nature of the system makes it impossible to follow the details of individual interactions, such as exchange of one component of a binary with a field star, collisions of stars during resonant interactions, mergers, etc. The implicit assumption that $N \to \infty$ in the Fokker-Planck calculations also makes it difficult to scale their results to finite systems (see, e.g., chap. 4).

Our Monte-Carlo method provides an intermediate approach, which combines many of the benefits of N-body simulations with the speed of an orbit-averaged calculation. The method is also 2-D by construction, and hence properly accounts for the velocity anisotropy in the system. Another benefit of the method is that it allows a wide range of binary parameters to be used without having to modify the underlying orbit-averaged calculation of the 2-body relaxation process. It can also allow individual interactions to be studied in detail, including collisions and exchange interactions, by computing strong interactions exactly using a 3-body integrator.

6.2 Binary Interaction Cross Sections

We use the basic Monte-Carlo method described in chapter 2 to compute the evolution of single stars, as well as binaries, due to two-body relaxation. We now describe the modifications required to take into account binary-binary and binary-single interactions in the Monte-Carlo framework. Cross sections for binary-binary and binary-single interactions are difficult to compute in general, due to the large parameter space for the properties of the interacting binaries, and also because the interactions are often resonant, leading to a variety of final outcomes such as disruption, exchange of one component of a binary with an interacting star, formation of a triple system, and collisions among the interacting stars.

6.2.1 Binary-Binary Interactions

For binary-binary interactions, we use the results of Mikkola (1983 a,b; 1984 a,b) for equal-mass stars. In the case where one binary has a much higher binding energy than the other ($\epsilon_1 >> \epsilon_2$), Mikkola (1984a) provides a semi-analytic fit to his numerical results, giving a collision cross section,

$$\sigma \approx 16.6[\ln(\frac{29|\epsilon_2|}{mw^2 + 0.04|\epsilon_2|})]^{2/3}\frac{Gma_2}{w^2}, \tag{6.1}$$

where w is the relative velocity of the two binaries at infinity, m is the mass of each star in the binary, and a_2 is the semi-major axis of the softer binary. A collision between two binaries can result in two possible types of outcomes- a binary and two single stars, or a hierarchical triple and a single star. In the latter case, since such hierarchical triples are usually short-lived in a dense cluster environment, we assume for simplicity that all hierarchical triples are eventually be destroyed. Thus we assume that in each binary-binary interaction, the softer of the two binaries is destroyed, producing two single stars and a binary. Mikkola also finds that, on average, approximately one-half of the combined binding energy $(\epsilon_1 + \epsilon_2)$ of the two binaries is released in the interaction in the form of translational energy ΔE_t. The semi-analytic fit given by Mikkola (1984a) for the distribution of translational energies produced is rather complicated. Instead, we use a simplified version of the distribution,

$$G(y) = \frac{49}{4} y (1 + \frac{7}{2} y^2)^{-11/4}. \tag{6.2}$$

This simplified version of the distribution function is also used by Gao et al. (1991). The mean value of this distribution $< y > \simeq 0.47$ is in good agreement with Mikkola's results for collisions which result in a binary and two single stars.

We also use a simplified overall binary-binary collision cross section (eq. [6.1]). Replacing the expression in square brackets by its value at $\epsilon_2 = \frac{1}{2} m w^2$, we get a cross section for binary-binary collisions,

$$\sigma_{bb} = 31.8 \frac{G m a_2}{w^2}. \tag{6.3}$$

The energy required to disrupt the softer binary, as well as the total translational energy released in the collision ΔE_t, are both generated at the expense of the energy of the surviving binary. This means that the binding energy of the surviving binary increases by an amount $\epsilon_2 + y(\epsilon_1 + \epsilon_2)$. According to Mikkola (1983a), for collisions between binaries of equal binding energies producing a binary and two single stars, one-fourth of the translational energy produced is carried away by the binary, and the remaining is distributed randomly among the two single stars. For simplicity, we

assume that this prescription is applicable to collisions between binaries of unequal binding energies as well.

During each timestep Δt, we first compute the probability for each binary to have a collision with another binary,

$$P = \sigma w n \Delta t, \tag{6.4}$$

where w is the relative velocity of the nearest binary, n is the local number density of binaries (computed using a sampling procedure), and $\sigma = \sigma_{bb}$. A binary actually has a collision during that timestep if a randomly selected number between 0 and 1 is less than the computed probability. In that case, the total energy released in the collision is computed using equation (6.2). The direction of the recoil velocity of the binary and the two single stars is selected randomly in the center-of-mass frame. The new velocities of the binary and the single stars is then computed. In each binary-binary collision, an additional single star is produced, which is added to the list of stars in the cluster with its proper energy.

6.2.2 Binary-Single Interactions

In a single timestep, usually only a small fraction of the binaries are involved in binary-binary interactions. For the rest of the binaries, a second probability is computed for an interaction with a single star, using equation (6.4), with $\sigma = \sigma_{bs}$, the cross section for binary-single interactions, and n being the local number density of single stars. As before, we take w to be the relative velocity of the nearest star to the binary. The total cross section for binary-single interactions is computed as $\sigma_{bs} = \pi b_{max}^2$, where b_{max} is the largest impact parameter which gives a distance of closest approach between the binary and the single star of $r_{min} = 3.5a$, with a being the binary semi-major axis. For a binary of mass m_b and single star of mass m, $b_{max}^2 = r_{min}^2(1+2G(m+m_b)/(w^2 r_{min}))$

The binary-single interaction is computed only if a randomly selected number is less than the computed probability. The outcome of the binary-single interaction can in principle be computed exactly using a 3-body integrator. Computing binary interactions by direct integration has many benefits, especially in providing an accu-

rate way of distinguishing between the various possible outcomes. However, it also requires significantly more computational resources. As a first step, we again use a semi-analytic fit to numerical results provided by Heggie & Hut (1991) to compute the translational energy released in a binary-single interaction. Let $y = \Delta\epsilon/\epsilon$ be the fraction of the binding energy of the binary that is released as translational energy. Then the differential cross section for the interaction is given by (Heggie & Hut 1991),

$$\frac{d\sigma_{bs}}{dy} = 12.48\pi a^2 (\frac{w}{v_{cr}})^{-2}(1+y)^{-4}y^{-0.5}, \tag{6.5}$$

where $v_{cr}^2 = 3Gm/2a$.

If a binary is not involved in a strong interaction with another binary or a single star, it is then treated as a single star in the 2-body relaxation step (see chapter 2), during which its internal structure is left unchanged.

6.3 Initial Conditions

We use a single component Plummer model, with a small fraction of binaries (10-20%) as our initial cluster model. The binaries are distributed in the cluster according to the Plummer density profile. Hence no initial mass segregation is assumed for the binaries. The distribution of the internal binding energy of the binaries is uniform in $\ln\epsilon$, with the minimum binding energy $\epsilon_{min} = mv_c(0)^2$, where $v_c(0)$ is the initial central 3-D velocity dispersion, and the maximum binding energy $\epsilon_{max} = 133\epsilon_{min}$, which is roughly the binding energy of a contact binary if $v_c(0) = 11\,\mathrm{km\,s^{-1}}$.

6.4 Results

We are able to perform, for the first time, simulations with primordial binaries including binary-single and binary-binary interactions, with a realistic number of stars $N \gtrsim 10^5$.

We first consider the evolution of our "standard model", which begins with a Plummer model, with 10% primordial binaries by number. We first show the main

impact of introducing binaries into the simulation, by focusing on the pre-collapse evolution of the cluster. In Figure 6-1, we show a comparison of a our standard model for an assumed value of $N = 3 \times 10^5$, with the same model without binary interactions, i.e., although the binaries are included in the model as a heavy component, no binary interactions are calculated to provide energy generation. We see that without binary interactions, the cluster undergoes core collapse within just $7\,t_{\rm rh}$, which is a fraction of the core-collapse time for an isolated single component Plummer model (see Chapter 3). However, with the support of binaries, the core is supported against collapse for up to $\approx 60\,t_{\rm rh}$.

In figure 6-2, we show the evolution of the core radius, the half-mass radius of the binaries, and the half-mass radius of the single stars, along with the fraction of the initial number of binaries surviving in the cluster, for the entire duration of the simulation, going well past the initial core collapse. Since in each binary-binary interaction one binary is disrupted, the total number of binaries in the cluster continuously decreases. In addition, some binaries can be kicked out of the cluster due to the recoil energy in a strong encounter. We see that the core radius initially decreases due to mass segregation. This "collapse" phase is followed by a period during which the core is supported against collapse by binary-binary and binary-single interactions for some time. This period is often known as the "Quasi-steady Post-collapse" (or QPC) phase. We find that with $N = 10^5$, this phase does not last very long, and extends the core-collapse time only till $\approx 20\,t_{\rm rh}$. This is significantly shorter than the time reported by Gao et al. (1991) of $\approx 50\,t_{\rm rh}$. However, this difference is mainly caused due to the difference in the number of stars N used. Gao et al. (1991) assume $N = 3 \times 10^5$ in their simulations. The increased value of N has a very significant effect on the core-collapse time, since it directly affects the ratio of the dynamical time to the relaxation time, which in turn affects the rate of binary interactions. We show our results with an assumed value of $N = 3 \times 10^5$ below (Fig. 6-4), where we find a much longer QPC phase, similar to that found by Gao et al. (1991). Note that although the QPC phase is short, it still extends the core-collapse time of the cluster significantly compared to an equivalent cluster without binaries, which collapses

at only $\approx 7\,t_{\rm rh}$ (Fig. 6-1). At the end of the QPC phase, the cluster finally undergoes core collapse, and the core rebounds as the rate of strong interactions increases in response to the core collapse. This launches the cluster into the "Gravothermal Oscillations" (or GTO) phase, during which the cluster maintains a larger core for long periods of time, punctuated by short periods of core collapse. During the QPC phase, the half-mass radius of binaries remains roughly constant, or increases slowly. However, the half-mass radius of the single stars constantly increases.

In figure 6-3, we show the evolution of the total binding energy of the binaries and the total translational energy generated in binary-single and binary-binary interactions for the same model as in figure 6-1. As binaries harden through binary-single and binary-binary interactions, the total binding energy increases. We see that the energy generated in binary-single interactions is smaller than that generated in binary-binary interactions by almost a factor of four. The small increases in the energy during the brief periods in which the core rebounds after collapsing (mainly due to binary-binary interactions) is also clearly visible.

In each timestep, in order to compute a probability for a binary-binary or binary-single interaction, the timestep Δt must be converted from relaxation-time units (see chapter 2) to dynamical-time units. In doing so, we must multiply the timestep by a factor $\simeq N/\ln \gamma N$ (with $\gamma \simeq 0.1$; see Chapter 2). The probability of a strong interaction is proportional to $n\sigma v\Delta t$, where n is the local number density, v is the local velocity dispersion, and σ is the binary interaction cross section. Hence, in the case of low-N clusters, since the evolution timestep is always proportional to the relaxation time, the value of Δt in dynamical-time units is smaller, which causes the interaction probability to be lower. Hence the interaction rate of binaries is smaller in low-N simulations, making it more difficult to support the core against collapse. This is the only place where the dynamical time appears explicitly in our code. The factor $N/\ln \gamma N$ only represents the ratio of the relaxation time to the dynamical time for the cluster, and hence can be set independently without affecting the evolution of the cluster due to two-body relaxation. The main effect of increasing the ratio of the relaxation time to the dynamical time is to increase the rate of binary interactions in

the core, thereby providing more energy to support the core against collapse.

In Figures 6-4 and 6-5, we show the evolution of the Plummer model, with the ratio of the relaxation time to the dynamical time set assuming that the cluster contains $N = 2 \times 10^5$, and $N = 3 \times 10^5$ stars, respectively (although the actual simulation is still performed with 10^5 stars). We can see that, even with the same fraction of primordial binaries (10%), the core is supported at a larger core radius, and for a much longer time compared to our standard model in figure 6-2. However, we also see that the increased binary interaction rate results in fewer gravothermal oscillations after the first collapse, which are replaced instead by another longer phase in which the core is supported against collapse by binary interactions.

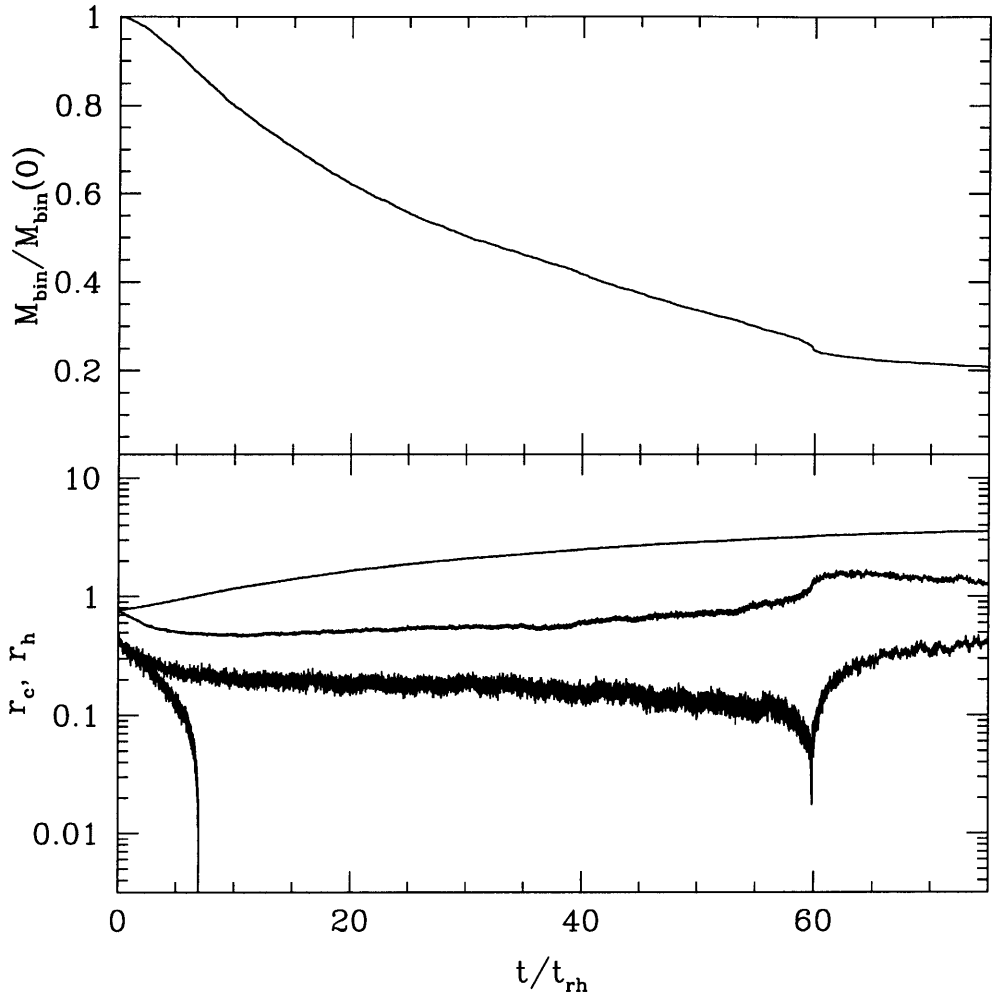

Figure 6-1: Evolution of the Plummer model, with $N = 3 \times 10^5$ stars, with 10% primordial binaries. The lowest curve is the core radius, followed by the half-mass radius of the binaries, and the half-mass radius of the single stars. Also shown is the total number of surviving binaries, as a fraction of the total initial number of binaries. Also shown, is the core radius for an equivalent Plummer model *without* binaries, which undergoes core collapse at only $\approx 7\, t_{\rm rh}$. Thus, the presence of binaries in a cluster, even at the 10% level, can extend the core-collapse time for the cluster by more than an order of magnitude.

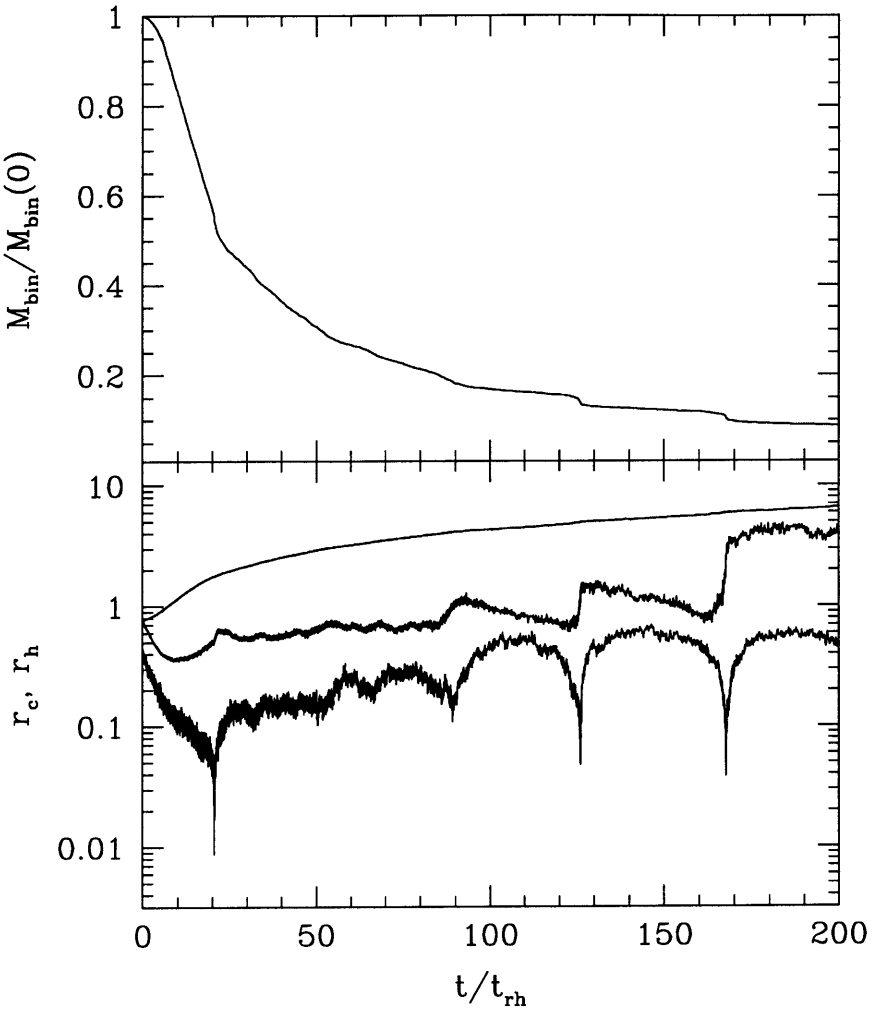

Figure 6-2: Evolution of the Plummer model, with $N = 10^5$ stars, with 10% primordial binaries. The lowest curve is the core radius, followed by the half-mass radius of the binaries, and the half-mass radius of the single stars. Also shown is the total number of surviving binaries, as a fraction of the total initial number of binaries. Note the sharp (but small) drops in the number of binaries during periods of core bounce, when binaries are destroyed at an accelerated rate in binary-binary interactions.

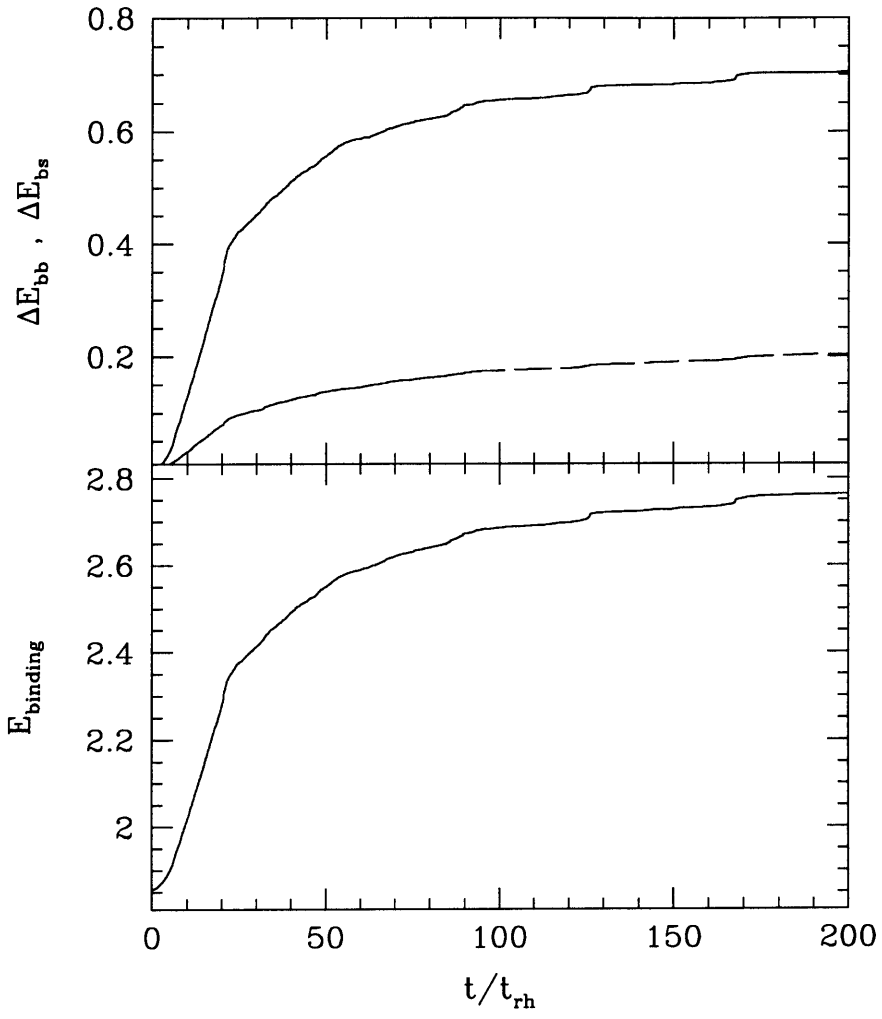

Figure 6-3: Evolution of the Plummer model, with $N = 10^5$ stars, with 10% primordial binaries. The lower panel shows the evolution of the total binding energy of the binaries. As binaries harden through binary-single and binary-binary interactions, the total binding energy increases. Also shown (top panel) is the total translational energy generated through binary-binary interactions (upper line) and binary-single interactions (lower line). We see that the energy generated in binary-single interactions is smaller than that generated in binary-binary interactions by almost a factor of four. The small jumps in the energy during the brief periods in which the core rebounds after collapsing (mainly due to binary-binary interactions) is clearly visible.

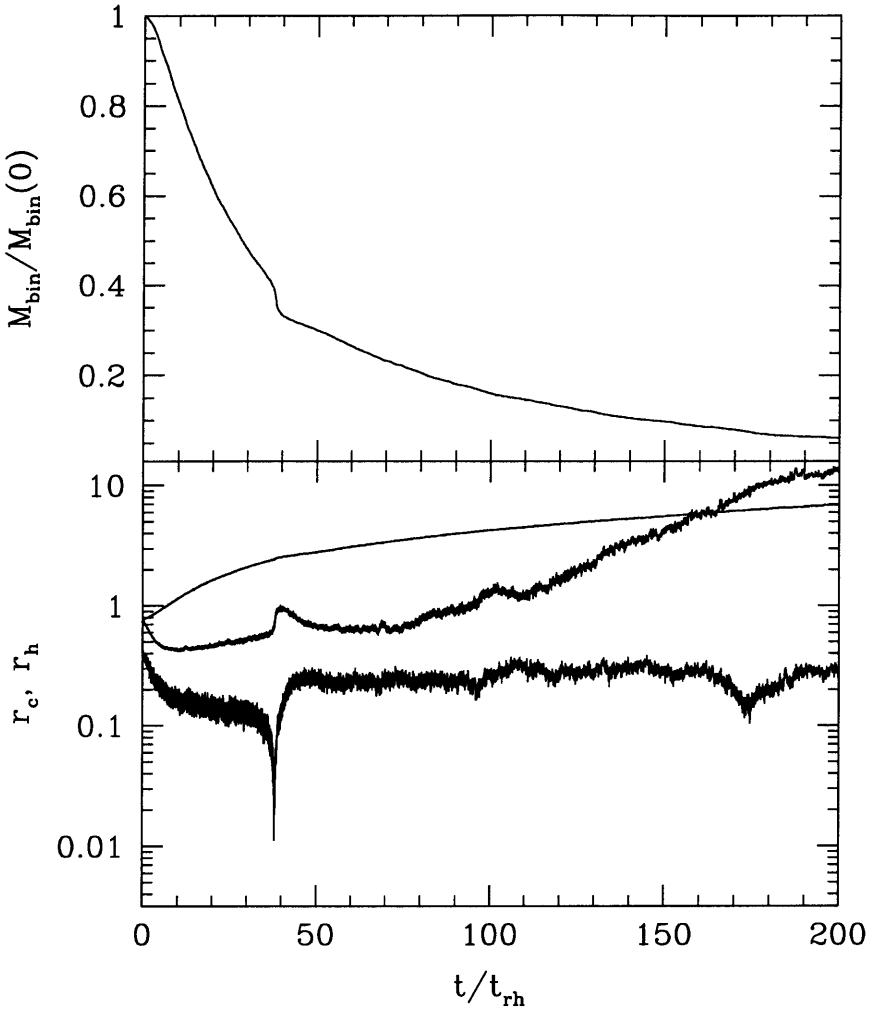

Figure 6-4: Same as Fig. 6-1, but with the ratio of the relaxation time to the dynamical time $N/\ln\gamma N$ computed using $N = 2 \times 10^5$. This ratio is only used to convert the timestep from relaxation time units to dynamical time units, in order to compute the probability for a binary-binary or binary-single interaction. This effectively raises the rate of interactions in the core, simulating the effect of binaries in a larger cluster with $N = 2 \times 10^5$ stars, even though our simulation only contains 10^5 stars.

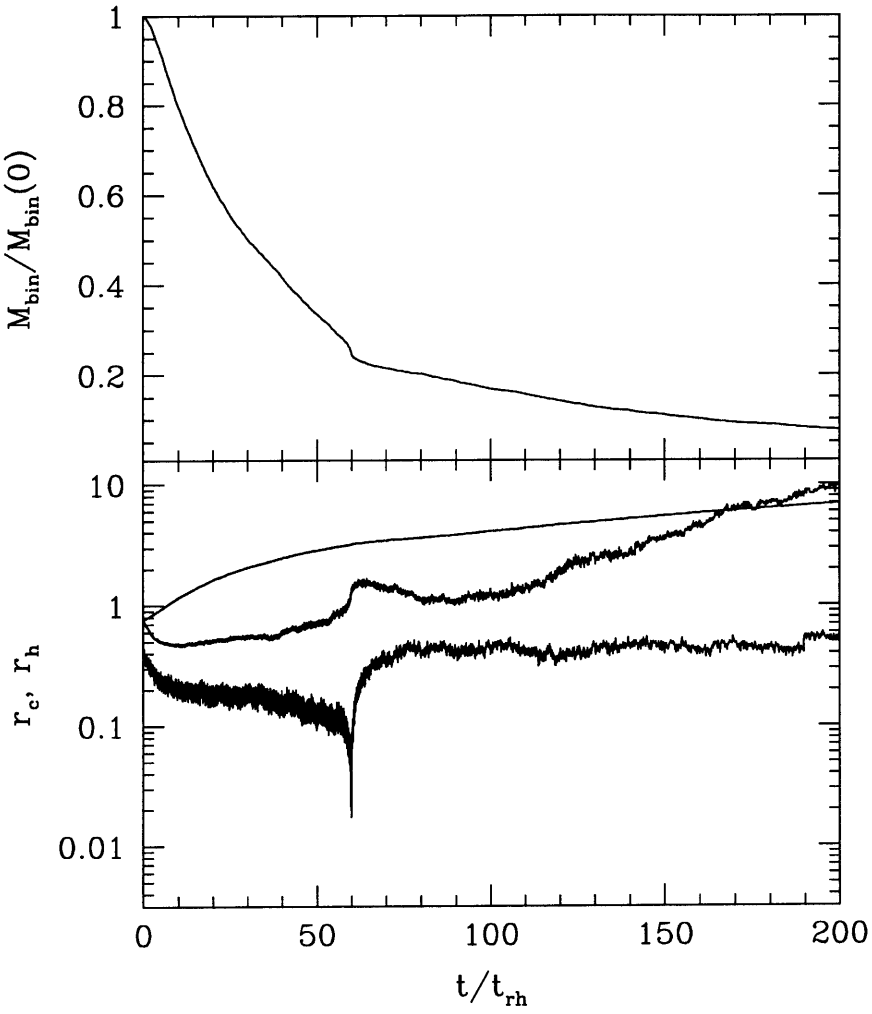

Figure 6-5: Same as Fig. 6-3, but with the ratio of the relaxation time to the dynamical time $N/\ln \gamma N$ computed using $N = 3 \times 10^5$.

There are several differences between our results and those of Gao et al. (1991). Although the qualitative behavior of our models is very similar to theirs, we find that the rate of binary-binary interactions in our calculations is slightly lower than theirs, which causes our standard model to undergo the first core collapse earlier at $\sim 20\,t_{rh}$, compared to the longer time of $\sim 50\,t_{rh}$ found by Gao et al. (1991). This difference is in large part due to the higher value of $N = 3 \times 10^5$ assumed in their calculations, which gives a larger ratio of the relaxation time to the dynamical time in the core, thereby effectively increasing the rate of binary-binary interactions in the core. As noted above, and shown in Figures 3 and 4, assuming a larger value of N in our calculations also gives a similar longer QPC phase, with the first core collapse occurring at $\sim 60\,t_{rh}$ for $N = 3 \times 10^5$. Note that in Fokker-Planck calculations the assumed value of N is also completely arbitrary, since the method uses a smooth distribution function, which gives the evolution of the system in the $N \to \infty$ limit. Hence we consider the agreement between our results for the time to first collapse (for an equivalent number of stars, with 10% binaries) to be good.

A more significant difference between our results is in the post-collapse evolution, where Gao et al. (1991) find gravothermal oscillations of the core beginning immediately after the first core collapse, where as in our models, pronounced gravothermal oscillations begin later in the post-collapse phase, when the number of binaries has dropped further. This is mainly due to the difference in the way the rate of binary-binary interactions is computed in their Fokker-Planck models. In converting time units from the relaxation time to the dynamical time, Gao et al. (1991) replace the quantity $\ln \gamma N$ with $\ln \gamma N_c$, with $\gamma = 0.4$, and N_c being the number of stars in the *core*. Since N_c is much smaller than N, and also varies significantly during core collapse and rebound, it serves as an additional factor which affects the binary-binary collision probability. In particular, when the core collapses, N_c gets smaller, thereby boosting the binary-binary interaction rate, while as the core rebounds and grows in size, N_c increases, causing the binary interaction rate to drop, and allowing the core to go the next core collapse. In our scheme, the quantity $\ln \gamma N$ remains roughly constant through the simulation. The only factor affecting the rate of binary inter-

actions in the core is the number density in the core, and the core relaxation time. Hence we find that after the core rebounds, the interaction rate does not diminish as quickly, and the core is again supported against collapse for a longer time. This also causes the disruption rate of binaries in the post-collapse phase to be higher in our simulations. Gravothermal oscillations eventually begin when the number of binaries drops below the level needed to support the core. Since the timestep in our method is already proportional to the core relaxation time, we only need to scale its value from the relaxation time (which is our unit for the overall evolution time), to the dynamical time. We prefer to hold the time units fixed in our calculations, and hence only use a constant factor $N/\ln \gamma N$ to convert time units. The smaller value of N_c used by Gao et al. (1991) only causes the overall interaction cross section to be slightly larger, thereby supporting the core at a larger radius than would otherwise be the case. Since the core radius does not change very much during the QPC phase, the binary interaction rate remains relatively constant. Hence, in spite of using slightly different scaling factors for the dynamical time, our core-collapse times agree well with those of Gao et al. (1991), for equivalent systems. The difference becomes pronounced during, and after core collapse, as the value of N_c varies significantly during this phase.

6.5 Summary

We have performed, for the first time, discrete simulations of globular clusters with a realistic number of stars with up to 10% primordial binaries. We find that the energy generated through binary-binary and binary-single interactions can support the core against collapse for many tens of relaxation times. However, in every case, the cluster eventually undergoes core collapse, which is followed by a phase of gravothermal oscillations. Our results up to the first core collapse are in good agreement with those of Gao et al. (1991). However, we find that in our models the gravothermal oscillations begin much later in the evolution compared to equivalent Fokker-Planck models. This could be in part due to the time-dependent scaling of the relaxation time to the

dynamical time used in the Fokker-Planck models. We have also shown that the effect of binaries on the evolution of a cluster is very sensitive to the total number of stars N in the cluster. This implies that it is not possible to directly compare results from smaller N-body simulations with those from large N simulations. Our code immediately provides the framework for more realistic simulations of globular cluster evolution, using more accurate cross sections for binary-binary and binary-single interactions, and also allows for arbitrary masses, and other binary parameters (assuming the interaction cross sections are known). Alternatively, binary-binary and binary-single interactions can be computed by exact numerical integrations, which will provide new insights into interactions that result in the exchange of stars in a binary, disruption of soft binaries, and collisions of stars during resonant interactions.

Bibliography

[1] Aarseth, S. 1998, in Impact of Modern Dynamics in Astronomy, IAU Colloq. 172, 1

[2] Anderson, S. B. 1992, PhD thesis, California Institute of Technology

[3] Bailyn, C. D. 1995, ARAA, 33, 133

[4] Binney, J., & Tremaine, S. 1987, Galactic Dynamics (Princeton, PUP)

[5] Breeden, J. L., Cohn, H. N., & Hut, P. 1994, ApJ, 421, 195

[6] Burgarella, D., Paresce, F., Meylan, G., King, I. R., Greenfield, P., Baxter, D., Jedrzejewski, R., Nota, A., Albrecht, R., Barbieri, C., Blades, J. C., Boksenberg, A., Crane, P., Deharveng, J. M., Disney, M. J., Jakobsen, P., Kamperman, T. M., Macchetto, F., Mackay, C. D., & Weigelt, G. 1994, A&A, 287, 769

[7] Burgarella, D., Paresce, F., & Quilichini, V. 1995, A&A, 301, 675

[8] Camilo, F., Lorimer, D. R., Freire, P., Lyne, A. G., & Manchester, R. N. 2000, ApJ, in press, [astro-ph/9911234]

[9] Chang, J. S., & Cooper, G. 1970, J. Comput. Phys., 6, 1

[10] Chernoff, D. F., Kochanek, C. S., & Shapiro, S. L. 1986, ApJ, 309, 183

[11] Chernoff, D. F. 1996, in Dynamical Evolution of Star Clusters, IAU Symp. 174, eds. P. Hut & J. Makino, 239

[12] Chernoff, D. F. & Weinberg, M. D. 1990, ApJ, 351, 121

[13] Cohn, H. 1979, ApJ, 234, 1036

[14] Cohn, H. 1980, ApJ, 242, 765

[15] Cool, A. M., Grindlay, J. E., Cohn, H. N., Lugger, P. M., & Slavin, S. D. 1995, ApJ, 439, 695

[16] Danner, R., Kulkarni, S. R., & Thorsett, S. E. 1994, ApJ, 436, L153

[17] Davies, M. B., & Hansen, B. M. S. 1998, MNRAS 301, 15

[18] De Marchi, G., & Paresce, F. 1994, ApJ, 422, 597

[19] De Marchi, G., Paresce, F., Stratta, M. G., Gilliland, R. L., & Bohlin, R. C. 1996, ApJ, L51

[20] Di Stefano, R., & Rappaport, S. 1994, ApJ, 423, 274

[21] Drukier, G.A., Cohn, H. N., Lugger, P. M., & Yong, H. 1999, ApJ, 518, 233

[22] Duncan, M. J., & Shapiro, S. L. 1982, ApJ, 253, 921

[23] Edmonds, P.D., Bailyn, C. D., Cohn, H. N., Cool, A. M., Gilliland, R. L., Grindlay, J. E., Livio, M., Lugger, P. M., Meylan, G., Petro, L. D. 1997, AAS, 191, #44.15

[24] Ferraro, F. R., Carretta, E., Bragaglia, A., Renzini, A., Ortolani, S. 1997a, MNRAS, 286, 1012

[25] Ferraro, F. R., Paltrinieri, B., Fusi Pecci, F., Rood, R. T., Dorman, B. 1997b, MNRAS, 292, L45

[26] Gao, B., Goodman, J., Cohn, H., & Murphy, B. 1991, ApJ, 370, 567

[27] Geffert, M., Auriere, M., Koch-Miramond, L. 1997, A&A, 327, 137

[28] Giersz, M. 1998, MNRAS, 298, 1239

[29] Giersz, M., & Heggie, D. C. 1994, MNRAS, 268, 257

[30] Gilliland, R. L., Edmonds, P. D., Petro, L., Saha, A., Shara, M. M. 1995, ApJ, 447, 191

[31] Gnedin, O. Y., Lee, H. M., & Ostriker, J. P. 1999, ApJ, 522, 935

[32] Goodman, J., Heggie, D. C., & Hut, P. 1993, ApJ, 415, 715

[33] Guhathakurta, P., Yanny, B., Schneider, D. P., & Bahcall, J. N. 1996, AJ, 111, 267

[34] Guhathakurta, P., Webster, Z. T., Yanny, B., Schneider, D. P., & Bahcall, J. N. 1998, AJ, 116, 1757

[35] Heggie, D. C., Giersz, M., Spurzem, R., & Takahashi, K. 1999, in Highlights of Astronomy, vol. 11, ed. J. Andersen, 591

[36] Heggie, D. C., & Hut, P. 1993, ApJS, 85, 347

[37] Heggie, D. C., Hut, P., McMillan, S. L. W. 1996, ApJ, 467, 359

[38] Heggie, D. C., & Mathieu 1986, in The Use of Supercomputers in Stellar Dynamics, (Berlin: Springer) eds. Hut, P. & McMillan, S. L. W., 233

[39] Heggie, D. C., & Stevenson, D. 1988, MNRAS, 230, 223

[40] Hénon, M. 1971a, Ap. Space Sci., 13, 284

[41] Hénon, M. 1971b, Ap. Space Sci., 14, 151

[42] Hernquist, L., Hut, P., & Makino, J. 1993, ApJ, 402, L85

[43] Hertz, P., & Grindlay, J. E. 1983, ApJ, 267, L83

[44] Hut, P., & Makino, J. 1999, Science, 283, 501

[45] Hut, P., Makino, J., & McMillan, S. 1995, ApJ, 443, L93

[46] Hut, P., McMillan, S., & Romani, R. W. 1992, ApJ, 389, 527

[47] Hut, P., McMillan, S., Goodman, J., Mateo, M., Phinney, E. S., Pryor, C., Richer, H. B., Verbunt, F., & Weinberg, M. 1992, PASP, 104, 981

[48] Inagaki, S., & Wiyanto, P. 1984, PASJ, 36, 391

[49] Jahn, K., Kałużny, J., Ruciński, S. M. 1995, A&A, 295, 101

[50] Joshi, K. J., Rasio, F. A., & Portegies Zwart, S. 2000, ApJ submitted, [astro-ph/9909115]

[51] Joshi, K. J., Nave, C., & Rasio, F. A. 2000, ApJ submitted, [astro-ph/9912155]

[52] Kałużny, J., & Ruciński, S. M. 1993, in Blue Stragglers, ed. R. E. Saffer (ASP Conf. Ser. Vol. 53), 164

[53] Katz, J., & Taff, L. G. 1983, ApJ, 264, 476

[54] Kim, S. S., Lee, H. M., & Goodman, J. 1998, ApJ, 495, 786

[55] King, I. R. 1966, AJ, 71, 64

[56] Kochanek, C. S. 1992, ApJ, 385, 604

[57] Kondrat'ev, B. P., & Ozernoy, L. M. 1982, ApJS, 84, 431

[58] Kumar, P., & Goodman, J. 1996, ApJ, 466, 946

[59] Lewin, W. H. G., Van Paradijs, J., Taam, R. E. 1993, Sp. Sci. Rev., 62, 223

[60] Lightman, A. P., & Shapiro, S. L. 1977, ApJ, 211, 244

[61] Lightman, A. P., & Fall, S. M. 1978, ApJ, 221, 567

[62] Livio, M. 1993, in ASP Conf. Ser., 53, Blue Stragglers, ed. R.A. Saffer (San Francisco: ASP), 3

[63] Lynden-Bell, D., & Eggleton, P. P. 1980, MNRAS, 191, 483L

[64] Makino, J. 1996, ApJ, 471, 796

[65] Makino, J., Taiji, M., Ebisuzaki, T., & Sugimoto, D. 1997, ApJ, 480, 432

[66] Marchant, A. B., & Shapiro, S. L. 1980, ApJ, 239, 685

[67] Marconi, G., Buonanno, R., Carretta, E., Ferraro, F. R., Montegriffo, P., Fusi Pecci, F., De Marchi, G., Paresce, F., Laget, M. 1998, MNRAS, 293, 479

[68] Mateo, M., Harris, H. C., Nemec, J., & Olszewski, E. W. 1990, AJ, 100, 469

[69] McMillan S. L. W., Hut P., & Makino, J. 1990, ApJ, 362, 522

[70] McMillan S. L. W., Hut P., & Makino, J. 1991, ApJ, 372, 111

[71] McMillan S. L. W., & Hut P. 1994, ApJ, 427, 793

[72] Merritt, D. 1981, AJ, 86, 318

[73] Miller, G. E., & Scalo, J. M. 1979, ApJ, 41, 513

[74] Milone, A. A. E., & Latham, D. W. 1994, AJ, 108, 1828

[75] Murphy, B. & Cohn, H. 1988, MNRAS, 232, 835

[76] Phinney, E. S. 1992, Phil. Trans. R. Soc. Lond., A, 341, 39

[77] Piotto, G., Cool, A. M., & King, I. R. 1997, AJ, 113, 1345

[78] Piotto, G., Zocalli, M., King, I. R., Djorgovski, S. G., Sosin, C., Dorman, B., Rich, R. M., & Meylan, G. 1999, AJ, 117, 264

[79] Portegies Zwart, S. 1995, PhD thesis, Univ. of Utrecht

[80] Portegies Zwart, S., Hut, P., McMillan, S.L.W., & Verbunt, F. 1997, A&A, 328, 143

[81] Portegies Zwart, S., Hut, P., Makino, J., & McMillan, S.L.W. 1998, A&A, 337, 363

[82] Portegies Zwart, S., Makino, J., McMillan, S.L.W., & Hut, P. 1999, A&A, 348, 117

[83] Press, W. H., Teukolsky, S. A., Vetterling, W. T., & Flannery, B. P. 1992, Numerical Recipes in C: The Art of Scientific Computing (2nd ed. New York: Cambridge University Press)

[84] Quinlan, G.D. 1996, New Astronomy vol. 1, no. 3, 255

[85] Rasio, F. A. 2000, to appear in Pulsar Astronomy – 2000 and Beyond, eds. M. Kramer, N. Wex, & R. Wielebinski (ASP Conf. Series), [astro-ph/9911133]

[86] Rich, R. M., Sosin, C., Djorgovski, S. G., Piotto, G., King, I. R., Renzini, A., Phinney, E. S., Dorman, B., Liebert, J., & Meylan, G. 1997, ApJ, 484, L25

[87] Richer, H.B., Fahlman, G. G., Ibata, R. A., Pryor, C., Bell, R. A., Bolte, M., Bond, H. E., Harris, W. E., Hesser, J. E., Holland, S., Ivanans, N., MandusheV, G., Stetson, P. B., Wood, M. A. 1997, ApJ, 484, 741

[88] Robinson, C., Lyne, A. G., Manchester, R. N., Bailes, M., D'Amico, N., & Johnston, S. 1995, MNRAS, 274, 547

[89] Rubenstein, E. P., & Bailyn, C. D. 1996, AJ, 111, 260

[90] Rubenstein, E. P., & Bailyn, C. D. 1997, ApJ, 474, 701

[91] Shara, M. M., Drissen, L., Bergeron, L. E., & Paresce, F. 1995, ApJ, 441, 617

[92] Shara, M. M., Bergeron, L. E., Gilliland, R. L., Saha, A., & Petro, L. 1996, ApJ, 471, 804

[93] Sigurdsson, S., & Phinney, E. S. 1995, ApJS, 99, 609

[94] Sosin, C., & King, I. R. 1995, AJ, 109, 639

[95] Sosin, C., & King, I. R. 1997, AJ, 113, 1328

[96] Spitzer, L. 1969, ApJ, 158, L139

[97] Spitzer, L. 1987, Dynamical Evolution of Globular Clusters (Princeton: Princeton University Press)

[98] Spitzer, L. & Hart, M. H. 1971a, ApJ, 164, 399

[99] Spitzer, L. & Hart, M. H. 1971b, ApJ, 166, 483

[100] Spurzem, R. & Giersz, M. 1996, MNRAS, 283, 805

[101] Statler, T. S., Ostriker, J. P., & Cohn, H. 1987, ApJ, 316, 626

[102] Stodólkiewicz, J. S. 1982, Acta Astron., 32, 63

[103] Stodólkiewicz, J. S. 1985, in Dynamics of Star Clusters, IAU Symp. 113, eds J. Goodman & P. Hut (Reidel, Dordrecht), 361

[104] Stodólkiewicz, J. S. 1986, Acta Astron., 36, 19

[105] Sugimoto, D., & Bettwieser, E. 1983, MNRAS, 204, 19P

[106] Takahashi, K. 1995, PASJ, 47, 561

[107] Takahashi, K. 1996, PASJ, 48, 691

[108] Takahashi, K. 1997, PASJ, 49, 547

[109] Takahashi, K., & Portegies Zwart, S. F. 1998, ApJ, 503, L49

[110] Takahashi, K., & Portegies Zwart, S. F. 1999, ApJ, submitted, [astro-ph/9903366]

[111] Verbunt, F., van Paradijs, J., & Elson, R. 1984, MNRAS, 210, 899

[112] Watters, W., Joshi, K. J., & Rasio, F. A. 2000, ApJ submitted, [astro-ph/9912457]

[113] White, N., & Mason, K. 1985, Sp. Sci. Rev., 40, 167

[114] Yan, L., & Mateo, M. 1994, AJ, 108, 1810

[115] Yanny, B., Guhathakurta, P., Schneider, D. P., & Bahcall, J. N. 1994, ApJ, 435, L59

[116] Yoshizawa, M., Inagaki, S., Nishida, M. T., Kato, S., Tanaka, Y., & Watanabe, Y. 1978, PASJ, 30, 279